学位論文

The Behavior of the Deuterated Species after Birth of Protostars

(原始星形成にともなう重水素化合物の振る舞い)

平成 26 年 12 月 博士（理学）申請

東京大学大学院理学系研究科
物理学専攻

柴田 大輝

Abstract

The star formation is the most basic structural formation process, and is actively studied as a critical issue of the astrophysics. The deuterium fractionation is a phenomenon that deuterium atoms are enriched in molecules under a cold condition of molecular clouds. So far, the deuterium fractionation of molecules has been widely used as a useful evolutionary tracer for starless-core phase of star formation. In contrast to extensive studies of deuterium fractionation in starless cores, studies of deuterium fractionation after the onset of star formation are very limited.

To examine the behavior of the deuterated species after the birth of protostar, we conducted observations of deuterated species toward the low-mass protostar, L1551-IRS5, L483, NGC1333-IRAS2A, IRAS16293-2422 and L1251A with the Nobeyama 45 m telescope and the ASTE 10 m telescope. Additionally, we used the archival data of The Submillimeter Array (SMA). As a result, we find that the deuterium fractionation ratios of the ionic species, DCO^+/HCO^+, and those of the neutral species, DNC/HNC, show the different behavior toward L1551-IRS5, L483, NGC1333-IRAS2A and IRAS16293-2422. The DCO^+/HCO^+ ratios decrease toward the protostar position, while the DNC/HNC ratios do not show such a trend. Moreover, the archival data of SMA for IRAS16293-2422 show that the neutral deuterated species are concentrated around the protostar and the ionic deuterated species are widely distributed away from the protostar position. We interpret this difference by the different timescale of destruction processes of deuterated species. Once the protostar is formed and the temperature of the ambient gas rises, the neutral deuterated species do not destructed for a while, whereas the ionic deuterated species are rapidly destructed. Our result seems to show this difference. Above all, it is confirmed that the deuterium fractionation ratio changes systematically after the protostar birth. In addition, the HNC/HCN ratio is shown to behave the deuterium fractionation of the ionic species: it is found to decrease toward the protostellar position of L483.

Contents

Chapter 1

Introduction

1.1 Interstellar molecular cloud and star formation

1.1.1 Interstellar molecular cloud

Interstellar molecular clouds are a representative form of interstellar clouds, where hydrogen mainly exists as hydrogen molecules. Those are places of star formation. Interstellar molecular clouds can be classified by the visual extinction A_V, as diffused clouds, giant molecular clouds, dark clouds, dense cores and Bok globules. Their typical physical conditions are shown in table 1.1. Such interstellar molecular clouds are widely distribute in the galaxy. Figure 1.1 shows distribution of interstellar molecular clouds near the sun (Dame et al. 1987).

Molecular clouds are generally at low temperature, and they do not emit visible light and near-infrared. However, they emit rotational transitions of molecules and dust continuum emission at radio wavelength. For this reason, the radio wave is mainly used to study inter-

molecular clouds	Av [mag]	density [cm^{-3}]	size [pc]	temperature [K]	mass [$M_\odot$]
Diffuse Clouds	1	500	3	50	50
Giant Molecular Clouds	2	100	50	15	10^5
Dark Clouds					
Complexes	5	500	10	10	10^4
Individual	10	10^3	2	10	30
Dense Cores / Bok Globules	10	10^4	0.1	10	10

Table 1.1: Typical physical conditions of molecular clouds.

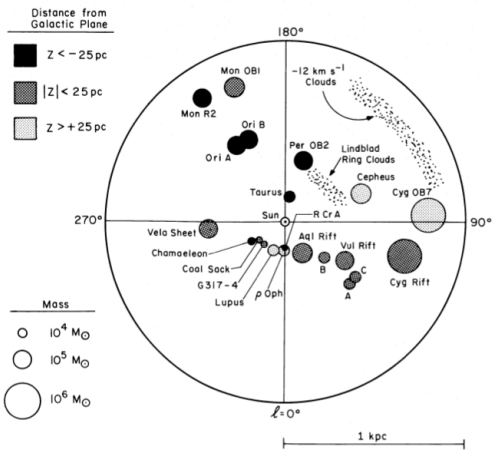

Figure 1.1: The distributions of the molecular clouds located within 1 kpc of the solar system (Dame et al. 1987). The size of the circles showes the size of the molecular clouds and the pattern shows the distance from the galactic plane. (Dame et al., ApJ, 322, 706, 1987, ©AAS. Reproduced with permission.)

stellar molecular clouds. Since discovery of the rotational emission spectrum of CO toward the Orion A molucular cloud in 1970 (Wilson et al. 1970), CO is widely used as a tracer of interstellar molecular clouds. Moreover, various molecules other than CO are also observed in interstellar molecular clouds.

We can study distributions and structures in interstellar molecular clouds by observing molecular spectral lines. Additionally, we can derive their physical conditions as temperature, density and mass. Moreover, we can investigate kinematics through the Dopplar effect.

In interstellar molecular clouds, about 150 species have been observed so far. Historically, studies of interstellar molecules started from observations of visible spectra of CN, CH and CH^+ toward the ζ Ophiuchi in 1940 (Mckellar 1940). However, these molecules are simple diatomic molecules and these discoveries did not draw much attention at that time. After that, microwave technology was developed, and radio spectral lines of the OH radical were first observed in 1963 for the first time. In 1968, the inversion spectrum of NH_3 was detected toward the galactic center (Cheung et al. 1968), and the rotational lines of H_2CO and H_2O were subsequently discovered in 1968 . Furthermore, the CO lines which plays an important role in present-day studies of molecular clouds was discovered in 1970 (Wilson et al. 1970). In molecular clouds, it is known that species which hardly exist in the terrestrial condition exist. Examples are molecular ions like HCO^+ and N_2H^+ and the

unstaturated molecules like HC_7N, HC_9N and $HC_{11}N$. These molecules do not stably exist under the terrestrial conditions because of their high chemical reactivity. However, reactions with other molecules hardly occur in interstellar conditions, because they collide with other molecules about only once in a day. Moreover, these molecules are not photodissociated because ultraviolet radiation is well shielded in molecular clouds.

The most abundant molecule in molecular clouds is H_2. The next most abundant molecules is CO, where the fractional abundance of CO relative to H_2 is 10^{-4}. The other molecules are minor and fractional abundances relative to H_2 are less than 10^{-6}. Characteristic features of interstellar chemistry are existence of the following classes of molecules. The first are ionic species such as H_3^+, HCO^+, OH^+. The existence of such ionic species means that molecular clouds are weakly-ionized prasma. The second are free radicals like OH, CH, C_2H. These free radicals are very reactive, and contribute to various reactions in the interstellar molecular cloud. The third are carbon-chain molecules such as C_3S, HC_7N, CH_3C_6H. The discoverty of these carbon chain molecules are surprising to astronomers.

Interstellar molecules are considered to be produced by chemical reactions driven by the cosmic ray. High energy cosmic rays penetrate molecular clouds and ionizes molecules. Ion-molecule reactions driven by molecular ions produce interstellar molecules. On the other hands, complex molecules such as $HCOOCH_3$ and C_2H_5CN are formed on surface of interstellar dust grains. The molecules formed on dust grains are evaporated from dust grains when protostars are born. Dust grains are heated up, and various molecules are thermally desorbed. In fact, molecules such as CH_3OH are observed in small regions whose temperatures are raised by star formation activities (hot core).

As mentioned above, chemical compositions reflect physical conditions and their past history. From this reason, these interstellar molecules are used as a important tool to study by star formation processes.

1.1.2 Star formation

Interstellar clouds are mostly in pressure equilibrium. However, gravitational contraction occurs in some parts where the density becomes high due to gravitational instability. Evolutionary stages of star formation are classified qualitatively into three phases as follows:

- **Starless core** It was observationally shown by Myers and Benson (Myers et al. 1983; Benson et al. 1989) that dense cores are birthplaces of protostars. Typical dense cores have H_2 density of 10^4 cm^{-3}, a size of 0.1 pc, temperature of 10 K and mass of

$10M_{\odot}$. Dense cores are in isothemal contraction up to the central density of about 10^{11} cm^{-3}. The timescale of the contraction is represented by the following equation (free fall time):

$$t_{\rm ff} = \left(\frac{3\pi}{32G\rho_0}\right)^{1/2}. \tag{1.1}$$

For initial H_2 density of 10^4 cm^{-3}, this timescale is 4×10^5 years. Real duration time of the starless core phase is extended to about 10^6 years because of support by turbulent motions and magnetic field.

- **Protostar** When the density of a starless core becomes as high as 10^{11} cm^{-3}, the radiation cooling becomes inefficient, because dust continuum emission becomes optically thick. For this reason, the temperature of the central region of the core rises. This is called the first stellar core. Moreover, when the central temperature reaches at 2000 K, dissociation of H_2 occurs. Dissociation enegy is so large that gravitational contraction of the central region is accelerated. This phase is called the second stellar core and the protostars are considered to be born at this point. Interstellar matter remains in a flattened envelope, and it still accretes onto protostars. Moreover, the bipolar outflows are developed perpendicular to the envelope.

- **T-Tauri star** After dissipating the surrounding gas by bipolar outflows, the accretion onto protostars stop, and protostars are evolved into the phase called the T-Tauri star. In this phase, stars are still shining by releasing of gravitational energy. The heat emerged in the central part of the star is mainly derivered to the surface by convection and the star contracts quasi-statically (the Hayashi track) (Hayashi et al. 1961). Moreover when the central temperature becomes high, the heat is transfered more effectively by thermal radiation. For this reason, contraction of the central part further proceeds. When the central temperature becomes higher, nuclear fusion reactions occur in the central region At first, nuclear fusion of deuterium starts, and the nuclear fusion of hydrogen occurs in the next phase. Then, stars evolved into main-sequence stars.

Observationally, the above evolutionally stages of the protostars are classified by the infrared excess (the infrared spectral index):

$$\alpha_{\rm IR} \equiv \frac{d\log(\lambda F_\lambda)}{d\log\lambda}. \tag{1.2}$$

Here, λ denotes wavelength, F_λ the flux. Objects of $\alpha_{\rm IR} > 0$ are called Class I, those of $-1.5 < \alpha_{\rm IR} < 0$ are called Class Ⅱ, and those of $\alpha_{\rm IR} < -1.5$ are called Class Ⅲ (Lada et al. 1987).

Moreover, protostars, which are deeply embedded in dense cores and can be observed only by the far infrared wave, were found. These sources are called Class 0. Protostars are considered to evolve in the order of Class 0 → Class I → Class Ⅱ → Class Ⅲ, and finally to main-sequence stars (André et al. 1990).

1.2 The CO depletion

As mentioned above, the carbon monoxide (CO) is the major molecule next to H_2 in molecular clouds ($[CO] \simeq 10^{-4}[H_2]$). CO plays an important role in radiative cooling of molecular clouds, and heavily influences to chemical processes.

On the other hands, there exist dust grains in molecular clouds whose mass is about 1/100 of the gas mass. At low temperature molecules are absorbed onto dust grains by collision with dust grains. This phenomenon is called the depletion. CO is also depleted if the temperature is less than 20 K (CO depletion). An observational evidence of CO depletion is first shown by Caselli et al. (1999).

They observed the starless core L1544 in Taurus with the IRAM 30 m telescope. Toward L1544, they observed the molecules such as $C^{18}O$, $C^{17}O$, DCO^+, $HC^{18}O^+$, $D^{13}CO^+$, $H^{13}CO^+$, HC_3N, N_2D^+ as well as dust emission. Figure 1.2 shows distribution of dust continuum emission, which well traces distribution of the column density because of its low opacity. Toward the peak of the dust continuum emission, the $C^{17}O$ line intensity becomes low in comparison with the surrounding positions. Since the $C^{17}O$ line is optically thin, this result indicates that the abundance of CO is decreased toward the dust continuum peak. This result established that CO is indeed depleted onto dust grains in a dense part of starless core.

The CO molecules depleted on dust grains react with the atomic hydrogen on the grain surface as:

$$\mathrm{H + CO} \longrightarrow \mathrm{HCO} \tag{1.3}$$

$$\mathrm{H + HCO} \longrightarrow \mathrm{H_2CO} \tag{1.4}$$

$$\mathrm{H + H_2CO} \longrightarrow \mathrm{CH_3O} \tag{1.5}$$

$$\mathrm{H + CH_3O} \longrightarrow \mathrm{CH_3OH.} \tag{1.6}$$

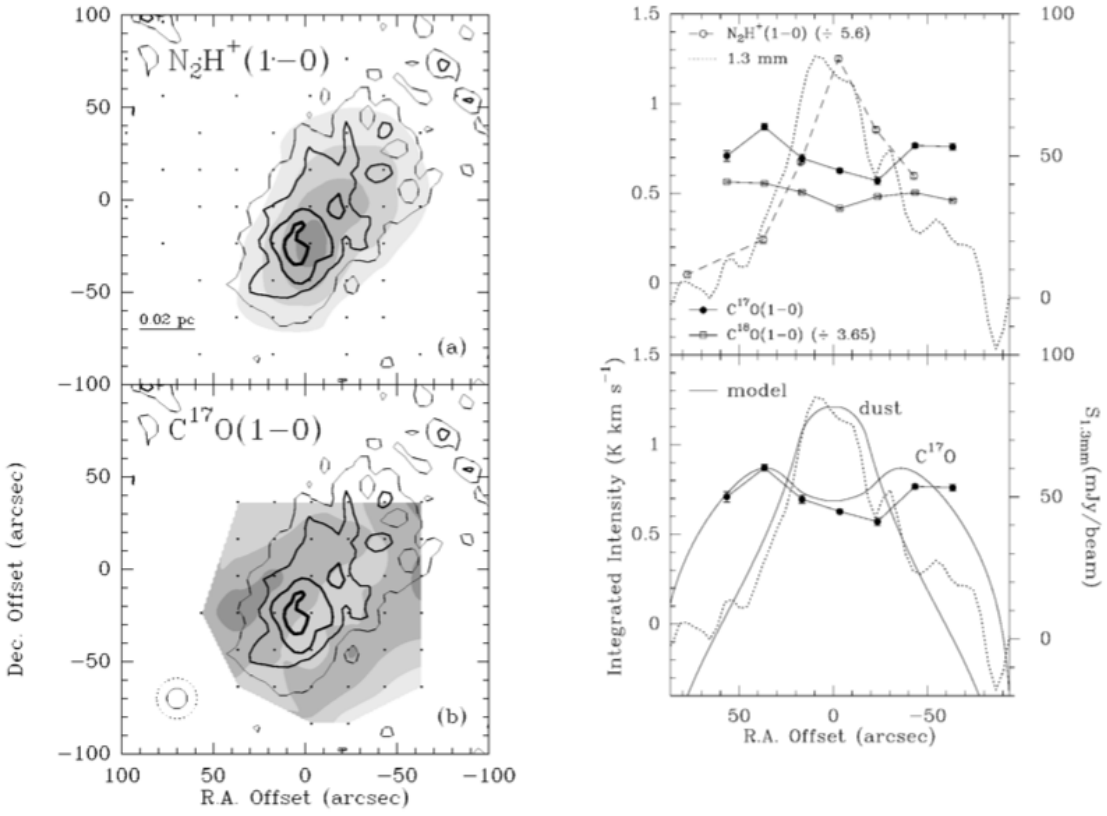

Figure 1.2: The observational result toward L1544 by Caselli et al. (1999). In the left panel, the gray map shows intensities of N_2H^+ (upper) and $C^{17}O$ (lower) and the solid lines shows dust continuum emission. The right panel shows the intensity profiles across the core. (Caselli et al., ApJ, 523, L165, 1999, ©AAS. Reproduced with permission.)

These reactions hardly occur in the gas phase, because they cannot discard the excess energy of the reaction. In contrast, they occur on the grain surface, because grains can absorb the excess energy.

The above story works at low temperature of less than 20 K, where protostars have not been formed. Once protostars are formed and the temperature of the core is raised, molecules formed on dust grains will be evaporated. For example, CO is evaporated at 20 K and CH_3OH at 100 K.

1.3 The deuterium fractionation

The cosmic abundance of D relative to H is about 10^{-5}. However, it is well known that deuterium is fractionated into molecules in cold molecular clouds. Observed D/H ratios of molecules in cold molecular clouds are 0.01 - 0.1, which are much higher than the ratio of the cosmic abundance. This phenomenon is called deuterium fractionation.

The most important mechanism of the deuterium fractionation is the following reactions:

$$H_3^+ + HD \longrightarrow H_2D^+ + H_2 + 230\ \mathrm{K} \tag{1.7}$$

$$H_2D^+ + CO \longrightarrow HCO^+ + HD \tag{1.8}$$

$$H_2D^+ + e \longrightarrow H + HD. \tag{1.9}$$

The reaction (1.7) is exothermic by 230 K. Since the backward reaction is endothermic, it is negligible at low temperature. Hence, the abundance of H_2D^+ is enhanced significantly. Then, deuterium is transferred to various molecules by reactions with H_2D^+, and hence, high deuterium fractionation is realized in various molecules.

In fact, assuming the equilibrium condition, the rate equation is given as:

$$\frac{d[H_2D^+]}{dt} = k[H_3^+][HD] - k[H_2D^+][CO] - k_r[H_2D^+][e] = 0. \tag{1.10}$$

Here, k is the rate coefficient of reaction (1.7) and (1.8), and k_r is the rate coefficien of reaction (1.9). k and k_r show the rate coefficient of the ion-molecule reaction and the dissociative recombination respectively, and their typical values are $k \simeq 2 \times 10^{-9}$ $\mathrm{cm^3 s^{-1}}$, $k_r \simeq 10^{-7}$ $\mathrm{cm^3 s^{-1}}$. Then the $[H_2D^+]/[H_3^+]$ ratio is evaluated by assuming that $[CO] \sim 10^{-4}[H_2]$ and

$[e] \sim 10^{-7}[H_2]$:

$$\frac{[H_2D^+]}{[H_3^+]} = \frac{k[HD]}{k[CO] + k_r[e]} \simeq 10^{-1}. \tag{1.11}$$

Thus, high fractionation is realized.

In equation (1.11), the abundance of CO ([CO]) and the electron ([e]) are involved in the denominator, and hence, the degree of the deuterium fractionation depends on the relative abundance of these two species. In case of no CO depletion, the abundance of CO is much higher than that of electron, as noted above. Then, reaction (1.8) mainly contributes to destruction of H_2D^+. When the abundance of CO becomes 1/10 by the CO depletion, the value of k[CO] is almost same as k_r[e], and the reactions of CO and e (reactions (1.8) and (1.9)) equally contribute. As a result, the $[H_2D^+]/[H_3^+]$ ratio increases. The CO depletion therefore accelerates the deuterium fractionation.

Once a protostar is formed and the temperature at the central part of the core is raised, a situation will change. Then, the backward reaction of reaction (1.7):

$$H_2D^+ + H_2 \longrightarrow H_3^+ + HD - 230K \tag{1.12}$$

can contribute significantly, and the abundance of H_2D^+ decreases. In addition, the CO molecules are evaporated from dust grains at the temperature higher than 20 K, which allow the destruction reaction of H_2D^+:

$$H_2D^+ + CO \longrightarrow HCO^+ + HD. \tag{1.13}$$

Consequently, it is predicted that the deuterium fractionation ratio starts to decrease.

1.4 Background and aims of this thesis

After Caselli et al. (1999) presented an evidence of the CO depletion, extensive studies on the deuterium fractionation have been conducted. Especially, the deuterium fractionation in starless cores was extensively studied. In L1544, deuterated species such as N_2D^+, DCO^+ and H_2D^+ were observed, and it was confirmed that the deuterium fractionation ratios of these species are higher at the center region than in the surrounding region (Caselli et al. 2002; Caselli et al. 2003). As an example, figure 1.3 shows the distribution of the deuterium

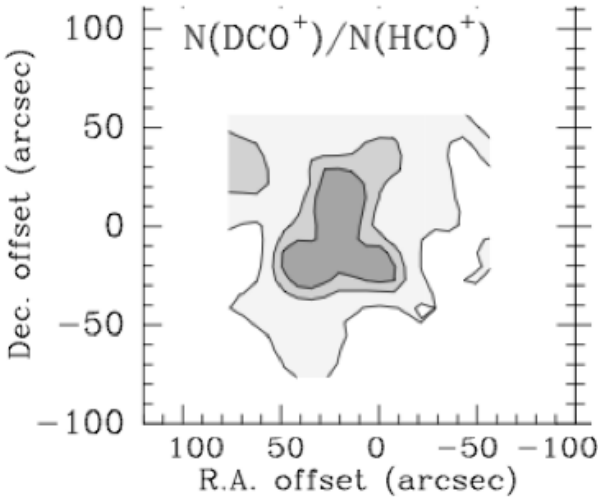

Figure 1.3: The mapping of the DCO^+/HCO^+ ratio toward the starless core L1544 (Caselli et al. 2002) (Caselli et al., ApJ, 565, 344, 2002, ©AAS. Reproduced with permission.)

fractionation ratio $[DCO^+]/[HCO^+]$ in L1544 (Caselli et al. 2002). Deuterium fractionation ratios have widely been used as the evolutionaly tracer of the starless cores.

Deuterium fractionation ratios of various species were also derived in the starless cores (e.g. Wootten et al. 1982; Gerin et al. 2001; Pagani et al. 2007). Moreover, in recent years, multiple deuterated species, where more than one hydrogen atoms in a molecule are substituted by the deuterium atom, were observed. For example, Roueff et al. (2000) discovered the doubly-deuterated ammonia (NHD_2) and derived the deuterium fractionation ratio of $[ND_2H]/[NH_2D]$ toward the dense core, L134N to be 0.05. Lis et al. (2002) detected the triply-deuterated ammonia (ND_3) toward the dark cloud, B1. The multiple deuterated species were also discovered toward the other starless cores (Loinard et al. 2001). Tine et al. (2000) conducted mapping observations of DCO^+, N_2D^+ and NH_2D toward the dark clouds, L134N and TMC1, and the peak of the these species coincides with the ammonia peak. The relationship between the CO depletion and the deuterium fractionation ratios are examined, and it was confirmed that the $[D_2CO]/[H_2CO]$ ratios in molecular clouds became high in the evolved cores (Bacmann et al. 2002; Bacmann et al. 2003). Hirota et al. (2001) observed the DNC/HNC ratios toward nearby dark cloud cores, and found that the DNC/HNC ratios and the NH_3/CCS ratios, which can be racognized as a tracer of the evolutionary stage of the starless core, correlate with each other. Chemical models including the deuterated species

were studied by Roberts et al. (2002). The theoretical studies of the deuterium fractionation on dust grains were conducted to compare with actual observational results (Stantcheva et al. 2003; Roberts et al. 2005).

As mentioned above, various studies on deuterium fractionation of starless cores were conducted. On the other hand, studies on the deuterium fractionation after star formation are still limited. Detections of deuterated species were reported toward various protostars (Parise et al. 2002; Parise et al. 2004; van der Tak et al. 2002; Ceccarelli et al. 1998; Turner et al. 1990). For example, van Dishoeck et al. (1995) detected DCO^+, DNC, HDCO and HDS toward IRAS16293-2422 in the line-survey observation. Toward the other protostars, for example, Sutton et al. (1995) detected HDO and HDCO in the hot core. As for the multiple deuterated species, Caselli et al. (1998) discovered doubly-deuterated formaldehyde toward IRAS16293-2422. Parise et al. (2002) detected doubly-deuterated methanol (CHD_2OH) toward the low-mass protostar forming region, IRAS16293-2422. Parise et al. (2006) and Roberts et al. (2007) observed deuterated formaldehyde and methanol toward the Class 0 protostar and studied formation of the formaldehyde and mathanol on the grain surface. Emprechtinger et al. (2009) observed the N_2D^+/N_2H^+ ratios toward the Class 0 protostars and reported that the N_2D^+/N_2H^+ ratio decreased with the evolution of the Class 0 protostar.

In recent years, studies of gaseous water proceeded, thanks to with the Herschel Space Observatory. With motivations to understand the origin of water on the earth, the HDO/H_2O ratios were studied toward IRAS16293-2422 and NGC1333-IRAS2A, to compare the ratios on the earth (Parise et al. 2005; Liu et al. 2011; Taquet et al. 2013).

Recently, studies on deuterium fractionation toward massive star forming regions has made a significant progress. Sakai et al. (2012) conducted the survey observation of the DNC/HNC ratios toward infrared dark clouds and indicated that the DNC/HNC ratio could not be explained only by the current temperature. Fontani et al. (2014) indicated that the DNC/HNC ratio is less sensitive to the temperature than the N_2D^+/N_2H^+ ratio, and showed that the N_2D^+/N_2H^+ ratio is suitable for identification of high-mass starless cores (HMSC).

Toward low-mass protostars, there are limited studies about the temperature effect of deuterated species. Moreover, most studies were done only for the protostar position. Then, a behavior of the deuterated species after the protostar birth is not well understood. In such a situation, to consider about the variation of the deuterated species, the distribution of the deuterated species around protostars is essential. With this motivation, we conducted the observations of the deuterated species toward the low-mass star forming regions with the single-dish telescopes, the Nobeyama 45 m telescope and the ASTE 10 m telescope. More-

over, we supplementally used the archival data of The Submillimeter Array to resolve detailed structures around the protostars.

1.5 Outline of this thesis

This thesis consist of six chapters. After introduction (Chapter 1), we explain the telescopes used for this thesis and the observed protostars in Chapter 2. In Chapter 3, we present results of the ionic deuterated species. Results of the neutral deutrated species are presented in Chapter 4. We compare the results of the ionic deuterated species and neutral deuterated species in Chapter 5. Chapter 6 conclude the thesis and show the future prospects.

Chapter 2

Telescopes and Target Sources

2.1 Telescopes

2.1.1 Nobeyama 45 m telescope

The Nobeyama 45 m telescope is one of the biggest radio telescopes which can observe millimeter-wave from space. It started the operation in 1982. The radio wave collected by the primary reflector (whose size is 45 m) is guided to receivers through a few reflecting mirrors. The telescope equips 11 receivers. By selecting the reflecting mirrors and the polarization grids, observers can select the receiver for their observation.

Such a large-size telescope as the Nobeyama 45 m telescope is affected by gravitational deformation. To avoid it, the homologous deformation method is employed. Moreover, thermal deformation by the solar radiation also makes significant influences on observational results in daytime observations. To overcome the thermal deformation, the honeycomb sandwich panels, whose surface is covered by the carbon-fiber reinforced plastic having smaller thermal expansion coefficient than metals, are employed for the reflector surface of the Nobeyama 45 m telescope. In addition, the thermal deformation is mitigated by covering the back side of the primary mirror with the insulation panels, which makes rather homogenous temperature of the surface.

Pointing accuracy of the telescope should be better than 1/10 of the beam width in the radio wave observation. For this purpose, the collimator method is employed in the Nobeyama 45 m telescope. In this method, the collimater tower is built on the independent base at the center of the telescope, and is directed to the target source accurately. A difference between

the directions of the primary mirror and the collimator is measured by the optical method, and the primary mirror is moved to point the same direction with the collimater. Moreover, the pointing accuracy can be evaluated from the observations of bright point sources.

Receiver

The radio wave received by the antenna (RF) is introduced into the receiver. There are two types receivers. One is direct amplification of the RF signal by low-noize amplifiers. The second is heterodyne detection, where the RF signal is down-converted to the low frequency (intermediate frequency, IF) signal which is easy to amplify. The direct amplification is used in frequencies lower than 40 GHz, for which low noize amplifiers are available. On the other hand, low noize amplifers are not available for frequencies higher than 40 GHz, and the heterodyne detection method is mainly used. The SIS mixer which is cooled at 4 K is employed as a heterodyne mixer element. The IF signals are amplified and are introduced to the radio spectrometer.

The receivers used for observations in the present studies are the heterodyne type receivers (T100H/V, TZ1H/V, T70H/V). These receivers are the 2SB type SIS receivers. The RF signals are split into two orthogonal polarization components, and they are down-converted separately. For each polarization signal, both USB and LSB signals are observed separately and simultaneously by using two mixers.

The heterodyne receivers mix the RF signal ($\nu_{\rm RF}$) and the local oscillator signal ($\nu_{\rm LO}$), and output the IF signal ($\nu_{\rm LO}$), using devices which have non-linear I-V characteristic. For example, we consider a diode as a non-linear device. We write the I-V characteristic of the non-linear point as:

$$I = a_0 + a_1 V + a_2 V^2 + \cdots . \tag{2.1}$$

When two input signals with frequencies of ω_0 and ω_1 are introduced into this device, V and I become:

$$V = V_0 \cos(\omega_0 t + \phi_0) + V_1 \cos(\omega_1 t + \phi_1), \tag{2.2}$$

and the current proportional to V^2 (I_2) can be written as:

$$\begin{aligned} I_2 &= a_2\left[V_0\cos(\omega_0 t+\phi_0)+V_1\cos(\omega_1 t+\phi_1)\right]^2 \\ &= \frac{a_2}{2}(V_0^2+V_1^2)+\frac{a_2}{2}V_0^2\cos[2(\omega_0 t+\phi_0)] \\ &\quad +\frac{a_2}{2}V_1^2\cos[2(\omega_1 t+\phi_1)]+A_2V_0V_1\cos\left[(\omega_0+\omega_1)t+(\phi_0+\phi_1)\right] \\ &\quad +a_2V_0V_1\cos\left[(\omega_0-\omega_1)t+(\phi_0-\phi_1)\right], \end{aligned} \tag{2.3}$$

where the last term corresponds to the down-converted signal.

In the heterodyne receivers, the following relation holds among $\nu_{\rm RF}$, $\nu_{\rm LO}$ and $\nu_{\rm LF}$:

$$\nu_{\rm IF}=|\nu_{\rm RF}-\nu_{\rm LO}|\,. \tag{2.4}$$

Hence, the receiver is sensitive to the two RF frequencies for the given LO frequency. $\nu_{\rm LO}+\nu_{\rm IF}$ is called USB (upper side band) and $\nu_{\rm LO}-\nu_{\rm IF}$ is called LSB (lower side band). The method in which the both sidebands are observed without distinguishing USB and LSB is called the DSB (double side band) method. The method in which only one of USB and LSB observed is called the SSB (single side band) method. The method which outputs both USB and LSB signals simultaneously by using two mixers is called the 2SB method.

In 2SB method, the input signal is split into two with a mutual phase shift of 90°. Each signal is introduced to a mixer and is mixed with the local oscillator signal for down-conversion to the IF signal. Then, the phase of one of the IF signals is shifted by 90° and the two IF signals are mixed. Here, which USB and LSB can be taken out is determined by which IF signal is phase shifted (figure 2.1).

Writing the USB component of the RF signal as $\cos(\omega_{\rm u}t+\phi_{\rm u})$, the LSB component of the RF signal as $\cos(\omega_{\rm l}t+\phi_{\rm l})$, and the LO signal as $\cos(\omega_{\rm LO}t)$, the USB signal passing through the Mixer 1 is:

$$\cos(\omega_{\rm u}t+\phi_{\rm u})\longrightarrow\cos\left(\omega_{\rm u}t+\phi_{\rm u}+\frac{\pi}{2}\right)\longrightarrow\cos\left[(\omega_{\rm u}-\omega_{\rm LO})t+\phi_{\rm u}+\frac{\pi}{2}\right]. \tag{2.5}$$

The LSB wave passing the Mixer 1 is:

$$\cos(\omega_{\rm l}t+\phi_{\rm l})\longrightarrow\cos\left(\omega_{\rm l}t+\phi_{\rm l}+\frac{\pi}{2}\right)\longrightarrow\cos\left[(\omega_{\rm LO}-\omega_{\rm l})t+\phi_{\rm l}+\frac{\pi}{2}\right]. \tag{2.6}$$

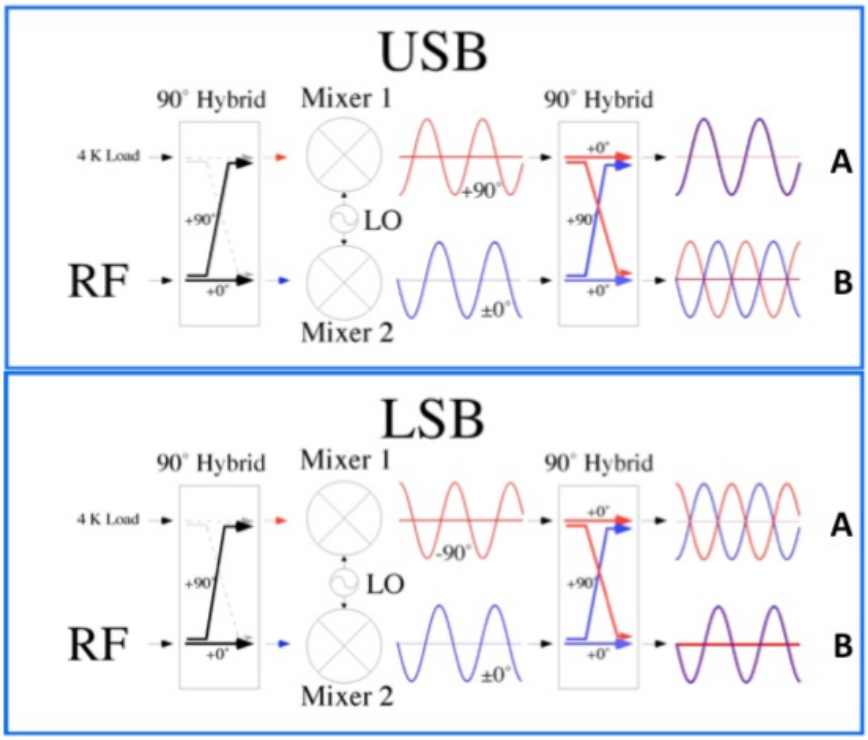

Figure 2.1: The principle of the 2SB method.

The USB wave passing the Mixer 2 is:

$$\cos(\omega_u t + \phi_u) \longrightarrow \cos(\omega_u t + \phi_u) \longrightarrow \cos\left[(\omega_u - \omega_{LO})t + \phi_u\right]. \tag{2.7}$$

The LSB wave passing the Mixer 2 is:

$$\cos(\omega_l t + \phi_l) \longrightarrow \cos(\omega_l t + \phi_l) \longrightarrow \cos\left[(\omega_{LO} - \omega_l)t + \phi_l\right]. \tag{2.8}$$

Then the output signal from A is:

$$2\cos\left((\omega_u - \omega_{LO})t + \phi_u + \frac{\pi}{2}\right) \longrightarrow \text{USB}. \tag{2.9}$$

The output signal from B is:

$$2\cos\left[(\omega_{\rm LO} - \omega_{\rm I}) - \pi_{\rm I}\right] \quad \longrightarrow \quad \text{LSB}. \tag{2.10}$$

Then, we can simultaneously observe the USB and LSB signals.

SIS Mixers

The SIS mixers (Superconductor/Insulator/Superconductor Mixer) are employed for the T100H/V, the TZ1H/V, and T70H/V receivers. The SIS mixer is an application of the Josephson junction, where a very thin insulator film is sandwiched by two superconductor films. When the bias voltage above the gap voltage of the superconducting material is applied between the superconductor films, the tunneling current appears. Even below the bias voltage lower than the gap voltage, tunneling current appears with assistance of photons. This is called as photon assisted tunneling (PAT). This situation is shown in figure 2.2.

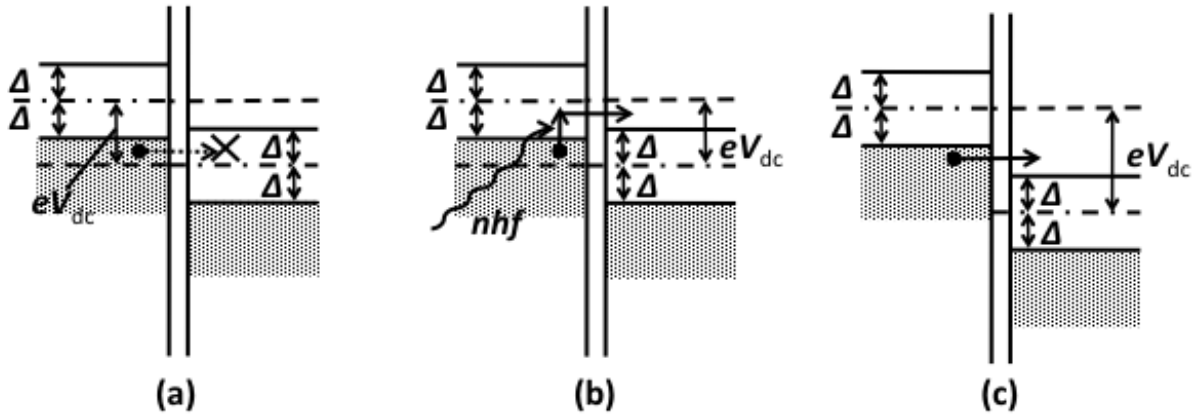

Figure 2.2: The energy state density of the SIS contact.

Typical I-V characteristics of the SIS mixer are schematically shown in figure 2.3. Without the LO signal, the current shows the sharp initial rise at $V_{\rm dc} = 2\Delta/e$, and the SIS mixer shows strong non-linearity. When LO signal is applied, the tunneling current occurs by the PAT mechanism.

When both the RF and LO signals are fed into the SIS element under an appropriate bias voltage ($0 < V_{\rm dc} < 2\Delta/e$), the tunneling current changes by the beat frequency ($\nu_{\rm IF}$). By picking out this component by the low-pass filter, the heterodyne conversion is achieved.

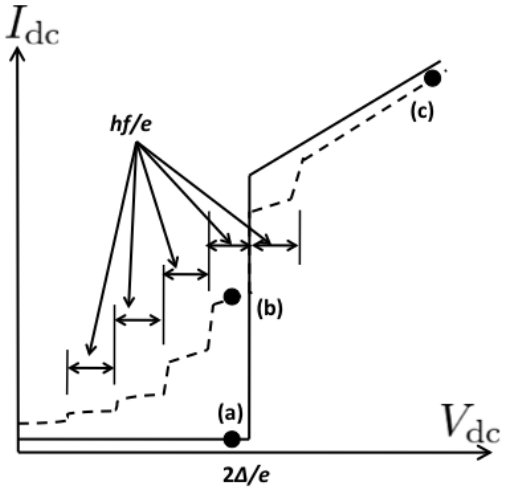

Figure 2.3: The I-V characteristics of the SIS mixer.

T70H/V receiver

There are many spectral lines of the deuterated species of basic molecules in the 70 GHz band. In addition to DCO^+, DNC, DCN, N_2D^+ which we observed in this study, the lines of NH_2D, CCD, HDCO, D_2CO, CH_3CCD, DC_3N also exist in this band. As mentioned in Section 1.3, the deuterium fractionation ratios of molecules play a key role in understanding physical conditions and evolutionary state of molecular clouds. For this purpose, high sensitivity observations at the 70 GHz band are very important. However, the sensitivity of the receivers in the 70 GHz band equipped with the Nobeyama 45 m telescope was a few times worse than that in the 80 - 115 GHz band. Moreover, there is little large aperture telescopes equipped with the high sensitivity receiver for this frequency region in the world. Therefore, we developed a high sensitivity 70 GHz band receiver, and installed it on the Nobeyama 45 m telescope. As a result, the sensitive observations of deuterated species becomes possible. The development and installation were mainly conducted by Dr. Sakai of the University of Electro-Communications, and I also participated in these processes.

2.1.2 ASTE 10 m telescope

The ASTE (Atacama Submillimeter Telescope Experiment) 10 m telescope is located at the Desierto de Atacama (alt. 4860 m) in the northern part of Chile. This telescope is the first 10 m diameter class submillimeter telescope in the southern hemisphere (Sugimoto et al. 2004). The ASTE 10 m telescope was constructed in March of 2002. The surface accuracy of the main reflector is 17 μm, and the pointing accuracy is 2″ in the conditions of the wind velocity of 7 meters per second or lower.

Spectroscopic and continuum observations are possible with the ASTE 10 m telescope. For spectroscopic observations, the CATS 345 receiver which can observe the 324 - 372 GHz region and the ALMA B8QM receiver which can observe the 400 - 500 GHz region are available. Heterodyne receivers are installed on the Cassegrain focus of the antenna. For the observations of the continuum, the AzTEC camera which was installed from 2007 to 2008 was used. Now, the TMS Camera (Bolometer camera) which can observe 270 GHz band and 350 GHz band is being developed.

Observations can be conducted not only at San Pedro de Atacama (Chile) but also in Japan in a remote way. In remote observations, the network observation system, N-COSMOS3 which is developed by the National Astronomical Observatory of Japan (NAOJ) is used.

2.1.3 The Submillimeter Array

The submillimeter Array (SMA) (Paul T. P. Ho et al. 2004) is a submillimeter interferometer located at Mauna Kea in Hawaii. This telescope is operated by the Smithsonian Astrophysical Observatory (SAO) in the United State and the Academia Sinica Institute of Astronomy and Astrophysics (ASIAA) in Taiwan communally. The SMA consists of eight telescopes of 6 meter in diameter, and started the operation in November 2003. The SMA can observe the 230 GHz, 345 GHz, 400 GHz and 690 GHz bands. The maximum baseline can be as long as 509 m, which realizes the maximum resolution of up to 0.1 arcsecond. Basically four configurations are possible, and the typical resolutions are: subcompact (5 arcsec at 345 GHz), compact (2.5 arcsec at 345 GHz), extended (0.7 arcsec at 345 GHz) and very extended (0.1 arcsec at 345 GHz). Data analyses were conducted by MIR for the calibration, and Miriad for the imaging analyses. In this study, we partly used the released archival data for investigating detailed distribution of molecules around protostars for some sources.

2.2 Target Sources

In this study, we observed with the Nobeyama 45 m telescope and with the ASTE 10 m telescope. With these telescopes (the spacial resolution of about 20 ″), we must resolve the 20 K region where the deuterium fractionation ratio is considered to change Hence, we considered nearby (nearer than 300 pc) and bright (brighter than 10 $L_{\odot}$) protostars. Additionally, we selected the sources in three different evolutionary stages, Class I, Class I/0 and Class 0. As the target protostars which satisfy the above requirements, we chose Class I protostars L1551-IRS5 and L1251A, Class I/0 protostar L483, and Class 0 protostars IRAS16293-2422 and NGC1333-IRAS2A.

2.2.1 Low-mass protostar L1551-IRS5

L1551-IRS5 in Taurus is the Class I protostar discovered by Strom et al. (1976). The distance from the sun is about 140 pc. Snell et al. (1980) discovered the bipolar molecular outflow toward this source by the observation of ^{12}CO($J = 1 - 0$, $J = 2 - 1$) and ^{13}CO($J = 1 - 0$). Kaifu et al. (1984) found a rotating gas disk prependicular to the outflow direction by the observation of CS ($J = 1 - 0$). From these results, L1551-IRS5 is considered as a typical example of a formation site of a low-mass protostar.

By interferometer observations of the CO ($J = 1 - 0$) line, Momose et al. (1998) found the following two components around L1551-IRS5: the component concentrating around the center and the component extending toward the direction of north and south. The size of the concentrated component is 2380×1050 AU and this component has a flattened shape perpendicular to the molecular outflow. This seems to be a circumstellar envelope around L1551-IRS5. By detailed analyses of the position-velocity diagram, the effect of the gravity outward of the envelope is found to be reduced by the gas pressure and magnetic pressure: The velocity structure at the centrifugal radius departs from the Keplerian rotation.

Moreover, L1551-IRS5 is used for the study of the detail structure of the molecular outflow. Wu et al. (2009) showed that the size of the molecular outflow is about 1.5 pc, and the outflow blows toward the northwestward direction in redshift and the southeastward in blueshift by the CO ($J = 1 - 0$) observation.

The protostar of the L1551-IRS5 itself is a close-binary system. However, this thesis concentrates on the core-scale distribution of deuterium fractionation ratios, and hence, we co not take into account of the binary.

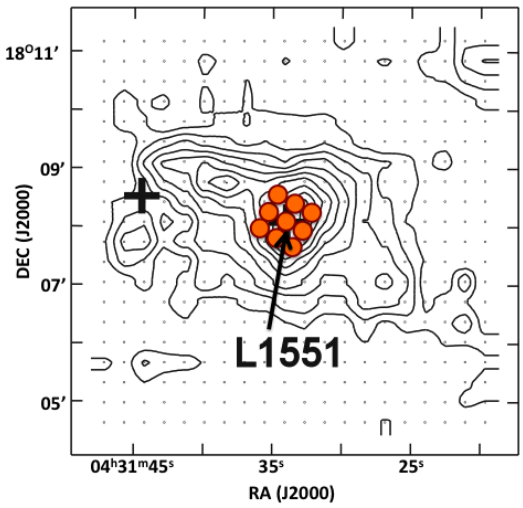

Figure 2.4: The distribution of N_2H^+ ($J = 1 - 0$) by Tatematsu et al. (2004). The orange circles show the observed positions. The sizes of these circles denote beam. (Tatematsu et al., ApJ, 606, 333, 2004, ©AAS. Reproduced with permission.)

2.2.2 Low-mass protostar L483

L483 is one of solar-type protostars discovered by Parker et al. (1988). L483 is located in the Aquila Rift, and the distance of L483 from the sun is about 200 pc (Dame et al. 1985). The luminosity of L483 is $\sim 10 L_{\odot}$, and hence, this is a relatively bright protostar. L483 is associated with H_2O maser (Xiang et al. 1995). Observations of ammonia show that the core of L483 is concentrated around the protostar with a strong velocity gradient along the core (Goodman et al 1993; Fuller et al. 1993; Anglada et al. 1997; Fuller et al. 2000).

L483 has been classified as a Class 0 protostar for a long time. Tafalla et al. (2000) showed from observations of H_2CO, SiO and CH_3OH toward the outflow that L483 shows the characteristics of Class 0 protostar such as the gas heating and H_2CO abundance enhancement. On the other hand, the characteristics of the Class I protostar as the weakness of the outflow wing of SiO and CH_3OH can also be recognized. From these results, L483 is now considered to be in a transition phase from Class 0 to Class I, that is, Class I/0 protostar (Tafalla et al. 2000). A dynamical age of the outflow of CO is about 10^4 years (Tafalla et al. 2000).

There are many studies on the envelope of L483. Millimeter-wave spectral lines of CS and H_2CO toward the protostar show the infalling asymmetry. For this reason, L483 is

considered as a candidate of a protostar which has the infalling gas motion in the ambient envelope (Myers et al 1995; Mardones et al. 1997). It was shown by observations of millimeter and centimeter-wave observation of NH_3, N_2H^+ and CH_3OH that the envelope is extended toward the east-west direction and the velocity structure is similar to the associated molecular outflow. From this result, it is confirmed that the dense gas in the outer envelope is influenced by the outflow (Gregersen et al. 1997; Fuller et al. 2000; Park et al. 2000; Tafalla et al. 2000). In addition, the detailed studies on chemical differentiation of the envelope have been conducted (Jϕrgensen et al. 2002; Jϕrgensen et al. 2004). Takakuwa et al. (2007) shows the distribution of the relatively high temperature dense gas by submillimeter-wave observations of CS and HCN.

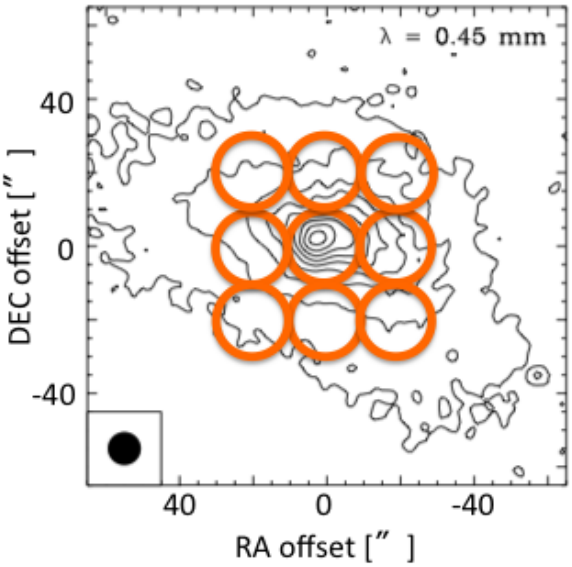

Figure 2.5: The dust continuum map toward L483 (Jϕrgensen, 2004). The orange circles show the observed positions. The sizes of these circles denote beam. (Jϕrgensen, A&A, 424, 589, 2004, reproduced with permission ©ESO.)

2.2.3 Low-mass protostar IRAS16293-2422

IRAS16293-2422 is a Class 0 protostar located in Ophiuchus at a distance from the sun of about 160 pc (Remijan et al. 2006; Yeh et al. 2008). This source is accompanied by the complicated-shape molecular outflow (Mizuno et al. 1990; Hirano et al. 2001). The

existence of the small scale outflows is also suggested by Yeh et al. (2008).

High resolution observations reveal that IRAS16293-2422 is a young binary system (Wootten et al. 1987; Mundy et al. 1992). Mundy et al. (1992) show by the high resolution observation of the millimeter continuum ($4''.5 \times 2''.5$) that IRAS16293-2422 is composed of two objects named MM1 and MM2, whose are separated by 840 AU. The most millimeter wave dust emission comes from the region within 300 AU from each object, and the mass of each object is lower than 0.5 $M_{\odot}$. The total balometric luminosity is 30 - 40 $L_{\odot}$, which is mainly caused by the gas accretion.

Moreover, IRAS16293-2422 is the first protostar recognized as a 'hot corino' source (Cazaux et al. 2003). Until then, it was considered that so called 'hot core', where various organic molecules are evaporated into the gas phase from the dust grain by the effect of the temperature rise associated with the protostar formation, are known only in the high-mass star forming regions. However, it was confirmed that such hot core (hot corino) also exists even around low-mass or intermediate-mass protostars.

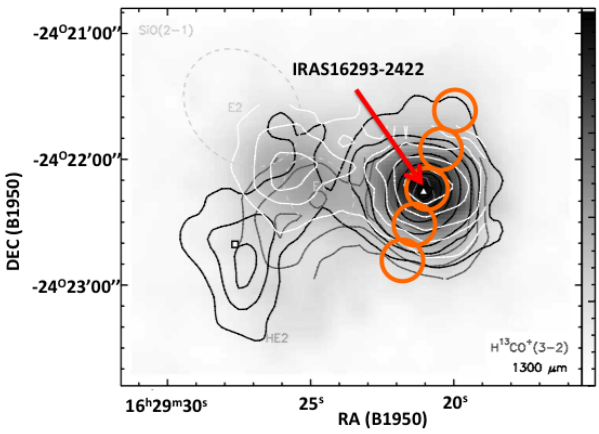

Figure 2.6: The distribution of dust continuum emission (black contours), HCO^+ ($J = 3-2$) (gray scale image), $H^{13}CO^+$ ($J = 3-2$) (gray contours) and HCN ($J = 3-2$) (white contours) by Lis et al. (2002). The orange circles show the observed positions. The sizes of these circles denote beam. (Lis et al., ApJ, 569, 322, 2002, ©AAS. Reproduced with permission.)

2.2.4 Low-mass protostar NGC1333-IRAS2A

NGC1333-IRAS2A is first detected by the IRAS observation (Jennings et al.1987). NGC1333-IRAS2A is a solar-type protostar located in the NGC1333 molecular cloud in the Perseus (Cernis et al. 1990). The distance of NGC1333-IRAS2A from the sun had been considered to be 220 pc (Cernis et al. 1990), but this distance was corrected to 235 pc by Hirota et al. (2008). The bolometric luminosity of NGC1333-IRAS2A is 16 $L_{\odot}$. NGC1333-IRAS2A is a binary system composed of three different objects, NGC1333-IRAS2A, NGC1333-IRAS2B and NGC1333-IRAS2C (Looney et al. 2000; Sandell et al. 2001). NGC1333-IRAS2B is located about 30″ south-east of NGC1333-IRAS2A, and NGC1333-IRAS2C is located north-west of NGC1333-IRAS2A respectively. NGC1333-IRAS2A and NGC1333-IRAS2B are distinguished from each other in the mid-infrared image with Spitzer Space Telescope (Jϕrgensen et al. 2007; Gutermuth et al. 2008). These objects show compact emission in the millimeter wave images (Looney et al. 2000; Jϕrgensen et al. 2004). NGC1333-IRAS2C is considered to be a starless core, because it shows strong emission of N_2H^+ and no 3 mm continuum (Jϕrgensen et al. 2004).

In this region, a large-scale outflow is known to exist in the direction of NNE-SSW (Sandell et al. 1994; Knee et al. 2000). Liseau et al. (1988) showed from the observation of CO that there exist two outflows toward NGC1333-IRAS2A. The two outflows are originated from the two positions separated by a few arcseconds, and hence, NGC1333-IRAS2A itself is likely a binary system. Each star of the binary is thought to be in the different evolutionary stage, judging from the difference of the timescale of the two outflows (Knee et al. 2000).

NGC1333-IRAS2A is a hot corino source as in the case of IRAS16293-2422 (Jϕrgensen et al. 2005). Many organic molecules including $HCOOCH_3$ and CH_3OH were observed toward NGC1333-IRAS2A (Bottinelli et al. 2007). Deuterium fractionation ratios of various molecules toward the envelope were also studied. The $HDCO/H_2CO$ ratio is reported in ~ 0.17 and the CH_2DOH/CH_3OH is ~ 0.62. These ratios are higher than those toward IRAS16293-2422 (Parise et al. 2004).

2.2.5 Low-mass protostar L1251A

L1251A is a Class I protostar located at the northern part of the L1251 molecular cloud (Mardones et al. 1997). The L1251 molecular cloud is in the molecular ring in Cepheus Flare, and is elongated in the east-west direction. The distance from the sun is about 300 pc based on the color excess (Kun et al. 1993; Itziar et al. 2006). L1251 is a bright protostar

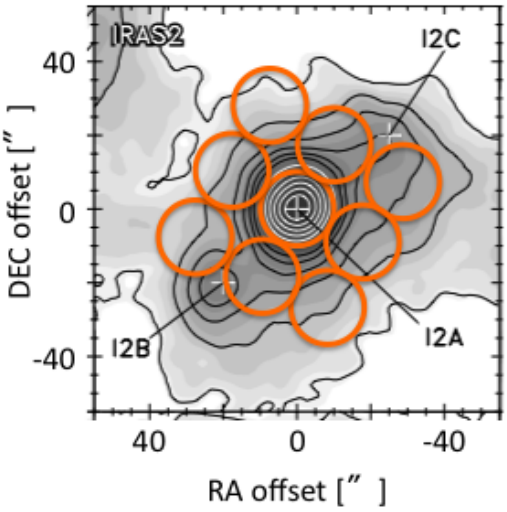

Figure 2.7: The SCUBA map of the dust continuum emission toward NGC1333-IRAS2A (Jørgensen et al., 2007). The orange circles show the observed positions. The sizes of these circles denote beam. (Jørgensen et al., ApJ, 659, 479, 2007, ©AAS. Reproduced with permission.)

whose bolometric luminosity is 27 $L_{\odot}$ (Itziar et al. 2006). Kun et al. (1998) estimated the mass of the hypethetical central star to be 2.35 $M_{\odot}$. Herbig-Haro objects (Balazs et al. 1992; Eiroa et al. 1994) and the H_2O maser (Wilking et al. 1994; Xiang et al. 1995; Claussen et al, 1996) were observed near L1251A. Sato et al. (1989) found the CO outflow in this source, where dynamical age is as about 10^5 years. Balazs et al. (1992) reported the optical jet in this source, whose axis coincide with that of the CO outflow.

Nikolić et al. (2003) conducted mapping observations of HCN, HNC, HCO^+ and CS toward star forming cores in the L1251 molecular cloud (figure 2.8). The dynamical age of the HCO^+ wing emission is an order of magnitude less than that of CO, and origins of these two outflows would be different. It was confirmed that there were two protostellar objects in L1251A by the centimeter wave observation (Beltrán et al. 2001). Either of these two objects would be an origin of the CO outflow.

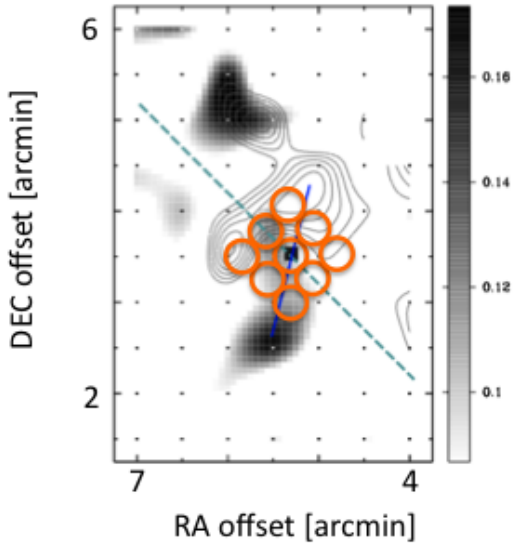

Figure 2.8: The distribution the HCO^+ line toward L1251A (Nikolić et al. 2003). The contour map shows the distribution of red-shifted HCO^+ and gray-scale map shows the distribution of blue-shifted HCO^+. The solid line shows the disk position, and the dotted line shows the direction of CO outflow. The orange circles show the observed positions. The sizes of these circles denote beam. (Nikolić et al., A&A, 409, 941, 2003, reproduced with permission ©ESO.)

Chapter 3

Deuterium Fractionation of Ionic Species

3.1 Observations

In order to examine the behavior of deuterated species after the birth of protostar, we conducted the observation of the deuterated species. At first, we studied deuterated species for ionic species. The observation was conducted toward L1551-IRS5, L1251A, L483, IRAS16293-2422 and NGC1333-IRAS2A with the Nobeyama 45 m telescope, and toward L483, IRAS16293-2422 and NGC1333-IRAS2A with the ASTE 10 m telescope.

The observation toward L1551-IRS5 was conducted in January and February, 2011 and April, 2013, toward IRAS16293-2422 in January and February, 2011, and toward NGC1333-IRAS2A and L1251A in March, 2014. The observed positions are shown in table 3.1. Toward IRAS16293-2422, we conducted a 5-point strip scan centered at the protostar position, which is vertical to the outflow. For the other protostars, we conducted 9-point observations centered at the protostar position. The observed molecular lines are $J = 1 - 0$ lines of DCO^+, $H^{13}CO^+$, $HC^{18}O^+$, N_2D^+ and N_2H^+ toward L1551-IRS5 and IRAS16293-2422, and $J = 1 - 0$ lines of DCO^+, $H^{13}CO^+$, $HC^{18}O^+$ and N_2H^+ toward L483, NGC1333-IRAS2A and L1251A (table 3.2). For the telescope pointing, we observed the SiO maser sources: NML-Tau for L1551-IRS5, IRC-10414 for L483, U-Ari for NGC1333-IRAS2A, RS-Lib for IRAS16293-2422 and IRAS22480+6002 for L1251A.

In the observation in 2011, we used the T100H/V receiver and the S100 receiver for 70 GHz observations, and T100H/V receiver for 90 GHz observations. In the observation in 2013, we used the TZH/V receiver for all the observations. In 2014, we used the T70H/V receiver for 70 GHz and 80 GHz observations, whereas we used the TZH/V receiver for

L1551-IRS5		
No.	RA(J2000)	DEC(J2000)
1	$+04^h\ 31^m\ 34^s.8$	$+18°\ 08'\ 31''.3$
2	$+04^h\ 31^m\ 35^s.4$	$+18°\ 08'\ 13''.1$
3	$+04^h\ 31^m\ 36^s.0$	$+18°\ 07'\ 54''.9$
4	$+04^h\ 31^m\ 33^s.6$	$+18°\ 08'\ 23''.0$
5	$+04^h\ 31^m\ 34^s.2$	$+18°\ 08'\ 04''.8$
6	$+04^h\ 31^m\ 34^s.7$	$+18°\ 07'\ 46''.6$
7	$+04^h\ 31^m\ 32^s.3$	$+18°\ 08'\ 14''.7$
8	$+04^h\ 31^m\ 32^s.9$	$+18°\ 07'\ 56''.5$
9	$+04^h\ 31^m\ 33^s.5$	$+18°\ 07'\ 38''.3$

L1251A		
No.	RA(J2000)	DEC(J2000)
1	$+22^h\ 35^m\ 24^s.3$	$+75°\ 17'\ 34''.3$
2	$+22^h\ 35^m\ 28^s.0$	$+75°\ 17'\ 20''.1$
3	$+22^h\ 35^m\ 31^s.7$	$+75°\ 17'\ 06''.0$
4	$+22^h\ 35^m\ 20^s.6$	$+75°\ 17'\ 20''.1$
5	$+22^h\ 35^m\ 24^s.3$	$+75°\ 17'\ 06''.0$
6	$+22^h\ 35^m\ 28^s.0$	$+75°\ 16'\ 51''.9$
7	$+22^h\ 35^m\ 16^s.9$	$+75°\ 17'\ 06''.0$
8	$+22^h\ 35^m\ 20^s.6$	$+75°\ 16'\ 51''.9$
9	$+22^h\ 35^m\ 24^s.3$	$+75°\ 16'\ 37''.7$

L483		
No.	RA(J2000)	DEC(J2000)
1	$+18^h\ 17^m\ 31^s.1$	$-04°\ 39'\ 18''.0$
2	$+18^h\ 17^m\ 31^s.1$	$-04°\ 39'\ 38''.0$
3	$+18^h\ 17^m\ 31^s.1$	$-04°\ 39'\ 58''.0$
4	$+18^h\ 17^m\ 29^s.8$	$-04°\ 39'\ 18''.0$
5	$+18^h\ 17^m\ 29^s.8$	$-04°\ 39'\ 38''.0$
6	$+18^h\ 17^m\ 29^s.8$	$-04°\ 39'\ 58''.0$
7	$+18^h\ 17^m\ 28^s.5$	$-04°\ 39'\ 18''.0$
8	$+18^h\ 17^m\ 28^s.5$	$-04°\ 39'\ 38''.0$
9	$+18^h\ 17^m\ 28^s.5$	$-04°\ 39'\ 58''.0$

NGC1333-IRAS2A		
No.	RA(J2000)	DEC(J2000)
1	$+03^h\ 28^m\ 56^s.0$	$+31°\ 15'\ 02''.0$
2	$+03^h\ 28^m\ 56^s.8$	$+31°\ 14'\ 44''.4$
3	$+03^h\ 28^m\ 57^s.5$	$+31°\ 14'\ 26''.7$
4	$+03^h\ 28^m\ 54^s.7$	$+31°\ 14'\ 52''.7$
5	$+03^h\ 28^m\ 55^s.4$	$+31°\ 14'\ 35''.0$
6	$+03^h\ 28^m\ 56^s.1$	$+31°\ 14'\ 17''.3$
7	$+03^h\ 28^m\ 53^s.3$	$+31°\ 14'\ 43''.3$
8	$+03^h\ 28^m\ 54^s.0$	$+31°\ 14'\ 25''.6$
9	$+03^h\ 28^m\ 54^s.8$	$+31°\ 14'\ 08''.0$

IRAS16293-2422		
No.	RA(J2000)	DEC(J2000)
4u	$+16^h\ 32^m\ 23^s.5$	$-24°\ 29'\ 10''.4$
4′	$+16^h\ 32^m\ 23^s.1$	$-24°\ 28'\ 51''.3$
5	$+16^h\ 32^m\ 22^s.6$	$-24°\ 28'\ 32''.2$
6′	$+16^h\ 32^m\ 22^s.2$	$-24°\ 28'\ 13''.1$
6d	$+16^h\ 32^m\ 21^s.7$	$-24°\ 27'\ 54''.0$

Table 3.1: Observed positions of Nobeyama 45 m telescope.

molecules	frequency [GHz]
DCO^+ ($J = 1 - 0$)	72.0393124
$H^{13}CO^+$ ($J = 1 - 0$)	86.7542884
$HC^{18}O^+$ ($J = 1 - 0$)	85.1622231
N_2D^+ ($J = 1 - 0$)	77.1092433
N_2H^+ ($J = 1 - 0$)	93.1733922

Table 3.2: Spectral lines observed with the Nobeyama 45 m telescope. The frequencies are taken from CDMS (http://www.astro.uni-koeln.de/cdms/).

90 GHz observations. For the telescope pointing, we used the H40 receiver. The system noise temperature in observations is summarized in table 3.3. The S100 receiver shows poor system noise temperature, because it does not work well at the 70 GHz band. For observations in 2011, we used AOS spectrometer (Acousto-Optical Spectrometer), while we used SAM45 spectrometer (correlators) in 2013 and 2014.

year	Object	T100H/V	S100	TZ1H/V	T70H/V
2011	L1551-IRS5	130 K - 250 K	470 K - 490 K		
	IRAS16293-2422	170 K - 390 K	530 K - 580 K		
2013	L1551-IRS5			166 K - 255 K	
2014	L483			120 K - 199 K	149 K - 239 K
	NGC1333-IRAS2A			123 K - 199 K	150 K - 227 K
	L1251A			136 K - 219 K	153 K - 236 K

Table 3.3: System temperatures of Nobeyama 45 m telescope

Observations with the ASTE 10 m telescope were conducted in July and August in 2014. The observed protostars are L483, NGC1333-IRAS2A and IRAS16293-2422. The observed potions are shown in table 3.4. We observed 9 positions toward L483 and 5 positions toward NGC1333-IRAS2A and IRAS16293-2422 centered at the protostar position. The observed lines are the $J = 5 - 4$ lines of DCO^+ and the $J = 4 - 3$ lines of $H^{13}CO^+$ (table 3.5). We can not observe the same transition of DCO^+ and $H^{13}CO^+$ with the ASTE 10 m telescope. For the telescope pointing, we observed the CO ($J = 3 - 2$) lines toward W-Aql for L483, NML-Tau for NGC1333-IRAS2A and R-Aql for IRAS16293-2422.

We used the CATS345 receiver. The system noise temperature in the observation was 202 K - 851 K for L483, 230 K - 541 K for NGC1333-IRAS2A and 226 K - 369 K for

L483		
No.	RA(J2000)	DEC(J2000)
1	$+18^h\ 17^m\ 31^s.1$	-04° 39′ 18″.0
2	$+18^h\ 17^m\ 31^s.1$	-04° 39′ 38″.0
3	$+18^h\ 17^m\ 31^s.1$	-04° 39′ 58″.0
4	$+18^h\ 17^m\ 29^s.8$	-04° 39′ 18″.0
5	$+18^h\ 17^m\ 29^s.8$	-04° 39′ 38″.0
6	$+18^h\ 17^m\ 29^s.8$	-04° 39′ 58″.0
7	$+18^h\ 17^m\ 28^s.5$	-04° 39′ 18″.0
8	$+18^h\ 17^m\ 28^s.5$	-04° 39′ 38″.0
9	$+18^h\ 17^m\ 28^s.5$	-04° 39′ 58″.0

NGC1333-IRAS2A		
No.	RA(J2000)	DEC(J2000)
2	$+03^h\ 28^m\ 56^s.8$	+31° 14′ 44″.4
4	$+03^h\ 28^m\ 54^s.7$	+31° 14′ 52″.7
5	$+03^h\ 28^m\ 55^s.4$	+31° 14′ 35″.0
6	$+03^h\ 28^m\ 56^s.1$	+31° 14′ 17″.3
8	$+03^h\ 28^m\ 54^s.0$	+31° 14′ 25″.6

IRAS16293-2422		
No.	RA(J2000)	DEC(J2000)
2	$+16^h\ 32^m\ 22^s.4$	-24° 28′ 35″.6
4	$+16^h\ 32^m\ 22^s.9$	-24° 28′ 15″.6
5	$+16^h\ 32^m\ 22^s.9$	-24° 28′ 35″.6
6	$+16^h\ 32^m\ 22^s.9$	-24° 28′ 55″.6
8	$+16^h\ 32^m\ 21^s.4$	-24° 28′ 35″.6

Table 3.4: Observed positions of ASTE 10 m telescope.

molecules	frequency [GHz]
DCO^+ ($J = 5 - 4$)	360.1697783
$H^{13}CO^+$ ($J = 4 - 3$)	346.998344

Table 3.5: Spectral lines observed by ASTE 10 m telescope. The frequencies are taken from CDMS (http://www.astro.uni-koeln.de/cdms/).

IRAS16293-2422. We used MAC spectrometer for spectral line observations.

3.2 Results

3.2.1 Spectral line profile

L1551-IRS5

Figure 3.1 shows the spectra observed with the Nobeyama 45 m telescope toward L1551-IRS5. The red number shown in the upper-left part of each spectrum shows the observed positions (table 3.1). The observation time for DCO^+ and $H^{13}CO^+$ toward the disk direction (positions 4, 5 and 6) is longer than toward other positions, and the S/N ratio is better at those positions. The DCO^+ line is strong at positions 1, 2, 3, 7, 8 and 9, whereas it is weak at the protostar position (position 5). The line intensities toward the disk direction seem to be relatively weak. In contrast, the spectrum of $H^{13}CO^+$ is stronger at the protostar position (position 5) than at the peripheral positions. The lines in the disk direction are stronger than other positions. The rare isotopic species $HC^{18}O^+$ shows a similar trend to $H^{13}CO^+$.

We also observed the hyperfine-resolved spectral lines of N_2D^+ and N_2H^+. N_2D^+ is relatively weak at the protostar position (position 5). In addition, the intensity toward the disk positions seems to be relatively weak: N_2D^+ shows the same trend as DCO^+. On the other hand, the N_2H^+ line intensity seems to show different distribution from the $H^{13}CO^+$ line.

L483

Figure 3.2 shows the spectra observed toward L483 with the Nobeyama 45 m telescope. Each red number shows the observed position. The DCO^+ line is strong at the positions 8 and 9, and is not strong at the protostar position. The spectral intensities of the $H^{13}CO^+$ and $HC^{18}O^+$ lines are strong at the protostar position, and their distributions seem to different from that of DCO^+. They are rather similar to the N_2H^+ distribution, although the N_2H^+ lines are affected by self-absorption effects.

With the ASTE 10 m telescope, we detected the DCO^+ line with a good S/N ratio toward protostar position (position 5), while they are faint at positions 2, 4, 6 and 8 probably due

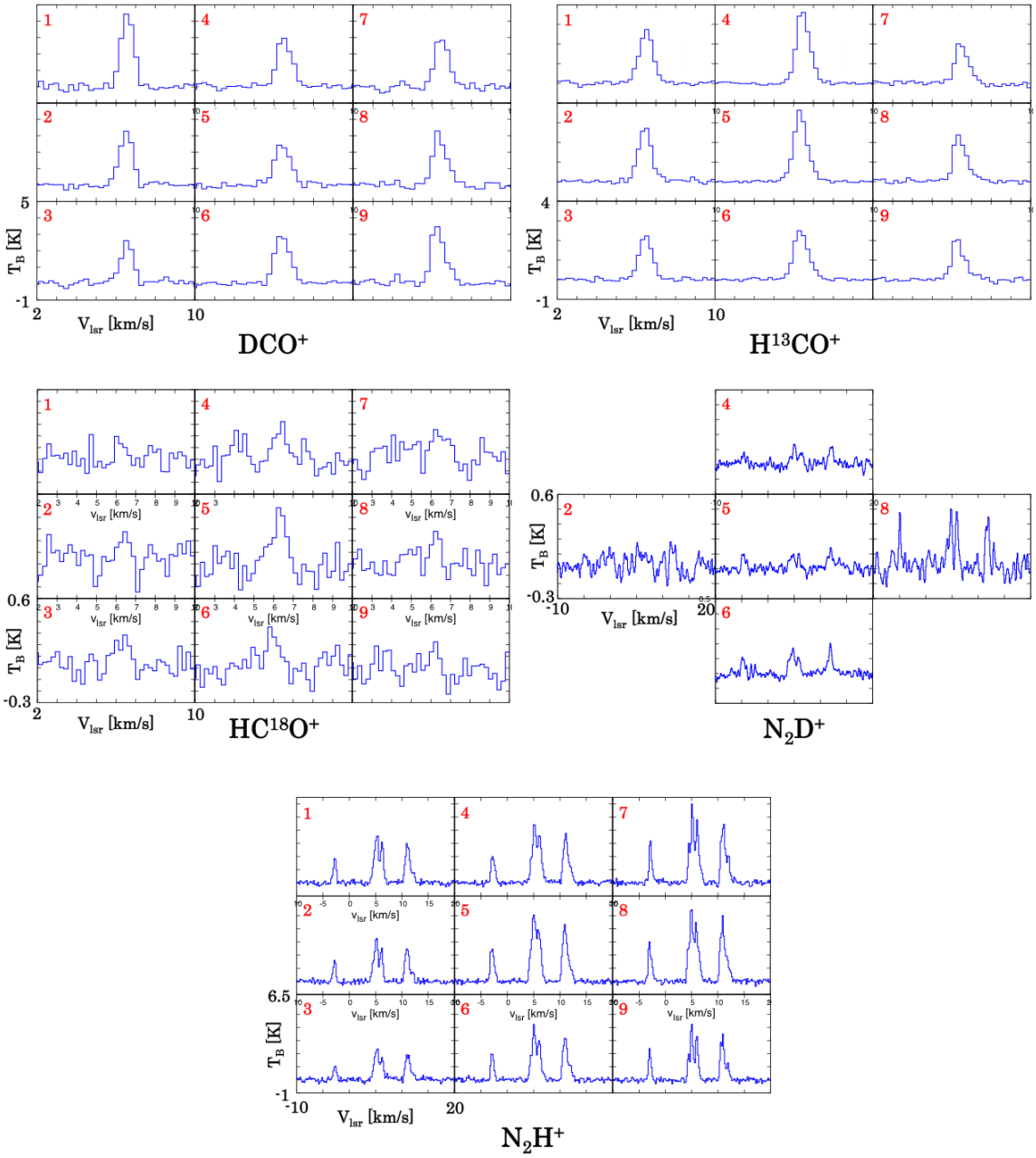

Figure 3.1: Spectra observed toward L1551 with the Nobeyama 45 m telescope.

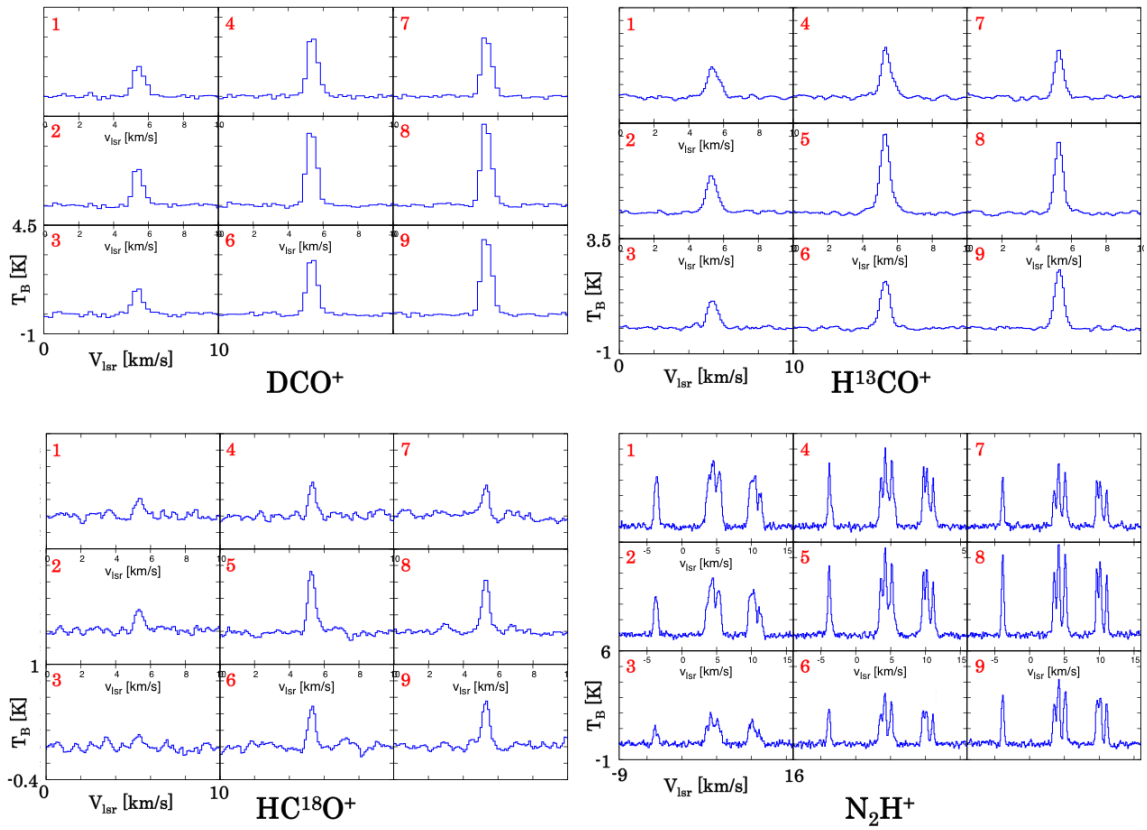

Figure 3.2: Spectra observed toward L483 with the Nobeyama 45 m telescope.

to insufficient excitation conditions of low H_2 density (figure 3.3). The $H^{13}CO^+$ line was detected at positions 5 and 8.

NGC1333-IRAS2A

Figure 3.4 shows the spectra observed with Nobeyama 45 m telescope toward NGC1333-IRAS2A. We show the observed positions in the red number in each spectra. The DCO^+ line is strong at the protostar position and positions 8 and 9. The intensitis at the positions 1, 2 and 3 are weaker than that at positions 7, 8 and 9. On the other hand, the $H^{13}CO^+$ line is strong at the protostar position and weak at positions 8 and 9. The $H^{13}CO^+$ distribution shows different trend from that of DCO^+. This trend for $H^{13}CO^+$ can be also seen in the

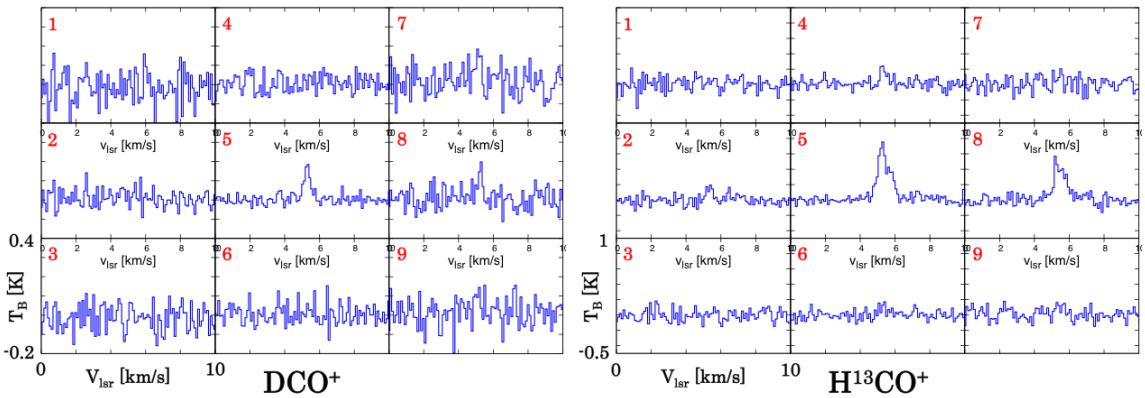

Figure 3.3: Spectra observed toward L483 with the ASTE 10 m telescope.

$HC^{18}O^+$ line. The $HC^{18}O^+$ line is strong at the protostar position as in the case of $H^{13}CO^+$. A similar distribution is also seen in the N_2H^+ line.

With the ASTE 10 m telescope, we could hardly detect the molecular line other than at the protostar position as in the case of L483 (figure 3.5). The weak DCO^+ line were observed at positions 6 and 8. The $H^{13}CO^+$ line was detected at positions 4 and 6. Both DCO^+ and $H^{13}CO^+$ are strong at the protostar position. This trend is the same as the case of L483.

IRAS16293-2422

Figure 3.6 shows the spectra observed toward IRAS16293-2422 with the Nobeyama 45 m telescope. The observed positions are shown in red numbers. The DCO^+ line is strong at the protostar position (position 5) and position 4. This is an opposite behavior to the density tracer N_2H^+. $H^{13}CO^+$ and $HC^{18}O^+$ also show the behavior similar to N_2H^+.

With the ASTE 10 m telescope, both DCO^+ and $H^{13}CO^+$ were detected at all positions (figure 3.7). Since IRAS16293-2422 is a bright protostar, a high temperature region seems to be widely extended. Both DCO^+ and $H^{13}CO^+$ are strong toward the protostar position, and, the line width of $H^{13}CO^+$ seems to be broadened at the protostar position.

L1251A

Molecular lines observed toward L1251A with the Nobeyama 45 m telescope are generally weaker than those observed toward the other four protostars. The DCO^+ and $H^{13}CO^+$ lines are relatively strong at positions 3 and 6. The S/N ratio of N_2H^+ is not very good, but the hyperfine structure is recognized. N_2H^+ is strongest at position 9.

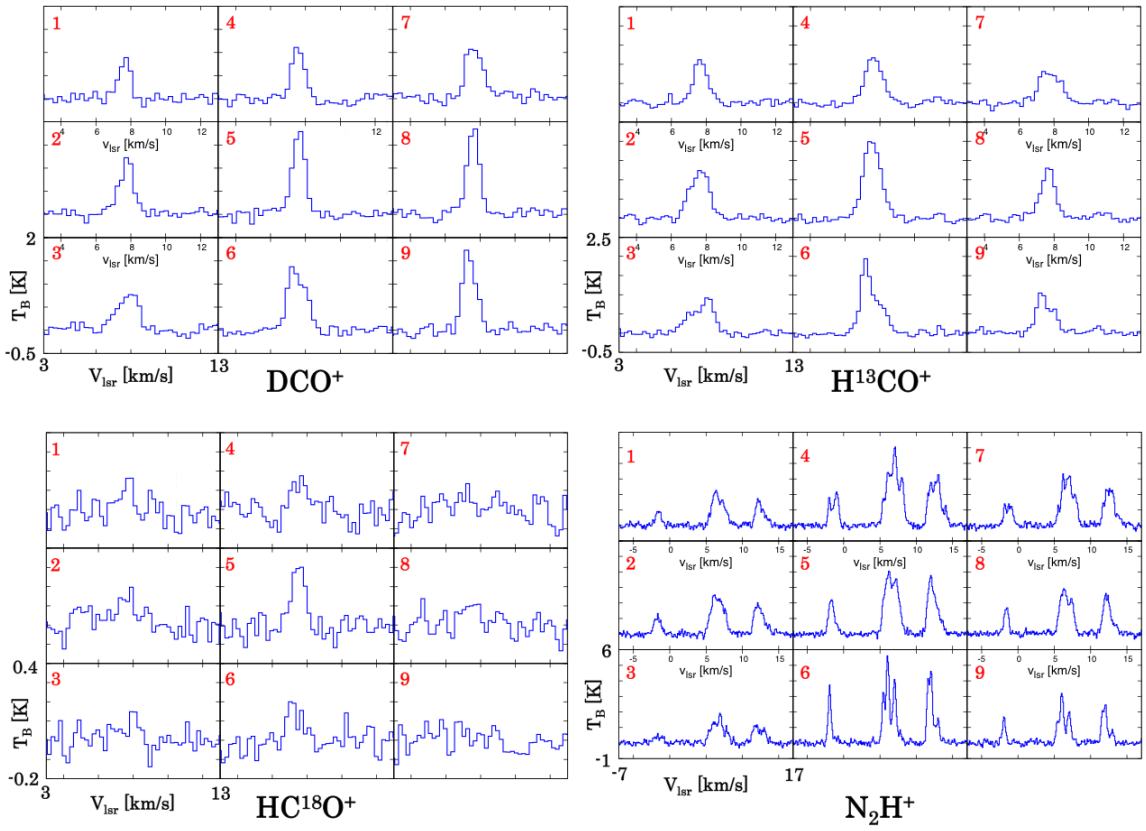

Figure 3.4: Spectra observed toward NGC1333-IRAS2A with the Nobeyama 45 m telescope.

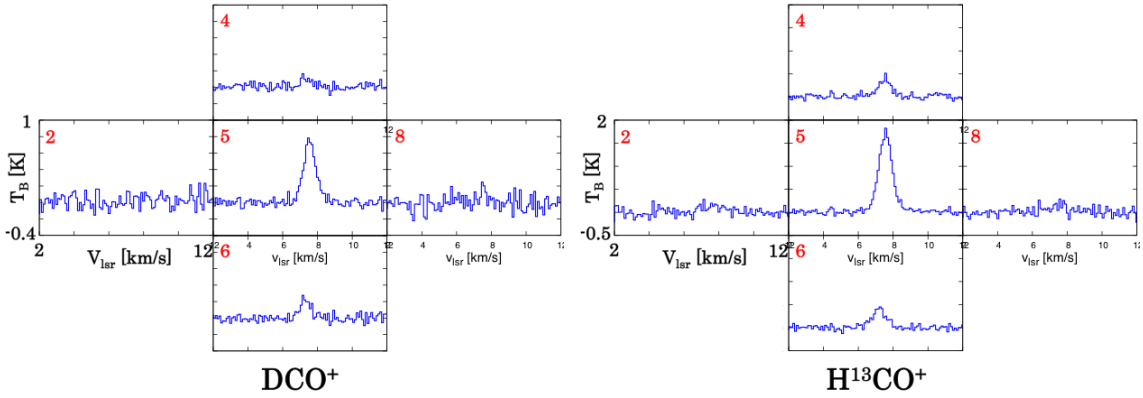

Figure 3.5: Spectra observed toward NGC1333-IRAS2A with the ASTE 10 m telescope.

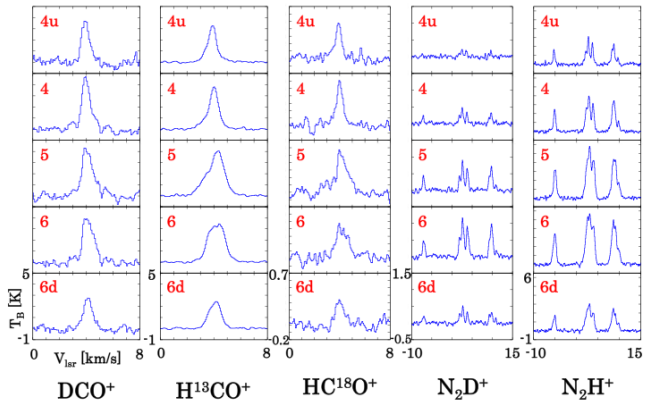

Figure 3.6: Spectra observed toward IRAS16293-2422 with the Nobeyama 45 m telescope.

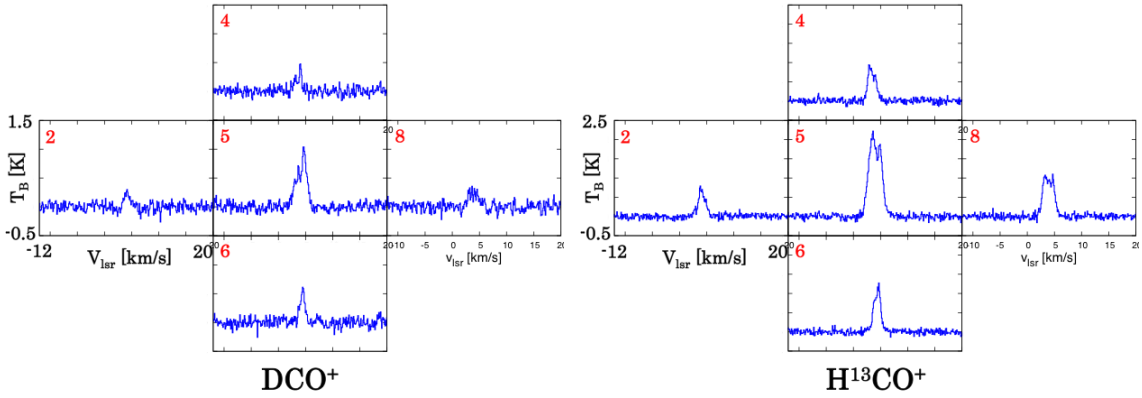

Figure 3.7: Spectra observed toward IRAS16293-2422 with the ASTE 10 m telescope.

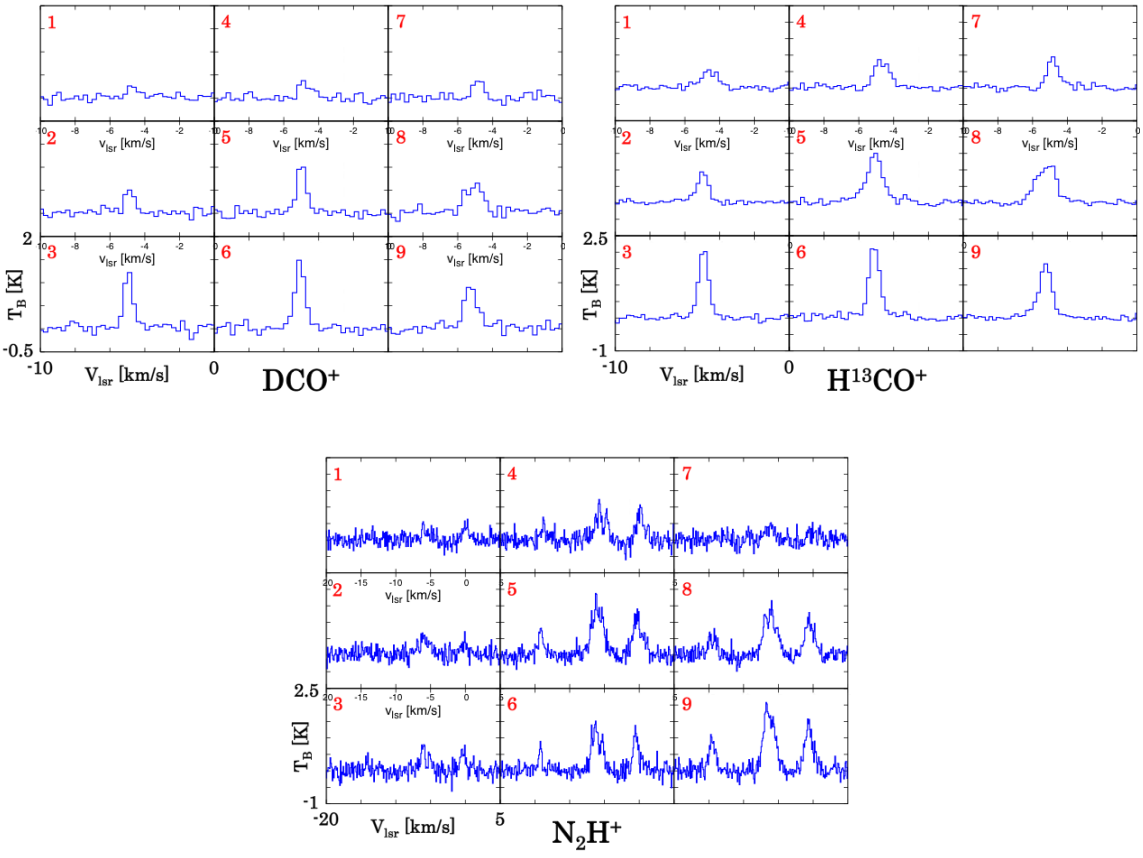

Figure 3.8: Spectra observed toward L1251A with the Nobeyama 45 m telescope.

3.2.2 Spectral line parameters

We here derive the line parameters of each molecule. For DCO^+, $H^{13}CO^+$, $HC^{18}O^+$ and H_2CO, we obtain T_B (brightness temperature), v_{lsr} (center velocity) and Δv (line width) by Gaussian fitting as:

$$y = T_B \exp\left[-\frac{4\ln 2(x - v_{lsr})^2}{\Delta v^2}\right]. \tag{3.1}$$

On the other hand, integrated intensities are directly calculated from the observed spectra. The error is evaluated from the rms noise in the range of $v = -20 - 0$ km/s, $10 - 30$ km/s, $v = -15 - -5$ km/s, $10 - 25$ km/s, $v = -10 - 0$ km/s, $15 - 30$ km/s for L1551-IRS5, L483, NGC1333-IRAS2A and IRAS16293-2422, and $v = -30 - -10$ km/s, $0 - 20$ km/s, $v = -25 - -15$ km/s, $0 - 15$ km/s, $v = -20 - -10$ km/s, $5 - 20$ km/s for L1251A. We employ the average value of the rms noise in the two intervals as the final rms noise.

On the other hand, N_2D^+ and N_2H^+ are split by the hyperfine structure of the N nucleus. We fit these hyperfine structure lines by using the following equation:

$$y = \sum_{i=1}^{7} T_{B_i} \tag{3.2}$$

$$= \sum_{i=1}^{7} T_0 \left[f(T_{ex}) - f(T_{bg})\right]\left[1 - e^{-\tau_i}\right] \exp\left[-\frac{4\ln 2(x_i - v_{lsr_i})^2}{\Delta v_i^2}\right]. \tag{3.3}$$

By use of this equation, we derive τ (optical depth), v_{lsr} and Δv by least-square fitting. Here, T_{ex} denotes excitation temperature, and T_{bg} the cosmic microwave background radiation temperature (2.7 K).

The results are summarized in tables 3.7, 3.8, 3.9, 3.11, 3.12, 3.13, 3.14, 3.15, 3.16 and 3.17. For the result of N_2D^+ and N_2H^+, we show the value obtained by assuming the excitation temperature of T_{ex} = 10 K, 20 K and 30 K (figure 3.9). Errors quoted are all three times the standard deviation (3 σ).

3.2.3 Optical depth and column density

We evaluate the optical depth (τ) and the column density (N) from the line parameter derived above by assuming the local thermodynamics equilibrium (LTE) conditions. For DCO^+,

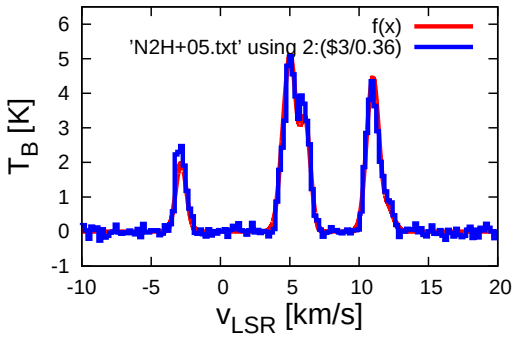

Figure 3.9: The fitting result of N_2H^+ at position 5 toward L1551-IRS5 assuming T_{ex} = 20 K.

$H^{13}CO^+$ and $HC^{18}O^+$, we use the following equation (Appendix B):

$$\tau = -\ln\left[1 - \frac{W}{\Delta v(T - T_b)}\right]. \tag{3.4}$$

Considering the effect of the optical depth, we calculate the column density by the following equation:

$$N = \frac{3h\Delta vZ}{8\pi^3\mu_0^2 S_{ul}}\left[\exp\left(\frac{h\nu}{kT}\right) - 1\right]^{-1} \exp\left(\frac{E_u}{kT}\right)\tau \tag{3.5}$$

where, k denotes the Boltzmann constant, h the Planck constant, U the partition function, S the intensity factor, μ the permanent dipole moment, ν_c the center frequency, E_u the the upper state energy and W the integrated intensity.

The column densities of N_2D^+ and N_2H^+ are calculated from the optical depth and the line width as:

$$N = \frac{3\tau\Delta v k T_{ex} e^{\frac{E_u}{kT_{ex}}}}{8\pi^3 S\mu^2 B\left(e^{\frac{h\nu_c}{kT_{ex}}} - 1\right)}. \tag{3.6}$$

Here, c denotes the speed of light in vacuum, Δv the line width and B the rotational constant. In this calculation, the excitation temperature has to be fixed to 10 K, 20 K and 30 K. The excitation temperature of 10 K is based on the gas kinetic temperature of dense cores (Benson and Myers 1989). Considering the temperature rise around the protostar, the higher

temperatures, 20 K and 30 K, are also used in order to examine the effect of the assumed excitation temperature on the derived column densities. The results are also shown in tables 3.7, 3.8, 3.10, 3.11, 3.12, 3.13, 3.14, 3.15, 3.16 and 3.17. In order to verify the assumption made for the excitation temperature, we calculated the excitation temperature using the integrated intensities at the protostar position obtained with the Nobeyama 45 m telescope and the ASTE 10 m telescope. We fitted the result of the two exicitation lines with the following equation:

$$\ln\frac{3kW}{8\pi^3\mu_0^2 S\nu} = \ln\frac{N}{Z} - \frac{E_\mathrm{u}}{kT}, \tag{3.7}$$

and calculated the excitation temperature from inclination. Here, W denotes the integrated intensity, N the column density, Z the distribution function, and E_u the upper state energy. Table 3.6 shows the result. The excitation temperatures obtained in this analysis are close to 10 K, and hence, the assumption for the excitation temperatures seem reasonable.

The optical depth of the observed lines tends to be higher for the excitation temperature of 10 K. However, it is mostly lower than unity. The exceptions are DCO^+ at position 1 toward L1551-IRS5 and that at position 4 toward IRAS16293-2422: the value is 1.1(2) and 1.3(3) respectively. The highest one for others is 0.97(9) for DCO^+ toward L483. Since the optical depth effect is taken into account by using equation (3.5), the moderate optical depth would not make serious errors in derivation of the column density.

	L483	NGC1333-IRAS2A	IRAS16293-2422
DCO^+	7.2(2)	11.7(4)	11.9(4)
$H^{13}CO^+$	8.9(3)	11.8(3)	13.14(15)

Table 3.6: The estimated excitation temperatures. The numbers in parentheses represent three times the standard deviation (3σ) in units of the best significant digits.

3.2.4 Deuterium fractionation ratio

We calculate the deuterium fractionation ratio of each molecule from the derived column densities. The results are shown in table 3.18. Here, we use the isotopic ratios $^{12}C/^{13}C = 59$ and $^{16}O/^{18}O = 672$ to calculate DCO^+/HCO^+ ratio (Lucas et al. 1998).

	position	$T_{\rm B}$ [K]	$v_{\rm lsr}$ [km/s]	Δv [km/s]	$\int Tdv$ [K•km/s]
DCO^+	1	4.60(14)	6.581(11)	0.75(3)	3.5(4)
	2	3.32(11)	6.522(12)	0.76(3)	2.6(4)
	3	2.61(13)	6.564(18)	0.72(4)	2.1(4)
	4	3.00(10)	6.523(14)	0.87(3)	2.8(4)
	5	2.49(10)	6.430(19)	0.93(5)	2.5(4)
	6	2.99(9)	6.421(14)	0.91(3)	2.9(3)
	7	3.05(13)	6.491(17)	0.82(4)	2.6(4)
	8	3.06(15)	6.38(2)	0.82(5)	2.7(4)
	9	3.48(16)	6.286(19)	0.81(4)	3.1(4)
$H^{13}CO^+$	1	2.70(6)	6.508(9)	0.83(2)	2.4(2)
	2	2.77(7)	6.443(9)	0.78(2)	2.38(19)
	3	2.26(5)	6.478(9)	0.78(2)	1.88(18)
	4	3.66(7)	6.464(7)	0.796(16)	3.12(12)
	5	3.48(6)	6.339(7)	0.813(16)	3.12(10)
	6	2.48(5)	6.363(8)	0.88(2)	2.34(12)
	7	2.00(8)	6.490(15)	0.79(4)	1.7(2)
	8	2.32(9)	6.394(15)	0.77(4)	2.0(2)
	9	2.00(9)	6.302(17)	0.76(4)	1.7(2)

	position	τ (10 K)	τ (20 K)	τ (30 K)	$N/10^{12}$ [cm^{-2}] (10 K)	$N/10^{12}$ [cm^{-2}] (20 K)	$N/10^{12}$ [cm^{-2}] (30 K)
DCO^+	1	1.1(2)	0.32(4)	0.19(3)	8.2(17)	9.2(13)	12.0(16)
	2	0.64(13)	0.22(4)	0.14(2)	5.1(11)	6.5(11)	8.7(14)
	3	0.51(13)	0.18(4)	0.11(2)	3.8(10)	5.1(11)	6.9(15)
	4	0.59(11)	0.21(3)	0.127(18)	5.4(10)	7.0(11)	9.3(14)
	5	0.46(9)	0.17(3)	0.103(17)	4.4(9)	6.0(11)	8.1(14)
	6	0.57(9)	0.20(3)	0.123(16)	5.4(9)	7.0(10)	9.4(13)
	7	0.56(12)	0.20(4)	0.12(2)	4.7(11)	6.2(12)	8.3(15)
	8	0.59(13)	0.21(4)	0.13(2)	5.0(11)	6.6(12)	8.7(16)
	9	0.72(15)	0.24(4)	0.15(2)	6.1(13)	7.6(13)	10.1(17)
$H^{13}CO^+$	1	0.51(6)	0.185(18)	0.113(11)	3.1(4)	4.1(4)	5.5(5)
	2	0.54(6)	0.195(18)	0.119(11)	3.1(4)	4.1(4)	5.4(5)
	3	0.40(5)	0.150(16)	0.092(10)	2.3(3)	3.2(3)	4.2(5)
	4	0.77(5)	0.256(13)	0.155(7)	4.5(3)	5.5(3)	7.2(4)
	5	0.74(4)	0.250(11)	0.151(6)	4.5(3)	5.5(3)	7.2(3)
	6	0.46(3)	0.168(10)	0.103(6)	3.0(2)	4.0(3)	5.3(3)
	7	0.35(5)	0.133(18)	0.082(11)	2.0(3)	2.8(4)	3.8(5)
	8	0.45(7)	0.17(2)	0.101(12)	2.6(4)	3.4(5)	4.6(6)
	9	0.37(6)	0.14(2)	0.087(12)	2.1(3)	2.9(4)	3.8(6)

Table 3.7: Line parameters toward L1551-IRS5 observed with the Nobeyama 45 m telescope. The numbers in parentheses represent three times the standard deviation (3σ) in units of the best significant digits.

	position	T_{ex} [K]	τ	v_{lsr} [km/s]	Δv [km/s]	$N/10^{11}$ [cm^{-2}]
	2	10	0.019(4)	5.35(10)	1.0(2)	3.7(15)
	4	10	0.0178(12)	5.19(3)	0.80(6)	2.9(4)
N_2D^+	5	10	0.0155(15)	4.92(4)	0.86(8)	2.7(5)
	6	10	0.0220(15)	4.89(3)	0.91(6)	4.0(6)
	8	10	0.075(5)	4.83(2)	0.53(4)	8.0(11)
	1	10	0.66(3)	5.253(10)	0.69(2)	39(3)
	2	10	0.57(2)	5.160(10)	0.64(2)	31(2)
	3	10	0.357(15)	5.273(14)	0.75(3)	23.2(19)
	4	10	0.71(3)	5.264(12)	0.86(3)	53(4)
N_2H^+	5	10	0.85(3)	5.125(11)	0.90(3)	66(4)
	6	10	0.67(3)	5.141(11)	0.75(2)	44(3)
	7	10	1.10(7)	5.145(15)	0.69(3)	65(7)
	8	10	0.90(5)	5.073(16)	0.86(4)	67(6)
	9	10	0.84(4)	5.004(10)	0.55(2)	40(3)
	2	20	0.0077(15)	5.35(10)	1.00(2)	6(2)
	4	20	0.0073(5)	5.19(3)	0.80(6)	4.3(6)
N_2D^+	5	20	0.0064(6)	4.92(4)	0.86(8)	4.0(8)
	6	20	0.0090(6)	4.89(3)	0.91(6)	6.0(8)
	8	20	0.030(2)	4.834(18)	0.53(4)	12.0(16)
	1	20	0.234(7)	5.249(10)	0.69(2)	50(3)
	2	20	0.207(7)	5.157(10)	0.64(2)	41(3)
	3	20	0.136(5)	5.270(14)	0.75(3)	32(3)
	4	20	0.252(8)	5.258(12)	0.85(3)	66(4)
N_2H^+	5	20	0.292(8)	5.119(11)	0.90(2)	81(5)
	6	20	0.238(8)	5.136(11)	0.75(2)	55(4)
	7	20	0.360(17)	5.138(14)	0.68(3)	75(7)
	8	20	0.306(13)	5.064(16)	0.85(4)	81(7)
	9	20	0.288(11)	5.001(10)	0.55(2)	49(4)
	2	30	0.0048(9)	5.35(10)	1.00(2)	8(3)
	4	30	0.0046(3)	5.19(3)	0.80(6)	5.9(8)
N_2D^+	5	30	0.0040(4)	4.92(4)	0.86(8)	5.5(11)
	6	30	0.0057(4)	4.89(3)	0.91(6)	8.3(12)
	8	30	0.0189(13)	4.835(18)	0.53(4)	16(2)
	1	30	0.142(4)	5.248(10)	0.69(2)	66(4)
	2	30	0.126(4)	5.156(10)	0.64(2)	54(3)
	3	30	0.083(3)	5.269(14)	0.75(3)	42(3)
	4	30	0.153(5)	5.257(12)	0.85(3)	87(5)
N_2H^+	5	30	0.176(5)	5.118(11)	0.90(2)	106(6)
	6	30	0.144(4)	5.135(11)	0.75(2)	73(5)
	7	30	0.214(10)	5.137(15)	0.68(3)	97(9)
	8	30	0.184(8)	5.063(16)	0.85(4)	105(9)
	9	30	0.173(6)	5.001(10)	0.55(2)	64(5)

Table 3.8: Line parameters toward L1551-IRS5 observed with the Nobeyama 45 m telescope. The numbers in parentheses represent three times the standard deviation (3σ) in units of the best significant digits.

	position	$T_{\rm B}$ [K]	$v_{\rm lsr}$ [km/s]	Δv [km/s]	$\int Tdv$ [K•km/s]
DCO^+	1	1.54(6)	5.447(15)	0.78(4)	1.28(16)
	2	1.96(7)	5.395(12)	0.66(3)	1.38(16)
	3	1.32(7)	5.370(19)	0.69(4)	1.03(16)
	4	3.10(7)	5.391(8)	0.702(19)	2.36(15)
	5	3.93(7)	5.344(6)	0.685(14)	2.86(14)
	6	2.93(6)	5.363(6)	0.685(15)	2.12(17)
	7	3.09(7)	5.352(7)	0.681(18)	2.22(16)
	8	4.27(7)	5.329(6)	0.678(14)	3.07(17)
	9	4.01(7)	5.343(6)	0.694(14)	2.94(15)
$H^{13}CO^+$	1	1.14(3)	5.407(10)	0.83(2)	1.01(8)
	2	1.43(3)	5.321(7)	0.767(18)	1.20(7)
	3	1.09(3)	5.372(10)	0.72(2)	0.90(8)
	4	1.81(4)	5.352(8)	0.703(19)	1.44(7)
	5	2.99(4)	5.289(5)	0.685(11)	2.34(7)
	6	1.86(3)	5.290(5)	0.659(12)	1.35(8)
	7	1.84(3)	5.290(5)	0.574(12)	1.10(8)
	8	2.78(4)	5.280(4)	0.569(8)	1.75(7)
	9	2.31(3)	5.299(4)	0.604(8)	1.48(8)
$HC^{18}O^+$	1	0.21(2)	5.37(3)	0.54(6)	0.05(2)
	2	0.27(2)	5.36(2)	0.55(5)	0.07(2)
	3	0.14(2)	5.30(4)	0.52(10)	0.03(2)
	4	0.42(2)	5.324(12)	0.44(3)	0.08(2)
	5	0.74(3)	5.280(9)	0.49(2)	0.174(18)
	6	0.50(3)	5.297(14)	0.45(3)	0.10(2)
	7	0.37(3)	5.274(18)	0.47(4)	0.08(2)
	8	0.64(2)	5.276(8)	0.49(2)	0.16(2)
	9	0.56(3)	5.296(12)	0.51(3)	0.14(2)

Table 3.9: Line parameters toward L483 observed with the Nobeyama 45 m telescope. The numbers in parentheses represent three times the standard deviation (3σ) in units of the best significant digits.

	position	τ (10 K)	τ (20 K)	τ (30 K)	$N/10^{12}$ [cm^{-2}] (10 K)	$N/10^{12}$ [cm^{-2}] (20 K)	$N/10^{12}$ [cm^{-2}] (30 K)
DCO^+	1	0.25(4)	0.099(14)	0.062(9)	2.1(3)	3.0(4)	4.0(6)
	2	0.34(5)	0.130(18)	0.080(11)	2.3(4)	3.3(5)	4.4(6)
	3	0.23(4)	0.091(16)	0.057(10)	1.7(3)	2.4(4)	3.3(6)
	4	0.62(6)	0.217(17)	0.132(10)	4.5(4)	5.8(5)	7.8(6)
	5	0.85(7)	0.276(16)	0.166(9)	6.1(5)	7.3(5)	9.5(6)
	6	0.55(6)	0.197(18)	0.120(11)	3.9(4)	5.2(5)	6.9(6)
	7	0.59(6)	0.208(18)	0.127(10)	4.2(5)	5.4(5)	7.3(6)
	8	0.97(9)	0.30(2)	0.181(11)	6.8(7)	7.9(6)	11.0(7)
	9	0.87(8)	0.281(18)	0.169(10)	6.3(6)	7.5(5)	9.8(6)
$H^{13}CO^+$	1	0.184(17)	0.073(6)	0.046(4)	1.13(11)	1.64(15)	2.2(2)
	2	0.242(16)	0.095(6)	0.059(4)	1.38(10)	1.96(13)	2.66(17)
	3	0.188(19)	0.075(7)	0.047(4)	1.01(10)	1.46(14)	1.98(19)
	4	0.33(2)	0.126(8)	0.078(5)	1.72(13)	2.39(16)	3.2(2)
	5	0.63(3)	0.220(8)	0.134(5)	3.22(16)	4.06(17)	5.4(2)
	6	0.33(2)	0.126(8)	0.078(5)	1.62(12)	2.24(15)	3.02(19)
	7	0.31(3)	0.117(10)	0.073(6)	1.30(12)	1.82(15)	2.5(2)
	8	0.55(3)	0.196(10)	0.120(6)	2.31(14)	3.00(15)	4.0(2)
	9	0.41(3)	0.153(9)	0.094(5)	1.84(13)	2.49(15)	3.3(2)
$HC^{18}O^+$	1	0.013(6)	0.005(3)	0.0034(16)	0.06(3)	0.09(4)	0.13(6)
	2	0.017(5)	0.007(2)	0.0046(14)	0.08(3)	0.13(4)	0.17(5)
	3	0.009(6)	0.004(2)	0.0024(15)	0.04(3)	0.06(4)	0.08(6)
	4	0.026(7)	0.011(3)	0.0070(19)	0.10(3)	0.15(4)	0.21(6)
	5	0.050(6)	0.021(2)	0.0132(15)	0.21(3)	0.32(4)	0.44(5)
	6	0.031(7)	0.013(3)	0.0082(17)	0.12(3)	0.18(4)	0.25(6)
	7	0.024(7)	0.010(3)	0.0064(17)	0.10(3)	0.15(4)	0.20(6)
	8	0.045(7)	0.019(3)	0.0117(17)	0.19(3)	0.28(4)	0.39(6)
	9	0.039(6)	0.016(3)	0.0102(16)	0.17(3)	0.25(4)	0.35(6)

Table 3.10: Line parameters toward L483 observed with the Nobeyama 45 m telescope. The numbers in parentheses represent three times the standard deviation (3σ) in units of the best significant digits.

	position	T_{ex} [K]	τ	v_{lsr} [km/s]	Δv [km/s]	$N/10^{12}$ [cm^{-2}]
	1	10	0.77(3)	4.373(14)	0.84(3)	5.6(4)
	2	10	0.65(2)	4.292(11)	0.79(3)	4.5(3)
	3	10	0.25(1)	4.229(16)	0.87(4)	1.89(16)
	4	10	1.14(6)	4.178(10)	0.53(2)	5.2(5)
N_2H^+	5	10	1.57(9)	4.155(8)	0.473(16)	6.4(6)
	6	10	0.68(3)	4.123(7)	0.466(15)	2.71(19)
	7	10	1.00(4)	4.117(6)	0.406(12)	3.5(3)
	8	10	2.39(12)	4.122(5)	0.371(9)	7.6(6)
	9	10	1.08(5)	4.126(6)	0.420(13)	3.9(3)
	1	20	0.259(10)	4.371(15)	0.87(3)	6.9(5)
	2	20	0.228(8)	4.289(12)	0.80(3)	5.7(4)
	3	20	0.098(4)	4.228(16)	0.87(4)	2.6(2)
	4	20	0.336(15)	4.179(12)	0.57(2)	5.9(5)
N_2H^+	5	20	0.423(18)	4.155(9)	0.507(19)	6.6(5)
	6	20	0.232(8)	4.121(8)	0.477(16)	3.4(2)
	7	20	0.317(11)	4.118(7)	0.417(14)	4.1(3)
	8	20	0.55(2)	4.125(6)	0.385(12)	6.5(4)
	9	20	0.333(12)	4.125(7)	0.433(15)	4.5(3)
	1	30	0.155(6)	4.370(15)	0.87(3)	9.1(7)
	2	30	0.138(4)	4.288(12)	0.81(3)	7.5(5)
	3	30	0.060(2)	4.228(16)	0.87(4)	3.5(3)
	4	30	0.197(9)	4.179(12)	0.58(3)	7.7(7)
N_2H^+	5	30	0.245(10)	4.154(10)	0.52(2)	8.5(7)
	6	30	0.140(5)	4.121(8)	0.480(17)	4.5(3)
	7	30	0.188(6)	4.118(7)	0.420(14)	5.3(4)
	8	30	0.312(11)	4.126(6)	0.390(13)	8.2(6)
	9	30	0.197(7)	4.125(7)	0.436(15)	5.8(4)

Table 3.11: Line parameters toward L483 observed with the Nobeyama 45 m telescope. The numbers in parentheses represent three times the standard deviation (3σ) in units of the best significant digits.

	position	$T_{\rm B}$ [K]	$v_{\rm lsr}$ [km/s]	Δv [km/s]	$\int T dv$ [K•km/s]
DCO^+	1	0.89(7)	7.65(3)	0.76(7)	0.7(2)
	2	1.16(6)	7.76(2)	0.98(6)	1.3(2)
	3	0.79(5)	7.84(5)	1.41(11)	1.16(19)
	4	1.14(6)	7.57(2)	0.85(6)	1.0(2)
	5	1.83(6)	7.621(14)	0.86(3)	1.70(18)
	6	1.31(6)	7.49(3)	1.25(7)	1.7(2)
	7	1.14(7)	7.66(3)	1.14(8)	1.4(2)
	8	1.89(6)	7.607(13)	0.83(3)	1.7(2)
	9	1.69(8)	7.37(2)	0.91(5)	1.6(2)
$H^{13}CO^+$	1	1.12(5)	7.67(2)	0.94(5)	1.09(17)
	2	1.25(4)	7.63(2)	1.28(5)	1.66(15)
	3	0.79(5)	7.81(5)	1.61(11)	1.32(15)
	4	1.19(4)	7.644(19)	1.15(5)	1.45(17)
	5	2.04(4)	7.550(12)	1.17(3)	2.56(17)
	6	1.60(9)	7.35(3)	1.18(8)	2.08(16)
	7	0.82(4)	7.76(4)	1.43(9)	1.23(16)
	8	1.29(5)	7.661(18)	0.95(4)	1.36(15)
	9	0.93(5)	7.44(3)	1.17(8)	1.18(16)

	position	τ (10 K)	τ (20 K)	τ (30 K)	$N/10^{12}$ [cm^{-2}] (10 K)	$N/10^{12}$ [cm^{-2}] (20 K)	$N/10^{12}$ [cm^{-2}] (30 K)
DCO^+	1	0.13(5)	0.052(18)	0.033(11)	1.0(4)	1.5(5)	2.1(7)
	2	0.19(4)	0.077(14)	0.048(9)	2.0(4)	2.9(6)	3.9(7)
	3	0.12(2)	0.049(9)	0.031(6)	1.8(4)	2.6(5)	3.6(7)
	4	0.18(4)	0.070(16)	0.044(10)	1.6(4)	2.3(5)	3.1(7)
	5	0.32(4)	0.122(14)	0.075(9)	2.8(4)	4.0(5)	5.4(7)
	6	0.21(3)	0.082(11)	0.051(7)	2.7(4)	3.9(6)	5.4(8)
	7	0.18(3)	0.071(13)	0.044(8)	2.1(4)	3.1(6)	4.2(8)
	8	0.33(5)	0.127(16)	0.079(10)	2.9(4)	4.0(5)	5.5(7)
	9	0.27(4)	0.107(15)	0.066(9)	2.6(4)	3.7(6)	5.1(8)
$H^{13}CO^+$	1	0.17(3)	0.070(12)	0.044(7)	1.2(2)	1.8(3)	2.4(4)
	2	0.20(2)	0.078(8)	0.049(5)	1.9(2)	2.7(3)	3.7(4)
	3	0.12(2)	0.049(7)	0.031(4)	1.4(2)	2.1(3)	2.9(4)
	4	0.19(3)	0.076(10)	0.047(6)	1.6(2)	2.3(3)	3.2(4)
	5	0.36(3)	0.135(10)	0.083(6)	3.1(3)	4.3(3)	5.7(4)
	6	0.28(3)	0.107(11)	0.067(7)	2.4(3)	3.4(4)	4.6(6)
	7	0.13(2)	0.051(8)	0.032(5)	1.3(2)	2.0(3)	2.7(4)
	8	0.22(3)	0.087(11)	0.054(6)	1.5(2)	2.2(3)	3.0(4)
	9	0.15(2)	0.060(10)	0.038(6)	1.3(2)	1.9(3)	2.6(4)

Table 3.12: Line parameters toward NGC1333-IRAS2A observed with the Nobeyama 45 m telescope. The numbers in parentheses represent three times the standard deviation (3σ) in units of the best significant digits.

	position	T_{ex} [K]	τ	v_{lsr} [km/s]	Δv [km/s]	$N/10^{12}$ [cm^{-2}]
	1	10	0.274(9)	6.426(13)	1.01(3)	2.39(15)
	2	10	0.308(9)	6.335(13)	1.20(4)	3.18(18)
	3	10	0.139(6)	6.38(3)	1.65(8)	1.98(19)
	4	10	0.455(17)	6.69(2)	1.66(6)	6.5(5)
N_2H^+	5	10	0.618(18)	6.290(11)	1.09(3)	5.8(3)
	6	10	1.40(4)	6.043(5)	0.496(10)	6.0(3)
	7	10	0.372(12)	6.658(16)	1.33(4)	4.3(3)
	8	10	0.463(12)	6.365(9)	0.88(2)	3.50(17)
	9	10	0.544(15)	6.049(6)	0.544(13)	2.54(13)
	1	20	0.106(3)	6.424(13)	1.01(3)	3.3(2)
	2	20	0.117(3)	6.334(13)	1.21(4)	4.4(3)
	3	20	0.055(2)	6.38(3)	1.66(8)	2.8(3)
	4	20	0.168(6)	6.69(2)	1.66(6)	8.6(6)
N_2H^+	5	20	0.217(6)	6.288(12)	1.11(3)	7.4(4)
	6	20	0.416(10)	6.039(5)	0.504(11)	6.5(3)
	7	20	0.140(4)	6.657(16)	1.33(4)	5.8(4)
	8	20	0.171(4)	6.361(9)	0.88(2)	4.7(2)
	9	20	0.198(5)	6.047(6)	0.545(13)	3.33(16)
	1	30	0.0665(19)	6.423(13)	1.01(3)	4.5(3)
	2	30	0.0724(19)	6.333(13)	1.21(4)	5.9(3)
	3	30	0.0343(15)	6.38(3)	1.66(8)	3.8(4)
	4	30	0.103(3)	6.69(2)	1.67(6)	11.5(8)
N_2H^+	5	30	0.132(4)	6.288(12)	1.11(3)	9.8(5)
	6	30	0.244(6)	6.038(6)	0.508(12)	8.3(4)
	7	30	0.086(3)	6.657(16)	1.33(4)	7.7(5)
	8	30	0.104(2)	6.360(9)	0.89(2)	6.2(3)
	9	30	0.120(3)	6.046(6)	0.546(13)	4.4(2)

Table 3.13: Line parameters toward NGC1333-IRAS2A observed with the Nobeyama 45 m telescope. The numbers in parentheses represent three times the standard deviation (3σ) in units of the best significant digits.

	position	$T_{\rm B}$ [K]	$v_{\rm lsr}$ [km/s]	Δv [km/s]	$\int Tdv$ [K•km/s]
DCO^+	4u	3.70(15)	3.926(14)	0.69(3)	2.6(6)
	4	4.51(14)	3.972(11)	0.75(3)	3.9(5)
	5	4.06(13)	4.072(16)	0.99(4)	4.4(5)
	6	3.94(12)	4.126(14)	0.95(3)	4.0(5)
	6d	2.73(10)	4.110(14)	0.79(3)	2.3(5)
$H^{13}CO^+$	4u	3.07(5)	3.876(6)	0.822(15)	2.93(14)
	4	3.51(6)	3.992(8)	0.913(18)	3.75(13)
	5	3.71(6)	4.176(12)	1.55(3)	6.22(13)
	6	3.55(4)	4.205(8)	1.443(18)	5.39(12)
	6d	2.41(2)	4.089(5)	1.066(12)	2.75(12)
$HC^{18}O^+$	4u	0.45(2)	3.904(14)	0.60(3)	0.31(9)
	4	0.55(2)	4.002(13)	0.65(3)	0.41(8)
	5	0.47(2)	4.18(2)	1.18(6)	0.59(8)
	6	0.398(18)	4.18(3)	1.20(6)	0.49(9)
	6d	0.32(2)	4.02(3)	0.80(6)	0.26(8)

	position	τ (10 K)	τ (20 K)	τ (30 K)	$N/10^{12}$ [cm^{-2}] (10 K)	$N/10^{12}$ [cm^{-2}] (20 K)	$N/10^{12}$ [cm^{-2}] (30 K)
DCO^+	4u	0.7(3)	0.25(7)	0.15(4)	5(2)	6.6(19)	9(2)
	4	1.3(3)	0.36(6)	0.21(3)	10(3)	10.4(16)	14(2)
	5	0.93(18)	0.29(4)	0.18(2)	9.6(19)	11.3(16)	15(2)
	6	0.86(17)	0.28(4)	0.17(2)	8.6(18)	10.2(15)	13.5(19)
	6d	0.52(15)	0.19(5)	0.11(3)	4.2(13)	5.6(14)	7.5(19)
$H^{13}CO^+$	4u	0.67(5)	0.231(13)	0.140(8)	4.1(3)	5.1(3)	6.7(4)
	4	0.83(5)	0.271(13)	0.163(7)	5.6(4)	6.7(3)	8.7(4)
	5	0.80(3)	0.265(8)	0.160(5)	9.2(4)	11.0(4)	14.4(5)
	6	0.72(3)	0.243(7)	0.147(4)	7.7(3)	9.4(3)	12.4(4)
	6d	0.44(2)	0.162(8)	0.099(5)	3.46(19)	4.6(2)	6.2(3)
$HC^{18}O^+$	4u	0.07(2)	0.031(9)	0.019(6)	0.38(12)	0.58(17)	0.8(2)
	4	0.09(2)	0.037(8)	0.023(5)	0.51(11)	0.76(16)	1.0(2)
	5	0.071(11)	0.029(4)	0.019(3)	0.72(11)	1.08(17)	1.5(2)
	6	0.057(12)	0.024(5)	0.015(3)	0.59(13)	0.89(19)	1.2(3)
	6d	0.046(15)	0.019(6)	0.012(4)	0.31(11)	0.47(16)	0.7(2)

Table 3.14: Line parameters toward IRAS16293-2422 observed with the Nobeyama 45 m telescope. The numbers in parentheses represent three times the standard deviation (3σ) in units of the best significant digits.

	position	T_{ex} [K]	τ	v_{lsr} [km/s]	Δv [km/s]	$N/10^{11}$ [cm^{-2}]
N_2D^+	4u	10	0.032(3)	2.456(19)	0.46(4)	3.0(5)
	4	10	0.064(3)	2.574(15)	0.60(3)	7.7(8)
	5	10	0.124(6)	2.686(16)	0.66(3)	16.5(15)
	6	10	0.157(7)	2.765(19)	0.79(4)	25(2)
	6d	10	0.072(3)	2.692(13)	0.56(3)	8.1(8)
N_2H^+	4u	10	0.509(13)	2.704(6)	0.521(12)	22.80(12)
	4	10	0.728(16)	2.823(6)	0.686(12)	42.92(19)
	5	10	0.93(2)	2.939(7)	0.984(18)	78.8(4)
	6	10	0.926(19)	2.867(7)	1.089(18)	86.6(4)
	6d	10	0.394(9)	2.815(9)	0.97(2)	32.84(17)
N_2D^+	4u	20	0.0133(11)	2.456(19)	0.46(4)	4.5(7)
	4	20	0.0262(12)	2.573(14)	0.60(3)	11.5(11)
	5	20	0.050(2)	2.685(16)	0.66(3)	24(2)
	6	20	0.063(3)	2.763(19)	0.79(4)	37(3)
	6d	20	0.0293(13)	2.692(13)	0.56(3)	12.2(11)
N_2H^+	4u	20	0.185(4)	2.703(6)	0.526(12)	30.06(15)
	4	20	0.249(5)	2.818(6)	0.699(13)	53.9(2)
	5	20	0.309(6)	2.935(8)	0.989(19)	94.7(4)
	6	20	0.306(5)	2.864(7)	1.100(19)	104.2(4)
	6d	20	0.147(3)	2.813(9)	0.97(2)	44.4(2)
N_2D^+	4u	30	0.0083(7)	2.456(19)	0.46(4)	6.2(10)
	4	30	0.0164(8)	2.573(14)	0.60(3)	15.7(15)
	5	30	0.0311(14)	2.684(16)	0.66(3)	33(3)
	6	30	0.0390(18)	2.762(19)	0.79(4)	50(5)
	6d	30	0.0183(8)	2.692(13)	0.56(3)	16.4(15)
N_2H^+	4u	30	0.113(3)	2.702(6)	0.528(12)	39.9(2)
	4	30	0.150(3)	2.817(6)	0.703(13)	70.8(3)
	5	30	0.185(4)	2.934(8)	0.992(19)	123.4(5)
	6	30	0.183(3)	2.863(7)	1.105(19)	135.9(5)
	6d	30	0.0904(19)	2.813(9)	0.98(2)	59.2(3)

Table 3.15: Line parameters toward IRAS16293-2422 observed with the Nobeyama 45 m telescope. The numbers in parentheses represent three times the standard deviation (3σ) in units of the best significant digits.

	position	$T_{\rm B}$ [K]	$v_{\rm lsr}$ [km/s]	Δv [km/s]	$\int T dv$ [K•km/s]
DCO^+	1	0.26(5)	−4.69(8)	0.78(18)	0.21(14)
	2	0.54(6)	−4.87(4)	0.64(9)	0.39(14)
	3	1.26(8)	−4.943(18)	0.60(4)	0.85(14)
	4	0.33(5)	−4.77(7)	0.89(16)	0.31(15)
	5	1.09(6)	−4.977(17)	0.63(4)	0.75(15)
	6	1.46(6)	−5.072(15)	0.69(4)	1.13(15)
	7	0.41(6)	−4.82(5)	0.68(12)	0.27(15)
	8	0.62(6)	−5.06(5)	1.22(13)	0.77(16)
	9	0.91(7)	−5.26(3)	0.91(8)	0.88(15)
$H^{13}CO^+$	1	0.50(4)	−4.59(4)	1.19(10)	0.66(15)
	2	0.91(4)	−4.974(18)	0.79(4)	0.86(14)
	3	2.10(5)	−4.917(8)	0.678(19)	1.60(16)
	4	0.83(4)	−4.68(3)	1.04(6)	0.90(15)
	5	1.42(5)	−5.08(2)	1.12(5)	1.77(16)
	6	2.19(7)	−5.111(11)	0.75(3)	1.91(15)
	7	0.91(5)	−4.83(2)	0.78(5)	0.77(15)
	8	1.13(4)	−5.21(2)	1.37(6)	1.64(13)
	9	1.61(5)	−5.259(12)	0.88(3)	1.61(17)

	position	τ (10 K)	τ (20 K)	τ (30 K)	$N/10^{12}$ [cm^{-2}] (10 K)	$N/10^{12}$ [cm^{-2}] (20 K)	$N/10^{12}$ [cm^{-2}] (30 K)
DCO^+	1	0.04(3)	0.016(11)	0.010(7)	0.3(2)	0.5(4)	0.7(5)
	2	0.09(4)	0.035(14)	0.022(9)	0.6(3)	0.9(4)	1.2(5)
	3	0.21(4)	0.085(16)	0.053(10)	1.3(3)	2.0(4)	2.7(5)
	4	0.05(3)	0.020(11)	0.013(7)	0.5(3)	0.7(4)	1.0(5)
	5	0.18(4)	0.072(16)	0.045(10)	1.2(3)	1.7(4)	2.4(5)
	6	0.25(4)	0.098(15)	0.061(9)	1.8(3)	2.6(4)	3.6(6)
	7	0.06(3)	0.023(14)	0.015(9)	0.4(3)	0.6(4)	0.8(5)
	8	0.09(2)	0.037(9)	0.023(5)	1.2(3)	1.7(4)	2.4(6)
	9	0.14(3)	0.058(11)	0.036(7)	1.3(3)	2.0(4)	2.8(6)
$H^{13}CO^+$	1	0.08(2)	0.033(8)	0.021(5)	0.70(19)	1.0(3)	1.4(4)
	2	0.16(3)	0.065(11)	0.041(7)	0.95(18)	1.4(3)	1.9(3)
	3	0.39(5)	0.146(16)	0.090(10)	2.0(3)	2.7(3)	3.6(4)
	4	0.13(2)	0.051(9)	0.032(6)	1.0(2)	1.4(3)	2.0(4)
	5	0.24(3)	0.096(10)	0.060(6)	2.0(3)	2.9(3)	3.9(4)
	6	0.43(5)	0.159(15)	0.098(9)	2.4(3)	3.2(3)	4.3(4)
	7	0.15(3)	0.059(12)	0.037(8)	0.84(19)	1.2(3)	1.7(4)
	8	0.179(18)	0.072(7)	0.045(4)	1.83(19)	2.6(3)	3.6(4)
	9	0.29(4)	0.111(13)	0.069(8)	1.9(3)	2.7(3)	3.6(4)

Table 3.16: Line parameters toward L1251A observed with the Nobeyama 45 m telescope. The numbers in parentheses represent three times the standard deviation (3σ) in units of the best significant digits.

	position	T_{ex} [K]	τ	v_{lsr} [km/s]	Δv [km/s]	$N/10^{12}$ [cm^{-2}]
	1	10	0.049(10)	−5.86(9)	0.80(17)	0.34(14)
	2	10	0.062(11)	−6.05(8)	0.94(17)	0.50(18)
	3	10	0.121(16)	−6.11(3)	0.55(7)	0.57(15)
	4	10	0.174(14)	−5.71(2)	0.59(5)	0.89(15)
N_2H^+	5	10	0.156(10)	−6.21(4)	1.31(9)	1.8(2)
	6	10	0.190(15)	−6.35(3)	0.77(5)	1.26(19)
	7	10	0.035(11)	−6.18(15)	1.1(4)	0.3(2)
	8	10	0.143(9)	−6.43(4)	1.41(10)	1.7(2)
	9	10	0.206(11)	−6.53(3)	1.19(7)	2.1(2)
	1	20	0.020(4)	−5.86(9)	0.80(17)	0.5(2)
	2	20	0.025(4)	−6.05(8)	0.93(17)	0.7(3)
	3	20	0.048(6)	−6.11(3)	0.55(7)	0.8(2)
	4	20	0.068(5)	−5.71(2)	0.60(5)	1.3(2)
N_2H^+	5	20	0.062(4)	−6.21(4)	1.31(9)	2.5(3)
	6	20	0.075(6)	−6.35(3)	0.77(5)	1.8(3)
	7	20	0.014(4)	−6.18(15)	1.1(4)	0.5(3)
	8	20	0.057(3)	−6.43(4)	1.41(10)	2.5(3)
	9	20	0.081(4)	−6.53(3)	1.19(7)	3.0(3)
	1	30	0.013(2)	−5.86(9)	0.80(17)	0.7(3)
	2	30	0.016(3)	−6.05(8)	0.93(17)	1.0(4)
	3	30	0.030(4)	−6.11(3)	0.55(7)	1.1(3)
	4	30	0.042(3)	−5.71(2)	0.60(5)	1.7(3)
N_2H^+	5	30	0.039(2)	−6.21(4)	1.31(9)	3.4(5)
	6	30	0.047(3)	−6.35(3)	0.77(5)	2.4(4)
	7	30	0.009(3)	−6.18(15)	1.1(4)	0.7(4)
	8	30	0.035(2)	−6.43(4)	1.41(10)	3.4(4)
	9	30	0.050(3)	−6.53(3)	1.19(7)	4.0(4)

Table 3.17: Line parameters toward L1251A observed with the Nobeyama 45 m telescope. The numbers in parentheses represent three times the standard deviation (3σ) in units of the best significant digits.

		10 K	20 K	30 K	literature data
DCO^+/HCO^+	1	0.044(11)	0.038(7)	0.037(6)	
	2	0.027(6)	0.027(5)	0.027(5)	
	3	0.028(8)	0.028(7)	0.028(7)	
	4	0.020(4)	0.022(3)	0.022(3)	
	5	0.017(4)	0.019(3)	0.019(3)	
	6	0.031(6)	0.030(5)	0.030(5)	
	7	0.039(11)	0.038(9)	0.037(9)	
	8	0.033(9)	0.032(7)	0.032(7)	
	9	0.050(14)	0.045(10)	0.045(10)	
N_2D^+/N_2H^+	1				
	2	0.12(5)	0.14(6)	0.14(6)	
	3				
	4	0.055(9)	0.065(10)	0.068(11)	
	5	0.041(8)	0.050(10)	0.052(11)	0.08(1)
	6	0.092(14)	0.109(17)	0.114(17)	
	7				
	8	0.12(2)	0.15(3)	0.16(3)	
	9				

L1551-IRS5

		10 K	20 K	30 K	literature data
DCO^+/HCO^+	1	0.031(6)	0.031(5)	0.031(5)	
	2	0.029(5)	0.028(4)	0.028(4)	
	3	0.028(6)	0.028(6)	0.028(6)	
	4	0.045(5)	0.041(4)	0.041(4)	
	5	0.032(3)	0.030(2)	0.030(2)	0.06
	6	0.041(6)	0.039(5)	0.039(4)	
	7	0.055(8)	0.051(6)	0.050(6)	
	8	0.050(6)	0.045(4)	0.044(4)	
	9	0.058(7)	0.051(5)	0.050(4)	

L483

		10 K	20 K	30 K	literature data
DCO^+/HCO^+	1	0.014(6)	0.015(6)	0.015(6)	
	2	0.018(4)	0.018(4)	0.018(4)	
	3	0.021(5)	0.021(5)	0.021(5)	
	4	0.016(5)	0.017(5)	0.017(5)	
	5	0.015(3)	0.016(2)	0.016(2)	0.02
	6	0.019(4)	0.020(4)	0.020(4)	
	7	0.027(7)	0.027(7)	0.027(7)	
	8	0.031(6)	0.031(6)	0.031(6)	
	9	0.034(8)	0.034(8)	0.033(8)	

NGC1333-IRAS2A

		10 K	20 K	30 K	literature data
DCO^+/HCO^+	4u	0.022(8)	0.022(6)	0.022(6)	
	4	0.030(8)	0.026(4)	0.026(4)	
	5	0.018(4)	0.017(3)	0.017(2)	0.007
	6	0.019(4)	0.018(3)	0.018(3)	
	6d	0.021(6)	0.021(5)	0.021(5)	
N_2D^+/N_2H^+	4u	0.013(2)	0.15(2)	0.16(3)	
	4	0.0180(18)	0.21(2)	0.22(2)	
	5	0.021(2)	0.26(2)	0.27(3)	
	6	0.029(3)	0.35(3)	0.37(3)	
	6d	0.025(2)	0.27(3)	0.28(3)	

IRAS16293-2422

		10 K	20 K	30 K	literature data
DCO^+/HCO^+	1	0.007(6)	0.008(6)	0.008(6)	
	2	0.010(5)	0.011(5)	0.011(5)	
	3	0.012(3)	0.012(3)	0.013(3)	
	4	0.008(5)	0.008(5)	0.008(5)	
	5	0.010(3)	0.010(3)	0.010(3)	
	6	0.013(3)	0.014(3)	0.014(3)	
	7	0.008(5)	0.008(6)	0.008(6)	
	8	0.011(3)	0.011(3)	0.011(3)	
	9	0.012(3)	0.013(3)	0.013(3)	

L1251A

Table 3.18: Deuterium fractionation ratios observed with the Nobeyama 45 m telescope. The numbers in parentheses represent three times the standard deviation (3σ) in units of the best significant digits. The literature data are taken from Roberts et al. (2007), Wootten et al. (1982) and Lis et al, (2002).

3.3 Discussion

Here, we summarize the distribution of the deuterium fractionation ratios of the ionic species in the five sources.

3.3.1 L1551-IRS5

Figure 3.10 shows the deuterium fractionation ratio of DCO^+/HCO^+ and N_2D^+/N_2H^+. We first consider the DCO^+/HCO^+ ratio. The deuterium fractionation ratio is lower toward the protostar position (position 5) than toward the other positions except for position 4. The deuterium fractionation ratio at position 4 is comparable with that at the protostar position. No strong gradient of the deuterium fractionation ratio can be found, although position 9 shows a relatively high ratio. The decrease of the deuterium fractionation toward the protostar position is not due to the optical depth effect. The optical depth of the DCO^+ line is certainly lower than or comparable to those of the other positions (figure 3.11), and hence, the saturation effect of the DCO^+ line as a cause of the decrease of the deuterium fractionation ratio toward the protostar position seems to be ruled out.

The similar trend can be seen in the N_2D^+/N_2H^+ ratio. The N_2D^+/N_2H^+ ratio also shows no apparent gradient, and the N_2D^+/N_2H^+ ratio is lower at the protostar position than at the other positions.

3.3.2 L483

Figure 3.12 shows the distribution of the DCO^+/HCO^+ ratios. The DCO^+/HCO^+ ratio at positions 1, 2, 3 is close the ratio at the protostar position. On the other hand, position 4, 6, 7, 8 and 9 show higher DCO^+/HCO^+ ratios than the ratio at the protostar position. Moreover, the DCO^+/HCO^+ ratios at the positions 1, 2 and 3 are almost the same. Similarly, the ratios at the positions 4 and 6 are similar to each other, and those at the position 7 and 9 are also similar. This means that there exists a gradient of the ratio over the cloud from east to west. Taking this gradient into account, there is a possibility that the DCO^+/HCO^+ ratio at the protostar position may slightly be declined.

To examine this trend, we plot the DCO^+/HCO^+ ratio for the following four directions passing through the protostar position: positions 1, 5, and 9, positions 2, 5 and 8, positions 3, 5 and 7, and positions 4, 5 and 6. The bottom panels of figure 3.12 show the result. When we

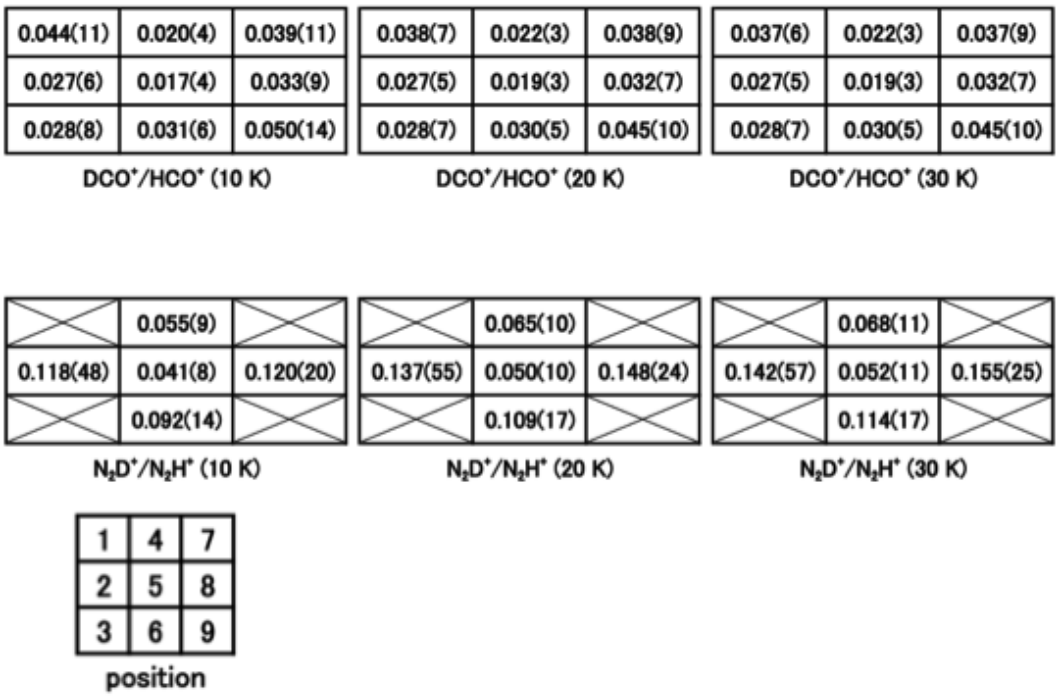

Figure 3.10: The deuterium fractionation ratio toward L1551-IRS5. The numbers in parentheses represent three times the standard deviation (3σ) in units of the best significant digits.

compare the three positions of each direction, there seems to be a slight dip of a deuterium fractionation ratio at the protostar position.

The deuterium fractionation ratio is known as the evolutionary tracer of starless cores, and deuterium fractionation ratio is higher in denser regions of starless cores. If deuterated species does not decline around the protostar, the deuterium fractionation ratio would still be enhanced at the protostar position. The dip of the DCO^+/HCO^+ ratio at the protostar position may suggest that the DCO^+/HCO^+ ratio is decreased around the protostar.

We also show the optical depths of DCO^+ and $H^{13}CO^+$ in figure 3.13. The gradient over the cloud from east to west seems to exist as in the case of the deuterium fractionation. However, the dip does not seem to originated from the high optical depth of the DCO^+ line, as in the case of L1551-IRS5 (Section 3.3.1).

3.3.3 NGC1333-IRAS2A

We show the distribution of the deuterium fractionation ratio of the DCO^+/HCO^+ in figure 3.14. The deuterium fractionation ratio seems to be affected by the gradient over the cloud as with the case of L483. Nevertheless, the DCO^+/HCO^+ ratio may be decreased slightly toward the protostar. This trend is marginally seen in the variations of the ratio along various directions through the protostar position (bottom panels of figure 3.14).

Figure 3.15 shows the optical depths of DCO^+ and $H^{13}CO^+$. The optical depths of DCO^+ at position 8 and 9 seems to be high. However, the optical depth of DCO^+ line toward the protostar position is moderate, and the possible dip of the deuterium fractionation ratio would not be due to the saturation of the DCO^+ line.

3.3.4 IRAS16293-2422

In figure 3.16, we plot the deuterium fractionation ratios DCO^+/HCO^+ and N_2D^+/N_2H^+. The meaning of the red value is similar as before. The DCO^+/HCO^+ ratio at position 4 is higher than that at the protostar position (position 5) and the N_2D^+/N_2H^+ ratio at position 6 is higher than that at the protostar position. The deuterium fractionation ratios at the other positions are comparable to that at the protostar position. The DCO^+/HCO^+ and N_2D^+/N_2H^+ ratios do not have a peak at the protostar position, although only a strip scan observation is available.

3.3.5 L1251A

Figure 3.17 shows the distribution of the DCO^+/HCO^+ toward L1251A. The meaning of the red value is described above. The deuterium fractionation ratio is slightly higher at position 6. However, the ratio seems almost constant over the cloud. This result is in contrast to those for the other sources.

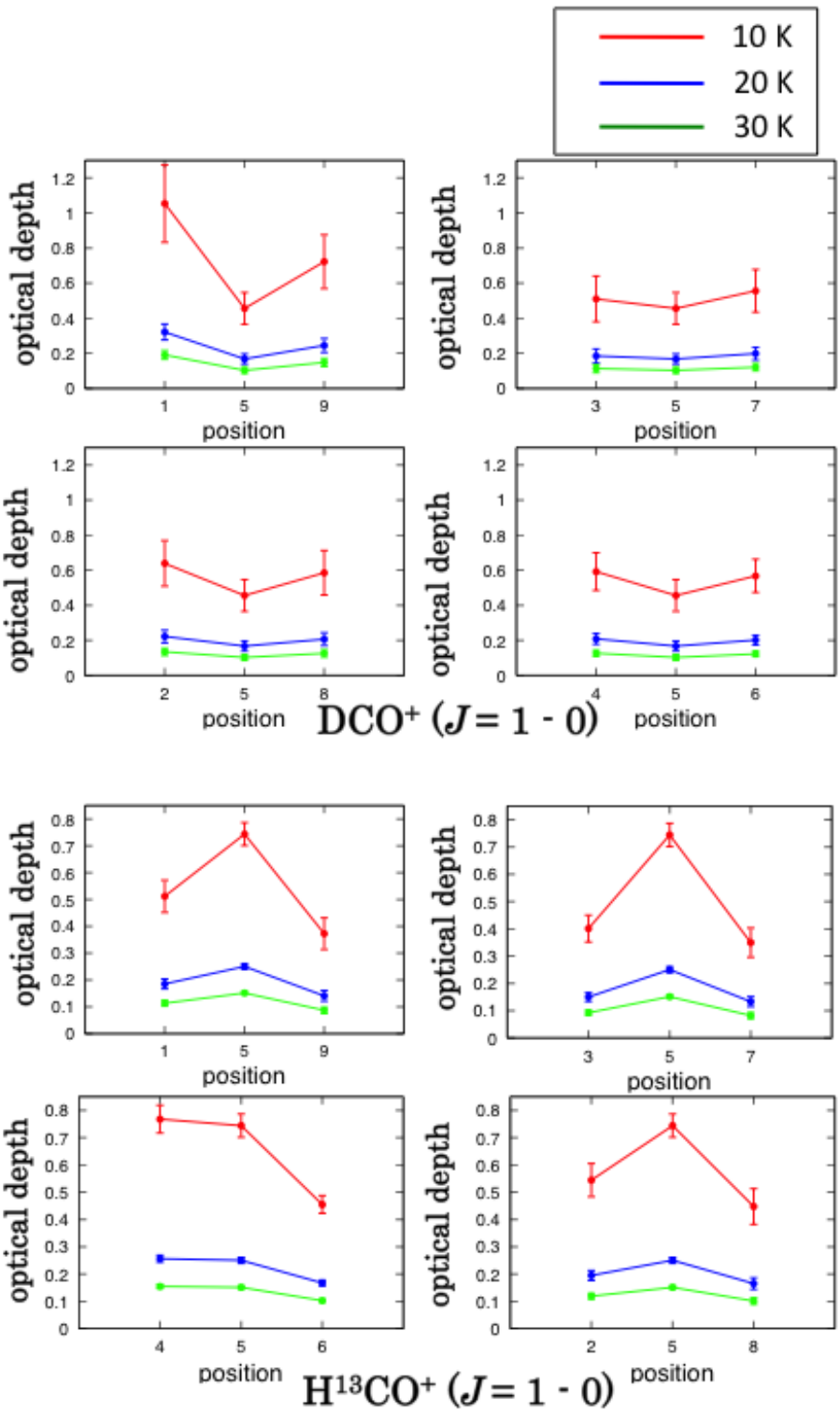

Figure 3.11: The optical depth toward L1551-IRS5. We show 3σ value for error.

0.031(6)	0.045(5)	0.055(8)
0.029(5)	0.032(3)	0.050(6)
0.028(6)	0.041(6)	0.058(7)

DCO^+/HCO^+ (10 K)

0.031(5)	0.041(4)	0.051(6)
0.028(4)	0.030(2)	0.045(4)
0.028(6)	0.039(5)	0.051(5)

DCO^+/HCO^+ (20 K)

0.031(5)	0.041(4)	0.050(6)
0.028(4)	0.030(2)	0.044(4)
0.028(6)	0.039(4)	0.050(4)

DCO^+/HCO^+ (30 K)

1	4	7
2	5	8
3	6	9

position

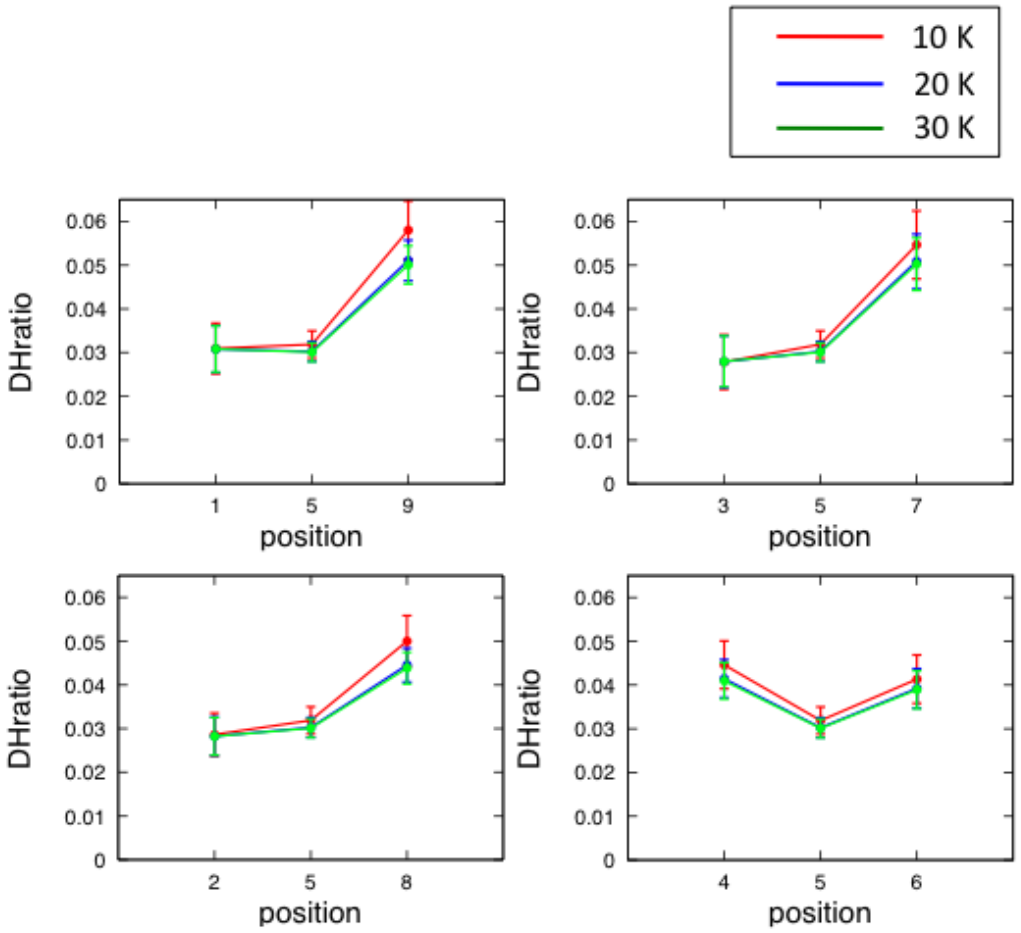

Figure 3.12: The deuterium fractionation ratio toward L483. The numbers in parentheses represent three times the standard deviation (3σ) in units of the best significant digits.

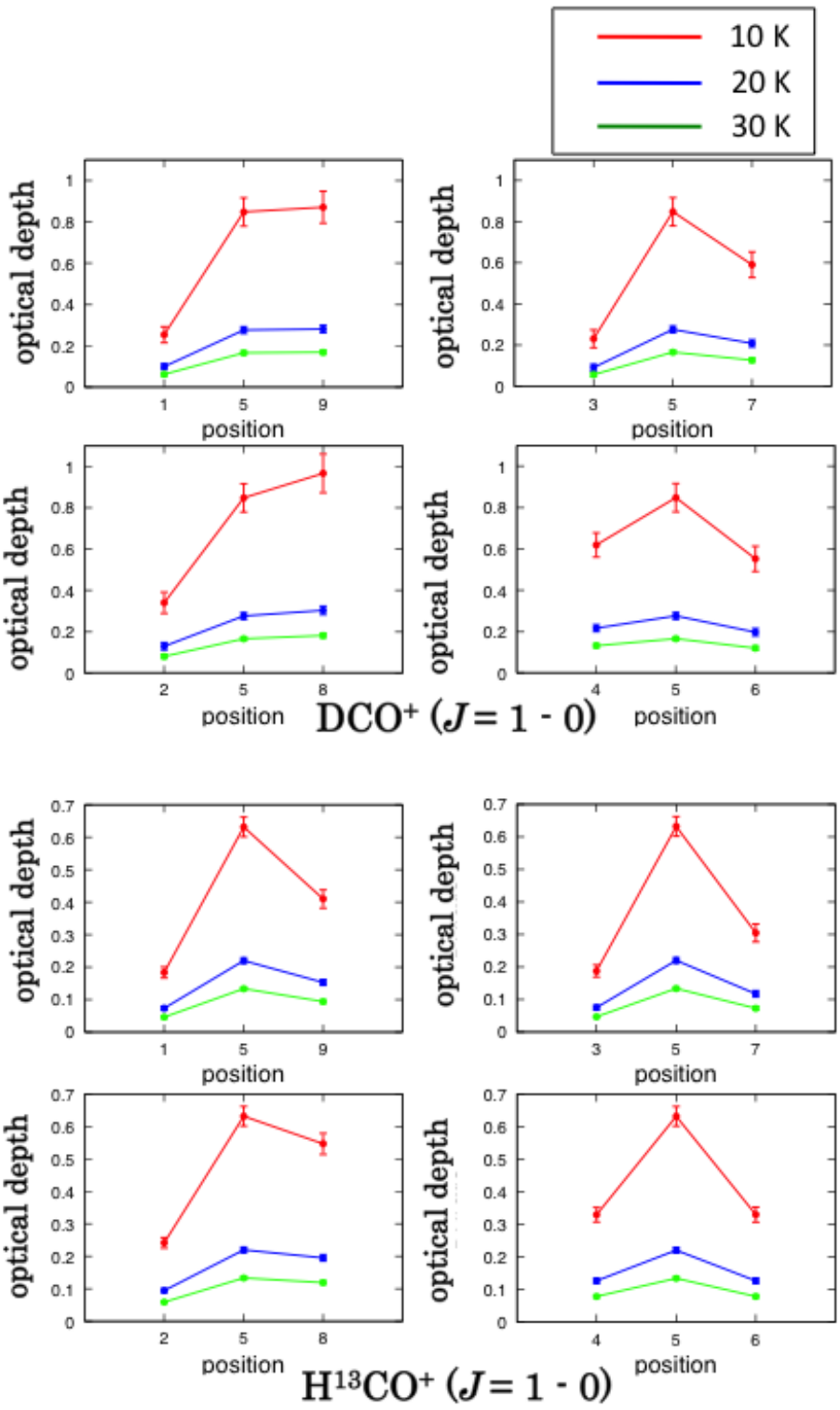

Figure 3.13: The optical depth toward L483. We show 3σ value for error.

0.014(6)	0.016(5)	0.027(7)
0.018(4)	0.015(3)	0.031(6)
0.021(5)	0.019(4)	0.034(8)

DCO^+/HCO^+ (10 K)

0.015(6)	0.017(5)	0.027(7)
0.018(4)	0.016(2)	0.031(6)
0.021(5)	0.020(4)	0.034(8)

DCO^+/HCO^+ (20 K)

0.015(6)	0.017(5)	0.027(7)
0.018(4)	0.016(2)	0.031(6)
0.021(5)	0.020(4)	0.033(8)

DCO^+/HCO^+ (30 K)

1	4	7
2	5	8
3	6	9

position

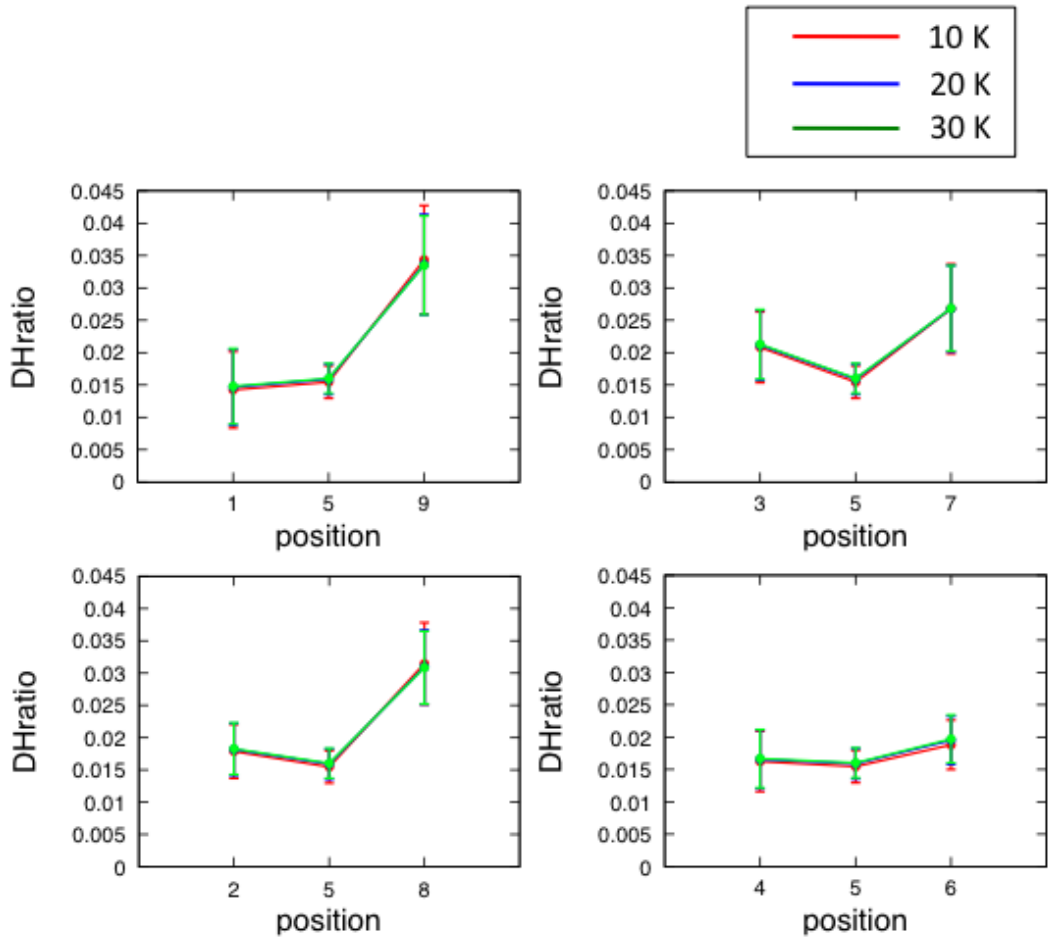

Figure 3.14: The deuterium fractionation ratio toward NGC1333-IRAS2A. The numbers in parentheses represent three times the standard deviation (3σ) in units of the best significant digits.

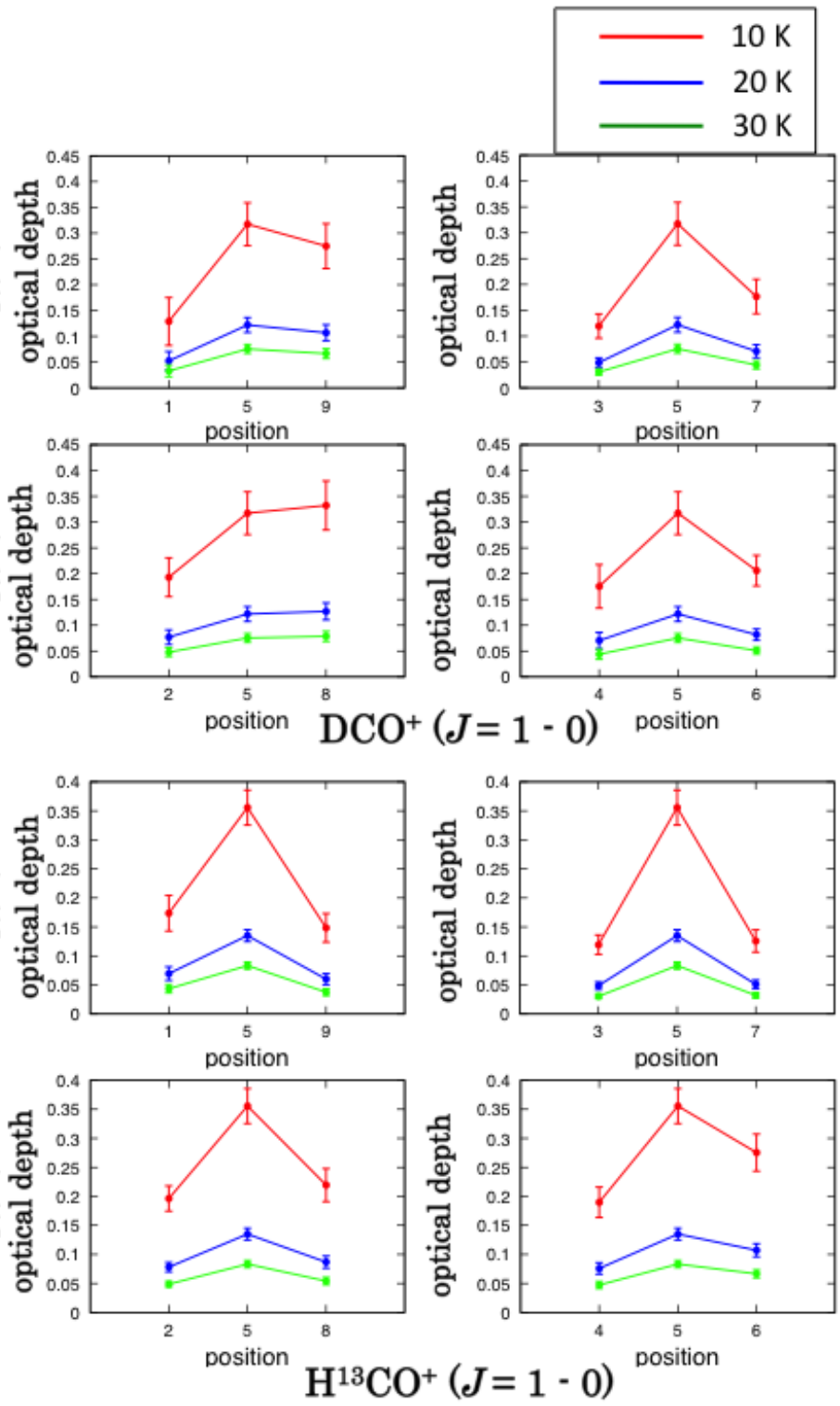

Figure 3.15: The optical depth toward NGC1333-IRAS2A. We show 3σ value for error.

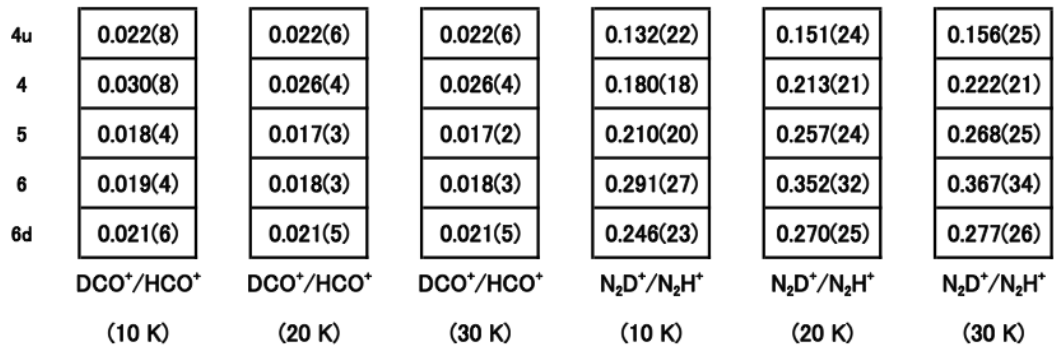

Figure 3.16: The deuterium fractionation ratio toward IRAS16293-2422. The numbers in parentheses represent three times the standard deviation (3σ) in units of the best significant digits.

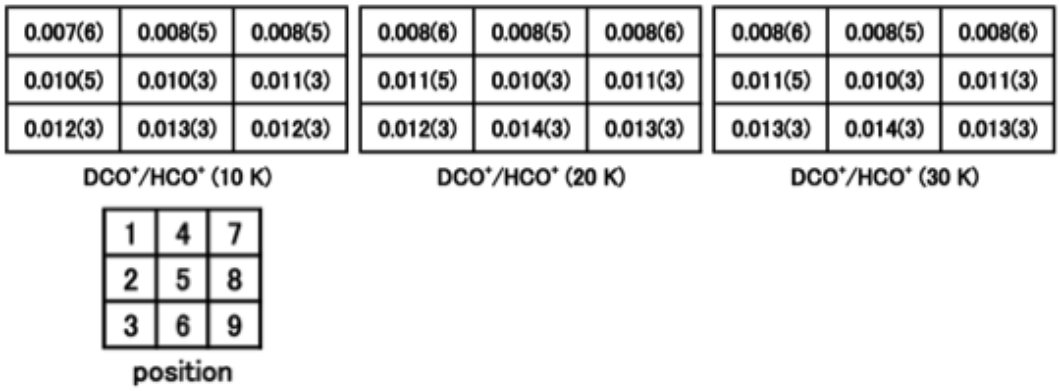

Figure 3.17: The deuterium fractionation ratio toward L1251A. The numbers in parentheses represent three times the standard deviation (3σ) in units of the best significant digits.

Chapter 4

Deuterium Fractionation of Neutral Species

4.1 Observation method

In this chapter, we describe observations of neutral species. The observed protostars are the same as those for the ionic species. Details of the observations are given in Chapter 3. We observed the $J = 1-0$ lines of DNC, $HN^{13}C$, DCN, $H^{13}CN$, $HC^{15}N$ and HCN toward L1551-IRS5, L483, NGC1333-IRAS2A and L1251A, and observed the $J = 1 - 0$ lines of DNC and $HN^{13}C$ toward IRAS16293-2422 by using the Nobeyama 45 m telescope (table 4.1). With the ASTE 10 m telescope, we observed the $J = 5 - 4$ lines of DCN, the $J = 4 - 3$ lines of $H^{13}CN$, CCD, CCH, HDCO, SO (table 4.1).

NRO 45 m telescope	
molecule (transition)	frequency [GHz]
DNC ($J = 1 - 0$)	76.3056995
$HN^{13}C$ ($J = 1 - 0$)	87.0908252
DCN ($J = 1 - 0$)	72.4146936
$H^{13}CN$ ($J = 1 - 0$)	86.3399215
$HC^{15}N$ ($J = 1 - 0$)	86.0549664
HCN ($J = 1 - 0$)	88.6316022

ASTE 10 m telescope	
molecule (transition)	frequency [GHz]
DCN ($J = 5 - 4$)	362.0457535
$H^{13}CN$ ($J = 4 - 3$)	345.3397694
HDCO ($J = 5_{1,4} - 4_{1,3}$)	335.0967820
CCD ($J = 5_6 - 4_5$)	360.6183400
CCH ($J = 4_5 - 3_4$)	349.3377056

Table 4.1: The observed spectral lines. Frequency is the value of CDMS (http://www.astro.uni-koeln.de/cdms/).

4.2 Results

4.2.1 Spectral line profile

L1551-IRS5

Figure 4.1 shows the spectra observed toward L1551-IRS5 with the Nobeyama 45 m telescope. The red numbers depicted in the upper left of each spectrum show the observational positions (table 3.1). For DNC and $HN^{13}C$, the integration time is longer for positions 4, 5 and 6 along the disk direction than for the other positions, and the S/N ratio is better at those positions. The DNC line was detected at all the nine positions. The line is relatively weak at the protostar position (position 5). The $HN^{13}C$ line is also detected at all the positions. It is generally stronger at the surrounding positions than at the protostar position. Such a distribution of $HN^{13}C$ is in contrast to the $H^{13}CO^+$ distribution which is centrally concentrated in this source. The spectra of DCN, $H^{13}CN$ and $HC^{15}N$ are fairly weak, but they are detected at several positions. The DCN line is rather weak at the protostar position in comparison with the surrounding positions (positions 1, 8 and 9), as in the case of DNC. Although the strong lines of the normal species (HCN) are detected, they are seriously affected by self absorption due to a foreground gas.

L483

Figure 4.2 shows the spectra observed toward L483 with the Nobeyama 45 m telescope. The red numbers shown in the upper left of each spectrum are the observational positions (table 3.1). The DNC emission peaks at the protostar position (position 5). This trend is the different from the DCO^+ case. The spectra at positions 7, 8 and 9 are stronger than the spectra at positions 1, 2 and 3, and a gradient over the cloud seems to exist. $HN^{13}C$ also shows a similar behavior as DNC. The distributions of DNC and $HN^{13}C$ are also similar to that of $H^{13}CO^+$ (figure 3.2). In addition, the lines of DCN, $H^{13}CN$ and $HC^{15}N$ are detected toward L483, where the hyperfine structures are resolved for DCN and $H^{13}CN$. Intensities of these lines are generally weaker than those of DNC and $HN^{13}C$. DCN is significantly strong at the protostar position in the disk direction as in the case of DNC, but the strong line is observed at position 8. In spite of a slight difference, DNC, $HN^{13}C$, DCN and $H^{13}CN$

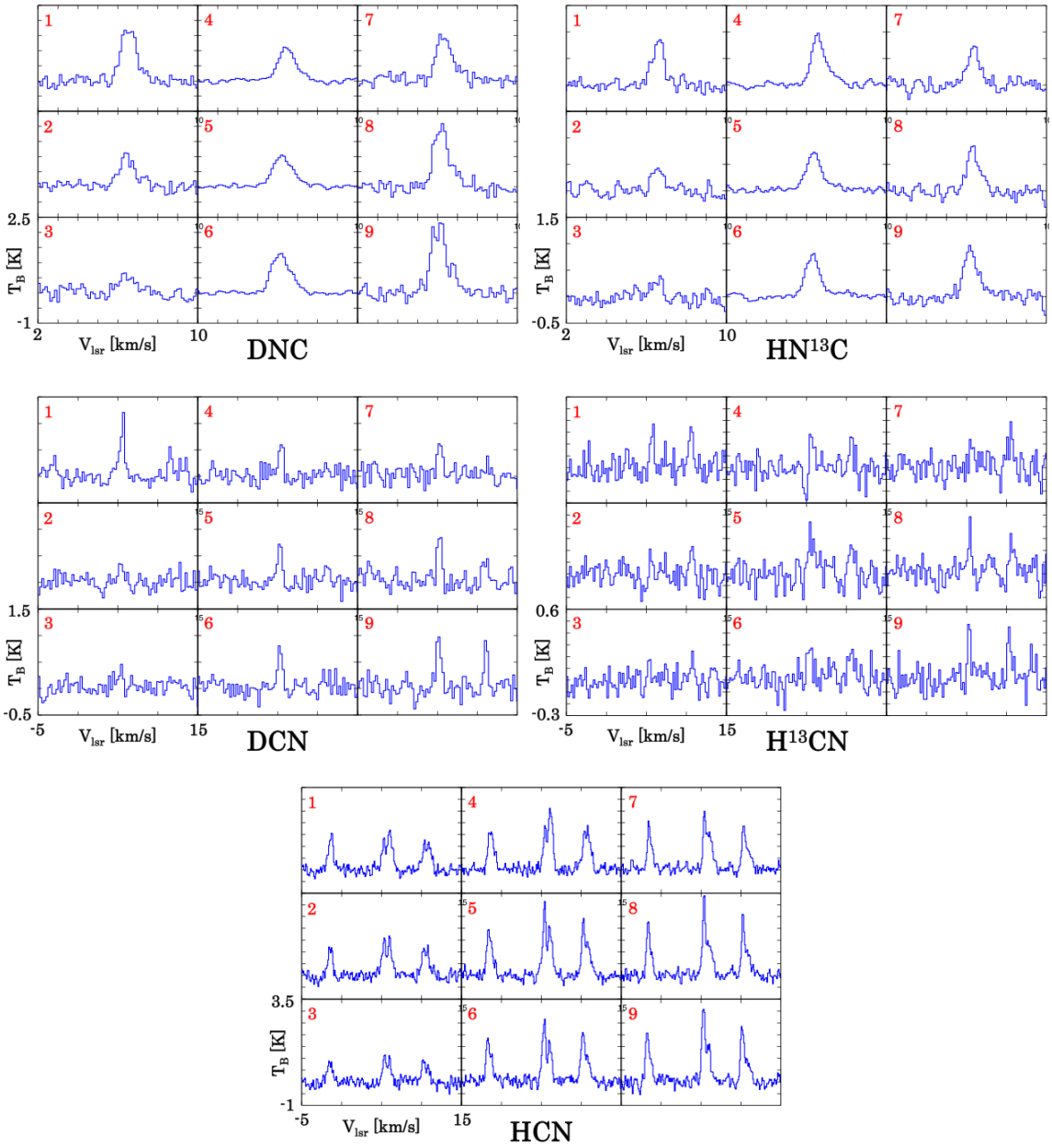

Figure 4.1: Spectra observed toward L1551 with the NRO 45 m telescope.

all show similar distributions. The spectral lines of HCN are bright, but they are seriously affected by the self-absorption effect, because a clear self-absorption dip is observed and the hyperfine intensity ratios are much different from those expected from the intrinsic line intensities. In addition, we observed the DCN, $H^{13}CN$, CCD and HDCO lines with the ASTE 10 m telescope. However, they were not detected.

NGC1333-IRAS2A

The spectral line observed toward NGC1333-IRAS2A with the Nobeyama 45 m telescope are shown in figure 4.3. The red numbers shown in the upper left of each spectrum indicate the observed positions (table 3.1). The DNC and $HN^{13}C$ lines have a similar distribution. They have a peak at position 7, and do not seem to show significant intensity enhancement toward the protostar position (position 5). There may exist a gradient from west to east. Such a feature contrasts with the DCO^+, $H^{13}CO^+$, and N_2H^+ cases (figure 3.4).

In addition, the lines of DCN and $H^{13}CN$ are detected toward NGC1333-IRAS2A. The hyperfine structure is resolved for these species. The distribution of DCN and $H^{13}CN$ are similar to each other. The spectral lines of $HC^{15}N$ are very weak, but it is confirmed to be the strongest at the protostar position among the nine observed positions. DCN, $H^{13}CN$, CCH and HDCO are detected at the protostar position by the observation with the ASTE 10 m telescope, while we could not detect the CCD lines.

IRAS16293-2422

Figure 4.4 shows the spectra toward IRAS16293-2422 observed with the Nobeyama 45 m telescope. The observed positions (table 3.1) are shown in the upper left of each spectrum in red. Again, the distribution along the strip is similar between DNC and $HN^{13}C$. They are also similar to the N_2H^+ distribution (figure 3.6). Furthermore, we observed DCN, $H^{13}CN$, CCD, CCH and HDCO with the ASTE 10 m telescope. The DCN, $H^{13}CN$ and HDCO lines are centrally concentrated around the protostar. At the protostar position, the line width of the spectra of DCN, $H^{13}CN$ and HDCO are wider than those of the DCO^+ and $H^{13}CO^+$ lines.

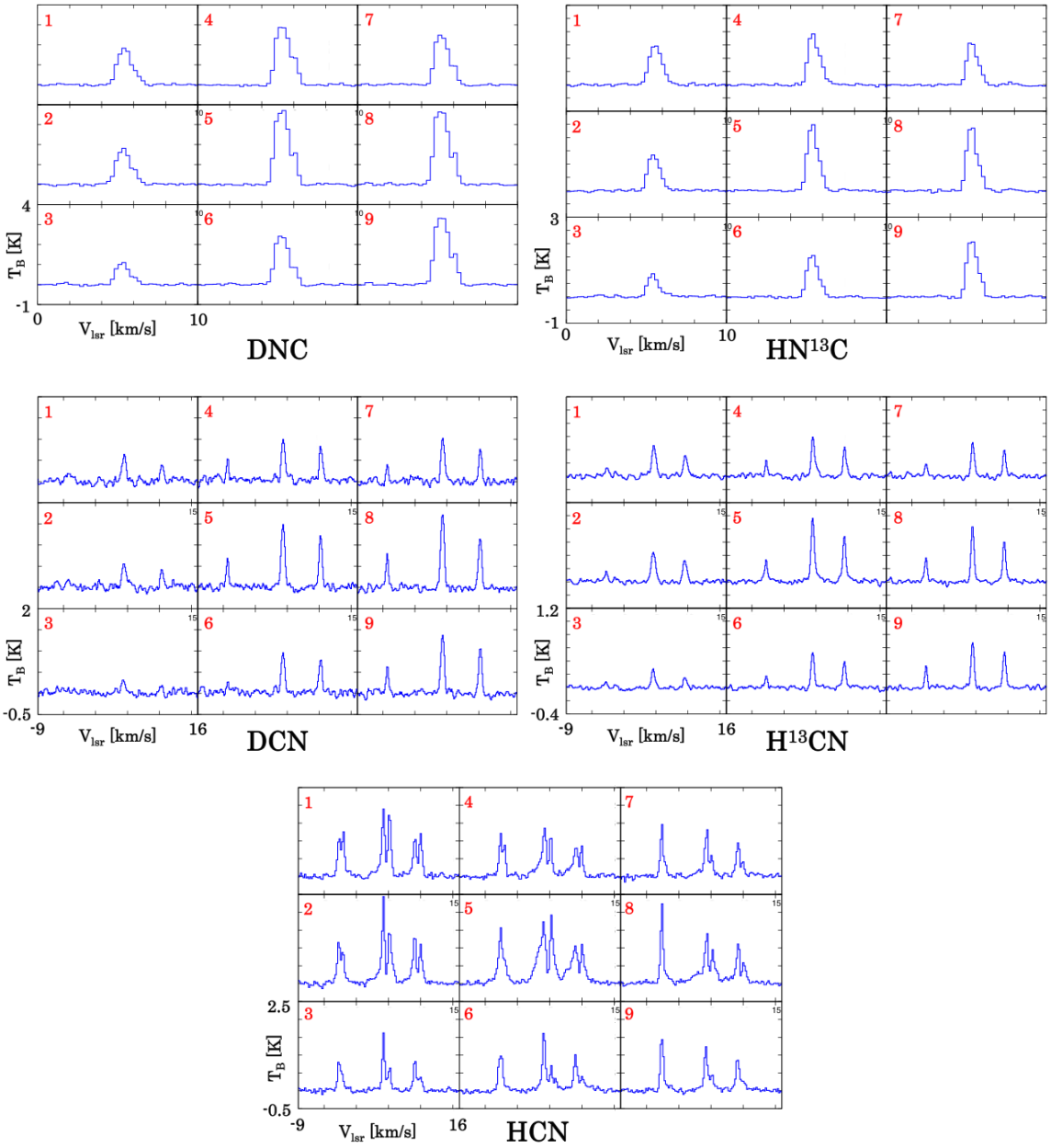

Figure 4.2: Spectra observed toward L483 with the NRO 45 m telescope.

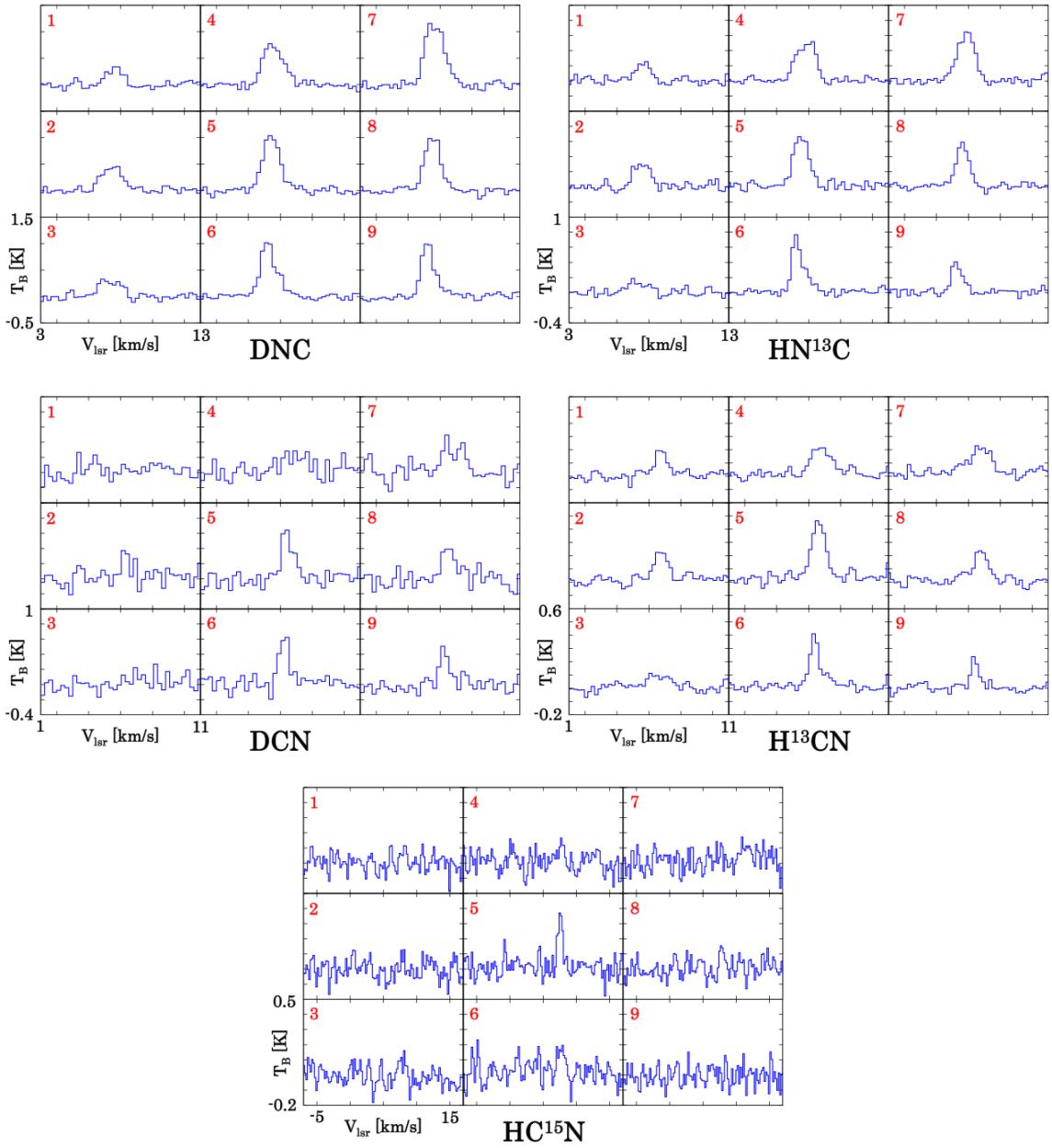

Figure 4.3: Spectra observed toward NGC1333-IRAS2A with the NRO 45 m telescope.

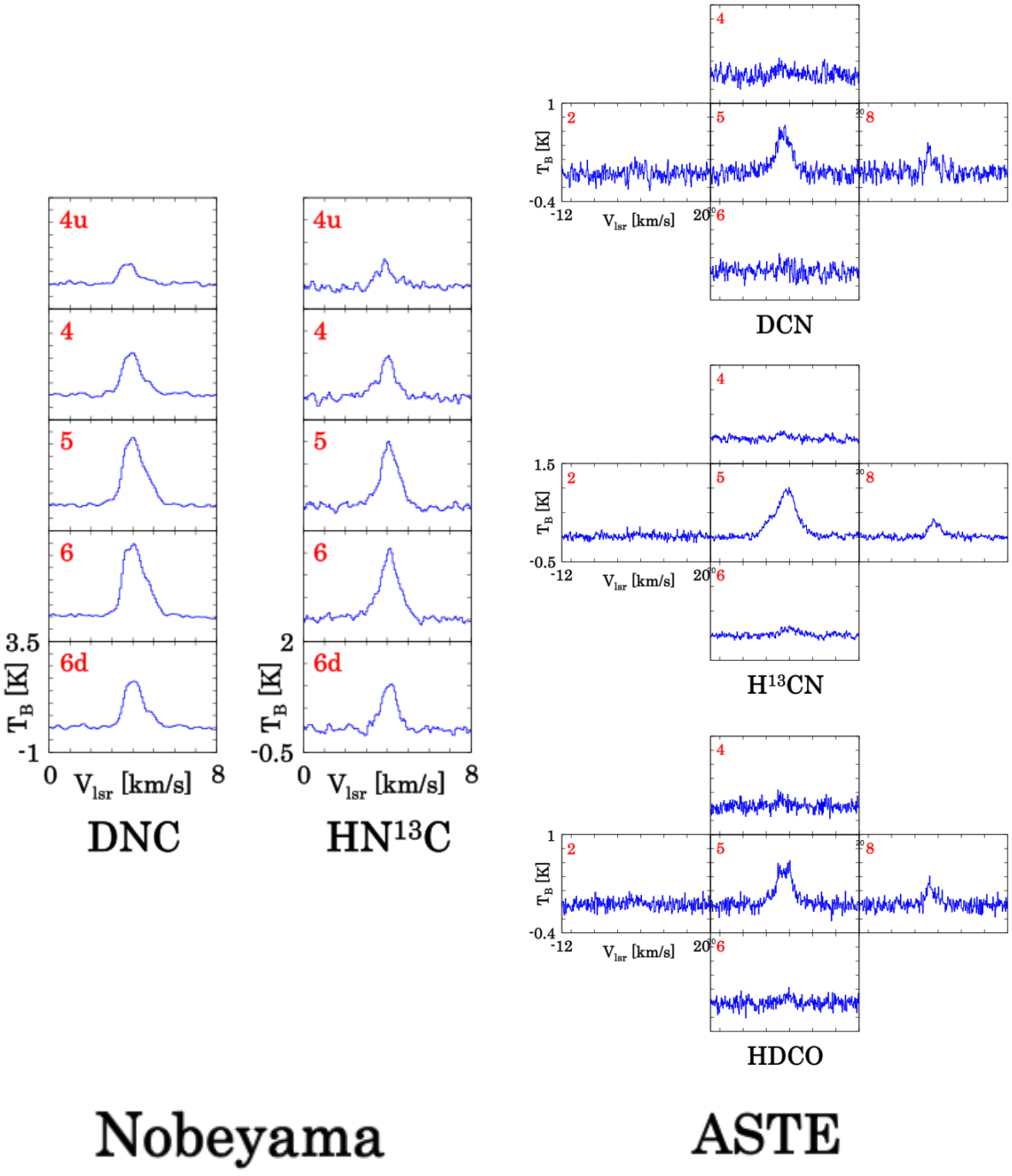

Figure 4.4: Spectra toward IRAS16293-2422.

L1251A

Figure 4.5 shows the spectra observed toward L1251A with the Nobeyama 45 m telescope. The distributuion of DNC shows a gradient from north to south, where the DNC line is brighter in the southern part. The distribution of $HN^{13}C$ is essentially similar to that of DNC. This trend is the same as that found for DCO^+ and $H^{13}CO^+$. The same trend can be confirmed by the weakest lines of N_2H^+ which are known as a density tracer. On the other hand, we could not detect the lines of DCN and $H^{13}CN$ at most positions because of the weakness of the lines. Nevertheless, DCN seems to exist only at positions 3 and 6, where the lines of DNC and $HN^{13}C$ are strong. The line of $H^{13}CN$ also looks strong at the protostar position.

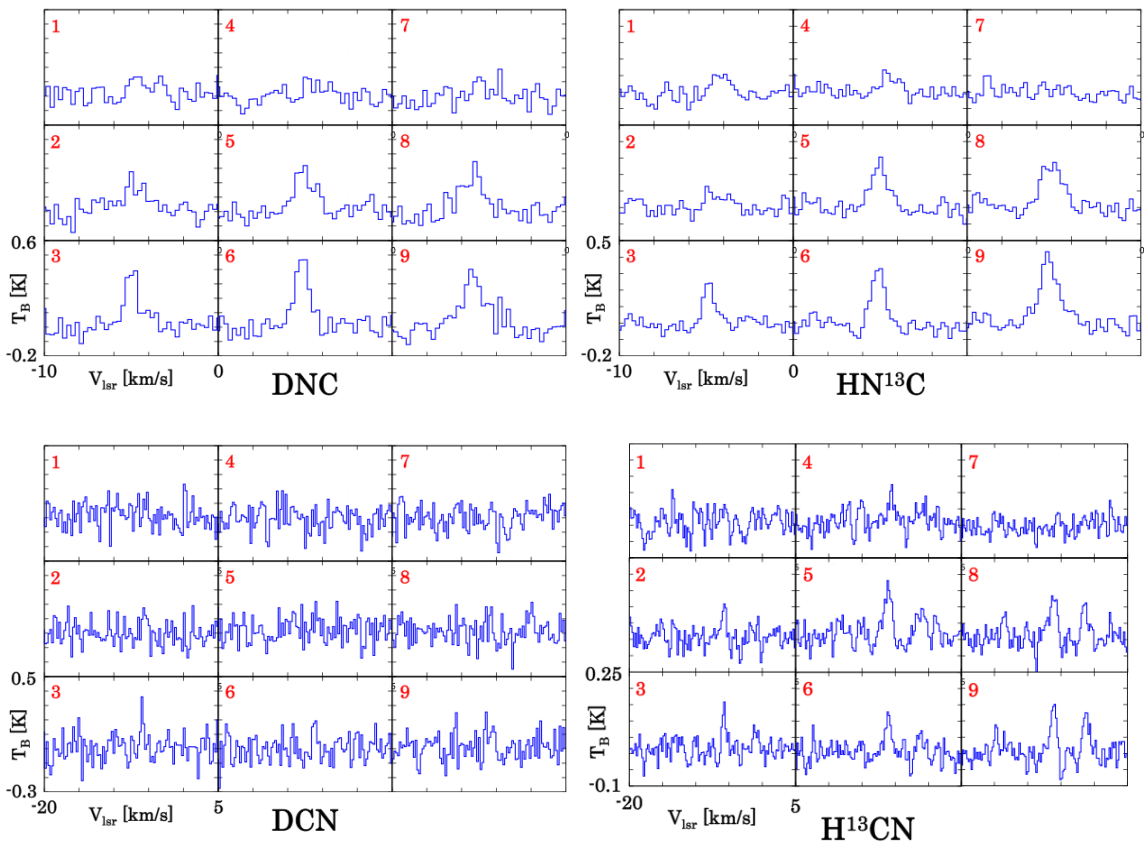

Figure 4.5: Spectra observed toward L1251A with the NRO 45 m telescope.

4.2.2 Spectral line parameters, optical depths and column densities

We derive the line parameters of each molecular line. For DNC and $HN^{13}C$, we conduct least-square fitting by equation (3.1), as in the case of the ionic species (Chapter 3), and calculate the brightness temperature $T_{\rm B}$, center velocity $v_{\rm lsr}$ and line width Δv. The integrated intensities are calculated directly from the spectra. We calculate the errors of the parameters by using the rms noise as discribed in Section 3.2.2.

The hyperfine structures are observed in the spectra of DCN ($J = 1 - 0$) and $H^{13}CN$ ($J = 1 - 0$) toward L483. For these lines, we conduct least-square fitting by the following equation:

$$y = \sum_{i=1}^{3} T_{{\rm B}_i} \tag{4.1}$$

$$= \sum_{i=1}^{3} T_0 \left[f(T_{\rm ex}) - f(T_{\rm bg}) \right] \left[1 - {\rm e}^{-\tau_i} \right] \exp\left[-\frac{4{\rm ln}2(x_i - v_{{\rm lsr}_i})^2}{\Delta v_i^2} \right], \tag{4.2}$$

and evaluate the optical depth τ, center velocity $v_{\rm lsr}$ and line width Δv. In some observation points, the hyperfine structures of the spectra of DCN ($J = 1 - 0$) and $H^{13}CN$ ($J = 1 - 0$) toward NGC1333-IRAS2A were also observed, but the S/N ratios are low and these lines are not enough for the fitting with equation (4.2). In such a case, we conduct fitting by equation (3.1). In calculating the integrated intensities of these molecules, we calculated the errors of the parameters by using the rms noise calculate by the average value in the range of $v = -30 - -10$ km/s to $20 - 40$ km/s, $v = -25 - -15$ km/s to $20 - 35$ km/s and $v = -20 - -10$ km/s to $25 - 40$ km/s. We used 3 σ value for the error. The results are shown in tables 4.2, 4.4, 4.5, 4.6, 4.8 and 4.9.

We evaluate the optical depths and the column densities of each molecule from the derived line parameters by assuming the LTE condition, as in the case of the ionic species (Section 3.2.3). For DNC and $HN^{13}C$, we calculate the optical depths and column densities from the integrated intensities by using equation (3.4) and (3.5). For DCN ($J = 1 - 0$) and $H^{13}CN$ ($J = 1 - 0$) toward L483, we derive the column densities from the optical depth (τ) by equation (3.6). In derivation of the column densities, the excitation temperature has to be fixed to 10 K, 20 K and 30 K, as explained in Section 3.2.3. The optical depths are mostly lower than unity: the highest optical depth is found toward position 8 of L483 for DNC. It should be noted that the effect of the optical depth is taken into account by using equation (3.5). The results of the column densities are shown in tables 4.3, 4.4, 4.5, 4.8 and 4.9.

along with the optical depth values. We also calculate the deuterium fractionation ratio of each molecule from the column densities. The results are shown in table 4.10. Here, we use the isotopic ratios $^{12}C/^{13}C = 59$ to evaluate the DNC/HNC ratios and the DCN/HCN ratios (Lucas et al. 1998).

	position	$T_{\rm B}$ [K]	$v_{\rm lsr}$ [km/s]	Δv [km/s]	$\int Tdv$ [K・km/s]
DNC	1	1.77(7)	6.542(18)	0.88(4)	1.6(2)
	2	0.99(7)	6.45(3)	0.93(8)	1.0(2)
	3	0.56(8)	6.45(7)	0.99(17)	0.6(2)
	4	1.08(2)	6.467(12)	1.05(3)	1.21(6)
	5	1.00(2)	6.250(12)	1.19(3)	1.22(7)
	6	1.27(3)	6.163(11)	1.11(3)	1.47(7)
	7	1.47(7)	6.33(2)	0.96(6)	1.5(2)
	8	1.96(9)	6.186(19)	0.89(4)	1.9(3)
	9	2.12(10)	6.08(2)	0.99(5)	2.2(2)
$HN^{13}C$	1	0.84(5)	6.594(19)	0.68(5)	0.64(16)
	2	0.44(5)	6.56(4)	0.66(9)	0.33(14)
	3	0.32(6)	6.54(6)	0.61(14)	0.15(16)
	4	0.89(3)	6.604(12)	0.85(3)	0.84(6)
	5	0.70(2)	6.373(14)	0.94(3)	0.74(6)
	6	0.78(2)	6.308(11)	0.84(3)	0.77(6)
	7	0.69(5)	6.36(3)	0.72(6)	0.53(16)
	8	0.78(5)	6.33(2)	0.74(6)	0.56(15)
	9	0.88(5)	6.21(2)	0.82(6)	0.82(15)
DCN	1	1.06(10)	5.59(3)	0.66(7)	0.8(3)
	2	0.37(10)	5.37(9)	0.7(2)	
	3	0.27(7)	5.12(17)	1.3(4)	
	4	0.67(11)	5.43(5)	0.63(13)	0.6(5)
	5	0.77(10)	5.28(4)	0.64(10)	0.6(3)
	6	0.82(10)	5.30(4)	0.66(9)	0.6(3)
	7	0.67(11)	5.31(6)	0.73(14)	0.5(6)
	8	0.97(11)	5.26(4)	0.64(9)	0.8(3)
	9	1.00(13)	5.15(4)	0.72(11)	0.8(3)
$H^{13}CN$	1	0.36(8)	5.75(6)	0.51(13)	
	2	0.3(12)	5.54(19)	0.2(7)	
	3	0.3(8)	5.36(4)	0.2(6)	
	4	0.29(7)	5.70(7)	0.55(16)	
	5	0.31(7)	5.64(10)	1.0(2)	
	6	0.29(7)	5.41(9)	0.7(2)	
	7	0.21(8)	5.66(11)	0.6(3)	
	8	0.48(9)	5.44(4)	0.37(7)	
	9	0.55(9)	5.34(3)	0.39(8)	

Table 4.2: Line parameters toward L1551-IRS5 observed with the Nobeyama 45 m telescope. The numbers in parentheses represent three times the standard deviation (3σ) in units of the best significant digits.

	position	τ (10 K)	τ (20 K)	τ (30 K)	$N/10^{12}$ [cm^{-2}] (10 K)	$N/10^{12}$ [cm^{-2}] (20 K)	$N/10^{12}$ [cm^{-2}] (30 K)
DNC	1	0.29(5)	0.113(17)	0.070(10)	4.0(7)	5.6(9)	7.6(12)
	2	0.16(4)	0.065(16)	0.041(10)	2.3(6)	3.4(9)	4.7(12)
	3	0.09(4)	0.035(15)	0.022(10)	1.3(6)	2.0(9)	2.7(12)
	4	0.172(11)	0.069(4)	0.043(3)	2.77(19)	4.1(3)	5.6(4)
	5	0.152(10)	0.061(4)	0.038(2)	2.77(19)	4.1(3)	5.6(4)
	6	0.200(12)	0.080(4)	0.050(3)	3.4(2)	5.0(3)	6.8(4)
	7	0.24(4)	0.094(15)	0.058(9)	3.5(7)	5.0(3)	6.9(12)
	8	0.35(6)	0.13(2)	0.081(12)	4.7(8)	6.6(10)	8.9(14)
	9	0.37(5)	0.138(17)	0.085(10)	5.6(8)	7.7(11)	10.4(14)
$HN^{13}C$	1	0.14(4)	0.056(15)	0.035(9)	1.1(3)	1.7(5)	2.3(6)
	2	0.07(3)	0.030(14)	0.019(9)	0.6(3)	0.9(4)	1.2(6)
	3	0.04(4)	0.015(16)	0.009(10)	0.3(3)	0.4(4)	5.4(6)
	4	0.146(13)	0.059(5)	0.037(3)	1.50(14)	2.2(2)	3.0(3)
	5	0.115(11)	0.047(4)	0.029(3)	1.30(13)	1.92(19)	2.6(3)
	6	0.133(11)	0.054(4)	0.034(3)	1.36(12)	1.99(17)	2.7(2)
	7	0.11(4)	0.044(14)	0.027(9)	0.9(3)	1.4(5)	1.9(6)
	8	0.11(3)	0.045(13)	0.028(8)	1.0(3)	1.5(4)	2.0(6)
	9	0.15(3)	0.059(12)	0.037(7)	1.5(3)	2.1(5)	2.9(6)
DCN	1	0.019(9)	0.008(4)	0.005(2)	0.6(3)	1.0(4)	1.3(6)
	2						
	3						
	4	0.014(13)	0.006(6)	0.004(3)	0.4(4)	0.7(6)	1.0(9)
	5	0.016(8)	0.007(3)	0.004(2)	0.5(2)	0.7(4)	1.0(5)
	6	0.015(9)	0.006(4)	0.004(2)	0.5(3)	0.7(4)	1.0(6)
	7	0.014(16)	0.006(7)	0.004(4)	0.4(5)	0.7(8)	0.9(11)
	8	0.020(8)	0.008(3)	0.005(2)	0.6(3)	0.9(4)	1.3(5)
	9	0.021(9)	0.009(4)	0.006(2)	0.6(3)	1.0(4)	1.4(6)

Table 4.3: Line parameters toward L1551-IRS5 observed with the Nobeyama 45 m telescope. The numbers in parentheses represent three times the standard deviation (3σ) in units of the best significant digits.

	position	$T_{\rm B}$ [K]	$v_{\rm lsr}$ [km/s]	Δv [km/s]	$\int Tdv$ [K•km/s]
DNC	1	1.82(4)	5.440(13)	1.07(3)	2.09(9)
	2	1.76(5)	5.371(14)	1.10(3)	2.06(8)
	3	1.10(4)	5.315(18)	0.99(4)	1.17(9)
	4	2.97(10)	5.353(19)	1.11(4)	3.47(9)
	5	3.80(13)	5.300(18)	1.08(4)	4.32(8)
	6	2.51(8)	5.283(16)	1.04(4)	2.75(9)
	7	2.54(8)	5.284(17)	1.05(4)	2.81(9)
	8	3.80(13)	5.274(19)	1.09(4)	4.38(9)
	9	3.44(12)	5.310(19)	1.12(4)	4.08(9)
$HN^{13}C$	1	1.52(3)	5.577(8)	0.926(19)	1.44(5)
	2	1.38(3)	5.468(9)	0.86(2)	1.23(6)
	3	0.85(3)	5.406(14)	0.77(3)	0.70(5)
	4	1.88(6)	5.446(12)	0.85(3)	1.67(5)
	5	2.45(5)	5.376(9)	0.80(2)	2.07(5)
	6	1.59(4)	5.370(9)	0.82(2)	1.37(6)
	7	1.59(4)	5.372(11)	0.80(3)	1.35(6)
	8	2.40(6)	5.341(10)	0.78(2)	1.99(6)
	9	2.15(5)	5.372(9)	0.80(2)	1.79(5)

	position	τ (10 K)	τ (20 K)	τ (30 K)	$N/10^{12}$ [cm^{-2}] (10 K)	$N/10^{12}$ [cm^{-2}] (20 K)	$N/10^{12}$ [cm^{-2}] (30 K)
DNC	1	0.310(18)	0.119(6)	0.074(4)	5.1(3)	7.2(4)	9.8(6)
	2	0.298(17)	0.115(6)	0.071(4)	5.0(3)	7.1(4)	9.6(6)
	3	0.175(17)	0.070(6)	0.044(4)	2.7(3)	3.9(4)	5.4(5)
	4	0.56(4)	0.198(10)	0.121(6)	9.5(7)	12.4(8)	16.6(11)
	5	0.79(5)	0.262(13)	0.158(7)	13.2(10)	16.0(10)	21.0(13)
	6	0.45(3)	0.166(9)	0.102(5)	7.2(5)	9.7(6)	13.0(8)
	7	0.46(3)	0.168(9)	0.103(5)	7.4(5)	9.9(7)	13.3(9)
	8	0.80(6)	0.265(14)	0.159(8)	13.4(11)	16.2(11)	21.3(14)
	9	0.69(4)	0.235(12)	0.142(7)	11.8(9)	14.9(10)	19.7(12)
$HN^{13}C$	1	0.240(11)	0.094(4)	0.059(3)	2.68(14)	3.82(18)	5.2(2)
	2	0.219(13)	0.087(5)	0.054(3)	2.27(15)	3.3(2)	4.4(3)
	3	0.134(12)	0.054(5)	0.034(3)	1.24(13)	1.82(18)	2.5(2)
	4	0.312(17)	0.120(6)	0.074(4)	3.2(2)	4.5(3)	6.0(4)
	5	0.440(19)	0.163(6)	0.100(4)	4.2(2)	5.7(3)	7.6(3)
	6	0.262(15)	0.102(5)	0.064(3)	2.58(16)	3.6(2)	4.9(3)
	7	0.262(17)	0.102(6)	0.064(4)	2.53(18)	3.6(2)	4.8(3)
	8	0.43(2)	0.160(7)	0.098(4)	4.1(2)	5.4(3)	7.3(4)
	9	0.369(18)	0.140(6)	0.086(4)	3.5(2)	4.9(3)	6.5(3)

Table 4.4: Line parameters toward L483 observed with the Nobeyama 45 m telescope. The numbers in parentheses represent three times the standard deviation (3σ) in units of the best significant digits.

	position	T_{ex} [K]	τ	v_{lsr} [km/s]	Δv [km/s]	$N/10^{12}$ [cm^{-2}]
DCN	1	10	0.051(3)	4.550(17)	0.62(5)	0.56(8)
	2	10	0.047(3)	4.560(19)	0.62(5)	0.52(8)
	3	10	0.026(3)	4.43(3)	0.55(8)	0.25(7)
	4	10	0.098(5)	4.450(11)	0.51(3)	0.88(10)
	5	10	0.154(5)	4.403(6)	0.485(17)	1.31(9)
	6	10	0.093(5)	4.403(10)	0.50(3)	0.81(9)
	7	10	0.100(4)	4.412(8)	0.47(2)	0.83(8)
	8	10	0.172(5)	4.388(5)	0.480(15)	1.45(8)
	9	10	0.143(5)	4.413(6)	0.459(18)	1.16(8)
$H^{13}CN$	1	10	0.0707(17)	4.693(9)	0.77(2)	0.70(4)
	2	10	0.0711(16)	4.600(8)	0.787(19)	0.72(3)
	3	10	0.0395(15)	4.582(12)	0.64(3)	0.33(3)
	4	10	0.093(2)	4.556(8)	0.640(19)	0.76(4)
	5	10	0.154(3)	4.504(6)	0.645(13)	1.27(5)
	6	10	0.0856(18)	4.497(6)	0.577(13)	0.63(3)
	7	10	0.083(2)	4.512(7)	0.579(16)	0.61(3)
	8	10	0.140(3)	4.473(5)	0.559(13)	1.00(4)
	9	10	0.116(3)	4.501(6)	0.554(14)	0.82(4)
DCN	1	20	0.0208(13)	4.550(17)	0.62(5)	0.84(12)
	2	20	0.0194(13)	4.560(19)	0.62(5)	0.78(12)
	3	20	0.0108(13)	4.43(3)	0.55(8)	0.38(10)
	4	20	0.040(2)	4.450(11)	0.51(3)	1.32(15)
	5	20	0.0613(19)	4.403(6)	0.487(18)	1.93(13)
	6	20	0.0379(18)	4.403(10)	0.50(3)	1.22(13)
	7	20	0.0406(17)	4.412(8)	0.47(2)	1.24(11)
	8	20	0.0684(18)	4.388(5)	0.482(15)	2.13(12)
	9	20	0.0574(19)	4.413(6)	0.461(18)	1.71(12)

Table 4.5: Line parameters toward L483 observed with the Nobeyama 45 m telescope. The numbers in parentheses represent three times the standard deviation (3σ) in units of the best significant digits.

	position	T_{ex} [K]	τ	v_{lsr} [km/s]	Δv [km/s]	$N/10^{12}$ [cm^{-2}]
$H^{13}CN$	1	20	0.0285(7)	4.693(9)	0.77(2)	1.02(5)
	2	20	0.0287(6)	4.601(8)	0.79(2)	1.05(5)
	3	20	0.0161(6)	4.582(12)	0.64(3)	0.48(4)
	4	20	0.0372(10)	4.556(8)	0.640(19)	1.10(6)
	5	20	0.0605(11)	4.504(6)	0.645(14)	1.81(7)
	6	20	0.0344(7)	4.497(6)	0.577(13)	0.92(4)
	7	20	0.0332(8)	4.512(7)	0.580(16)	0.89(5)
	8	20	0.0552(11)	4.473(6)	0.559(13)	1.43(6)
	9	20	0.0463(11)	4.501(6)	0.554(15)	1.19(6)
DCN	1	30	0.0131(8)	4.550(17)	0.62(5)	1.15(16)
	2	30	0.0122(8)	4.560(19)	0.62(5)	1.07(16)
	3	30	0.0068(8)	4.43(3)	0.55(8)	0.53(14)
	4	30	0.0249(13)	4.450(11)	0.51(3)	1.8(2)
	5	30	0.0382(12)	4.403(6)	0.487(18)	2.63(18)
	6	30	0.0237(11)	4.403(10)	0.50(3)	1.67(18)
	7	30	0.0255(11)	4.412(8)	0.47(2)	1.70(16)
	8	30	0.0426(11)	4.388(5)	0.482(15)	2.91(17)
	9	30	0.0359(12)	4.413(6)	0.461(18)	2.34(17)
$H^{13}CN$	1	30	0.0178(4)	4.693(9)	0.77(2)	1.39(7)
	2	30	0.0179(4)	4.601(8)	0.79(2)	1.42(7)
	3	30	0.0101(4)	4.582(12)	0.64(3)	0.65(5)
	4	30	0.0232(6)	4.556(8)	0.640(19)	1.50(8)
	5	30	0.0376(7)	4.504(6)	0.645(14)	2.45(10)
	6	30	0.0215(4)	4.497(6)	0.577(13)	1.25(5)
	7	30	0.0208(5)	4.512(7)	0.580(16)	1.22(6)
	8	30	0.0343(7)	4.473(6)	0.560(13)	1.94(9)
	9	30	0.0288(7)	4.501(6)	0.555(15)	1.61(8)

Table 4.5: continued.

	position	$T_{\rm B}$ [K]	$v_{\rm lsr}$ [km/s]	Δv [km/s]	$\int T dv$ [K•km/s]
DNC	1	0.33(4)	7.63(6)	1.11(14)	0.35(13)
	2	0.46(3)	7.46(4)	1.51(10)	0.74(12)
	3	0.31(3)	7.30(8)	1.55(19)	0.47(12)
	4	0.77(3)	7.54(3)	1.44(7)	1.16(12)
	5	1.06(3)	7.426(19)	1.22(4)	1.41(12)
	6	0.99(4)	7.23(2)	1.15(6)	1.25(12)
	7	1.18(4)	7.65(2)	1.39(6)	1.71(12)
	8	1.04(3)	7.526(19)	1.14(4)	1.26(12)
	9	1.01(4)	7.22(2)	0.93(5)	1.07(13)
$HN^{13}C$	1	0.25(3)	7.64(5)	1.03(13)	0.26(9)
	2	0.32(3)	7.56(5)	1.17(12)	0.38(9)
	3	0.14(2)	7.25(11)	1.5(3)	0.19(9)
	4	0.52(2)	7.84(3)	1.39(7)	0.74(9)
	5	0.68(3)	7.53(2)	1.13(5)	0.80(9)
	6	0.69(4)	7.29(2)	0.86(6)	0.67(10)
	7	0.65(2)	7.86(2)	1.23(5)	0.84(9)
	8	0.58(2)	7.632(17)	0.93(4)	0.56(9)
	9	0.39(3)	7.27(3)	0.81(7)	0.32(9)
DCN	1				
	2				
	3				
	4				
	5	0.61(7)	6.42(5)	0.87(11)	0.6(2)
	6	0.66(7)	6.23(4)	0.71(9)	0.5(2)
	7				
	8	0.42(7)	6.52(8)	0.96(19)	0.4(2)
	9	0.51(7)	6.24(4)	0.60(10)	0.4(3)
$H^{13}CN$	1	0.200(19)	6.76(4)	0.90(10)	0.22(6)
	2	0.24(2)	6.76(5)	1.06(11)	0.29(6)
	3	0.094(14)	6.60(13)	1.9(3)	0.17(7)
	4	0.214(15)	6.79(6)	1.60(13)	0.33(7)
	5	0.46(3)	6.62(3)	1.11(8)	0.55(7)
	6	0.38(3)	6.37(3)	0.77(6)	0.36(6)
	7	0.203(16)	6.70(8)	1.94(18)	0.39(6)
	8	0.227(19)	6.77(5)	1.19(11)	0.31(6)
	9	0.24(2)	6.40(3)	0.55(6)	0.17(7)

Table 4.6: Line parameters toward NGC1333-IRAS2A observed with the Nobeyama 45 m telescope. The numbers in parentheses represent three times the standard deviation (3σ) in units of the best significant digits.

	position	τ (10 K)	τ (20 K)	τ (30 K)	$N/10^{12}$ [cm^{-2}] (10 K)	$N/10^{12}$ [cm^{-2}] (20 K)	$N/10^{12}$ [cm^{-2}] (30 K)
DNC	1	0.044(17)	0.018(7)	0.012(4)	0.8(3)	1.1(5)	1.6(6)
	2	0.069(13)	0.029(5)	0.018(3)	1.6(3)	2.4(5)	3.4(6)
	3	0.043(12)	0.018(5)	0.011(3)	1.0(3)	1.5(5)	2.1(7)
	4	0.116(14)	0.048(6)	0.030(3)	2.6(3)	3.9(5)	5.3(7)
	5	0.173(17)	0.069(7)	0.043(4)	3.2(3)	4.8(5)	6.5(7)
	6	0.162(19)	0.065(7)	0.041(5)	2.8(4)	4.2(5)	5.7(7)
	7	0.186(17)	0.074(6)	0.046(4)	3.9(4)	5.8(6)	7.9(7)
	8	0.164(18)	0.066(7)	0.041(4)	2.9(3)	4.2(5)	5.8(7)
	9	0.17(2)	0.069(9)	0.043(6)	2.5(4)	3.6(5)	4.9(7)
$HN^{13}C$	1	0.036(13)	0.015(5)	0.009(3)	0.44(17)	0.7(3)	0.9(3)
	2	0.046(12)	0.019(5)	0.012(3)	0.65(18)	1.0(3)	1.3(4)
	3	0.018(10)	0.008(4)	0.005(3)	0.32(18)	0.5(3)	0.7(4)
	4	0.076(11)	0.031(4)	0.020(3)	1.28(19)	1.9(3)	2.6(4)
	5	0.103(13)	0.042(5)	0.026(3)	1.40(19)	2.1(3)	2.8(4)
	6	0.113(19)	0.046(8)	0.029(5)	1.2(2)	1.7(3)	2.4(4)
	7	0.099(12)	0.040(5)	0.025(3)	1.46(19)	2.2(3)	3.0(4)
	8	0.087(15)	0.036(6)	0.022(4)	0.97(17)	1.4(2)	2.0(3)
	9	0.056(17)	0.023(7)	0.015(4)	0.55(18)	0.8(3)	1.1(4)
DCN	1						
	2						
	3						
	4						
	5	0.013(5)	0.005(2)	0.0034(13)	0.48(19)	0.7(3)	1.0(4)
	6	0.012(5)	0.005(2)	0.0031(14)	0.4(2)	0.7(3)	0.9(4)
	7						
	8	0.009(5)	0.004(2)	0.0023(12)	0.33(18)	0.5(3)	0.7(4)
	9	0.009(6)	0.004(2)	0.0025(15)	0.3(2)	0.5(3)	0.7(4)
$H^{13}CN$	1	0.0045(11)	0.0019(5)	0.0012(3)	0.13(3)	0.20(5)	0.27(7)
	2	0.0059(12)	0.0025(5)	0.0016(3)	0.17(3)	0.26(5)	0.36(7)
	3	0.0036(14)	0.0015(6)	0.0010(4)	0.10(4)	0.15(6)	0.21(8)
	4	0.0067(13)	0.0028(6)	0.0018(4)	0.19(4)	0.30(6)	0.41(8)
	5	0.0116(15)	0.0049(6)	0.0031(4)	0.33(4)	0.50(6)	0.68(9)
	6	0.0079(13)	0.0033(6)	0.0021(4)	0.21(4)	0.33(5)	0.45(8)
	7	0.0080(13)	0.0034(6)	0.0021(3)	0.23(4)	0.35(6)	0.48(8)
	8	0.0063(13)	0.027(5)	0.0017(3)	0.18(4)	0.28(6)	0.38(8)
	9	0.0037(15)	0.0015(6)	0.0010(4)	0.10(4)	0.15(6)	0.21(8)

Table 4.7: Line parameters toward NGC1333-IRAS2A observed with the Nobeyama 45 m telescope. The numbers in parentheses represent three times the standard deviation (3σ) in units of the best significant digits.

	position	$T_{\rm B}$ [K]	$v_{\rm lsr}$ [km/s]	Δv [km/s]	$\int T dv$ [K・km/s]
DNC	4u	0.82(2)	3.788(15)	0.98(3)	0.90(10)
	4	1.68(3)	3.951(10)	1.09(2)	2.02(10)
	5	2.67(4)	4.049(10)	1.25(2)	3.60(9)
	6	2.93(5)	4.063(11)	1.25(3)	3.91(10)
	6d	1.91(4)	4.052(10)	1.09(2)	2.28(10)
$HN^{13}C$	4u	0.47(3)	3.89(3)	0.91(6)	0.48(14)
	4	0.83(3)	3.996(17)	0.99(4)	0.94(14)
	5	1.37(3)	4.106(11)	1.07(2)	1.65(16)
	6	1.41(3)	4.099(10)	1.13(2)	1.76(12)
	6d	1.03(3)	4.095(11)	0.89(3)	0.98(13)

	position	τ (10 K)	τ (20 K)	τ (30 K)	$N/10^{12}$ [cm^{-2}] (10 K)	$N/10^{12}$ [cm^{-2}] (20 K)	$N/10^{12}$ [cm^{-2}] (30 K)
DNC	4u	0.13(2)	0.054(6)	0.034(4)	2.0(3)	3.0(4)	4.1(5)
	4	0.29(2)	0.113(6)	0.070(4)	4.9(3)	6.9(4)	9.4(6)
	5	0.50(2)	0.183(6)	0.112(4)	9.6(4)	12.8(5)	17.1(7)
	6	0.56(2)	0.200(7)	0.122(4)	10.7(5)	14.0(6)	18.7(7)
	6d	0.34(2)	0.129(7)	0.080(4)	5.6(3)	7.9(4)	10.7(6)
$HN^{13}C$	4u	0.07(2)	0.031(9)	0.019(6)	0.8(3)	1.2(4)	1.7(5)
	4	0.14(2)	0.057(9)	0.035(6)	1.7(3)	2.4(4)	3.3(5)
	5	0.24(3)	0.093(10)	0.058(6)	3.1(3)	4.4(5)	5.9(6)
	6	0.24(2)	0.094(7)	0.059(4)	3.3(3)	4.7(4)	6.3(5)
	6d	0.16(2)	0.066(9)	0.041(6)	1.8(3)	2.6(4)	3.5(5)

Table 4.8: Line parameters toward IRAS16293-2422 observed with the Nobeyama 45 m telescope. The numbers in parentheses represent three times the standard deviation (3σ) in units of the best significant digits.

	position	$T_{\rm B}$ [K]	$v_{\rm lsr}$ [km/s]	Δv [km/s]	$\int Tdv$ [K・km/s]
DNC	1	0.11(3)	−4.3(2)	1.8(5)	0.16(17)
	2	0.17(3)	−4.80(16)	1.9(4)	0.38(16)
	3	0.39(4)	−4.98(4)	0.89(10)	0.45(16)
	4	0.09(3)	−4.4(2)	1.5(6)	0.15(16)
	5	0.28(3)	−5.06(7)	1.34(16)	0.38(14)
	6	0.49(3)	−5.18(3)	0.96(8)	0.52(15)
	7	0.15(6)	−5.00(11)	0.6(3)	0.1(4)
	8	0.25(3)	−5.39(10)	1.5(2)	0.41(15)
	9	0.33(3)	−5.33(8)	1.59(19)	0.59(16)
$HN^{13}C$	1	0.11(3)	−4.16(12)	1.0(3)	0.05(9)
	2	0.08(2)	−4.38(18)	1.4(4)	0.08(9)
	3	0.25(3)	−4.86(3)	0.69(8)	0.16(10)
	4	0.105(18)	−4.49(9)	1.1(2)	0.12(10)
	5	0.26(2)	−5.05(5)	1.09(11)	0.30(9)
	6	0.34(3)	−5.11(3)	0.83(8)	0.24(9)
	7	0.02(2)	−5.2(8)	1.4(18)	0.03(10)
	8	0.27(2)	−5.13(5)	1.38(12)	0.37(8)
	9	0.39(2)	−5.29(4)	1.24(8)	0.54(8)

	position	τ (10 K)	τ (20 K)	τ (30 K)	$N/10^{12}$ [cm^{-2}] (10 K)	$N/10^{12}$ [cm^{-2}] (20 K)	$N/10^{12}$ [cm^{-2}] (30 K)
DNC	1	0.013(13)	0.005(6)	0.003(4)	0.3(4)	0.5(6)	0.7(8)
	2	0.027(13)	0.011(5)	0.007(3)	0.8(4)	1.3(6)	1.7(9)
	3	0.07(3)	0.030(11)	0.019(7)	1.0(4)	1.5(6)	2.0(8)
	4	0.014(16)	0.006(7)	0.004(4)	0.3(4)	0.5(6)	0.7(8)
	5	0.040(16)	0.017(6)	0.011(4)	0.8(3)	1.3(5)	1.7(7)
	6	0.08(2)	0.032(10)	0.020(6)	1.1(4)	1.7(5)	2.4(7)
	7	0.04(11)	0.02(5)	0.01(3)	0.3(9)	0.5(14)	0.6(19)
	8	0.038(15)	0.016(6)	0.010(4)	0.9(4)	1.4(6)	1.9(8)
	9	0.052(16)	0.022(7)	0.014(4)	1.3(4)	1.9(6)	2.7(9)
$HN^{13}C$	1	0.007(12)	0.003(5)	0.002(3)	0.08(15)	0.1(2)	0.2(3)
	2	0.008(9)	0.003(4)	0.002(2)	0.14(16)	0.2(2)	0.3(3)
	3	0.03(2)	0.014(9)	0.009(5)	0.27(17)	0.4(3)	0.6(4)
	4	0.015(13)	0.006(5)	0.004(3)	0.19(17)	0.3(3)	0.4(4)
	5	0.038(12)	0.016(5)	0.010(3)	0.51(17)	0.8(3)	1.0(3)
	6	0.040(16)	0.017(6)	0.010(4)	0.40(16)	0.6(2)	0.8(3)
	7	0.003(11)	0.001(5)	0.001(3)	0.05(19)	0.1(3)	0.1(4)
	8	0.038(9)	0.016(4)	0.010(2)	0.63(16)	1.0(2)	1.3(3)
	9	0.062(11)	0.026(4)	0.016(3)	0.93(17)	1.4(3)	1.9(3)

Table 4.9: Line parameters toward L1251A observed with the Nobeyama 45 m telescope. The numbers in parentheses represent three times the standard deviation (3σ) in units of the best significant digits.

		10 K	20 K	30 K	literature data
DNC /HNC	1	0.06(2)	0.058(19)	0.057(18)	
	2	0.07(4)	0.07(4)	0.07(4)	
	3	0.09(10)	0.09(10)	0.09(10)	
	4	0.031(4)	0.031(4)	0.031(3)	
	5	0.036(4)	0.036(4)	0.036(4)	0.036(4)
	6	0.043(5)	0.042(4)	0.042(4)	
	7	0.06(3)	0.06(2)	0.06(2)	
	8	0.08(3)	0.08(3)	0.08(3)	
	9	0.065(17)	0.062(16)	0.061(15)	

L1551-IRS5

		10 K	20 K	30 K	literature data
DNC /HNC	1	0.029(16)	0.029(16)	0.029(16)	
	2	0.042(14)	0.042(14)	0.042(14)	
	3	0.05(3)	0.05(3)	0.05(3)	
	4	0.034(7)	0.034(7)	0.034(7)	
	5	0.039(7)	0.039(6)	0.039(6)	
	6	0.041(9)	0.041(9)	0.041(9)	
	7	0.046(7)	0.045(7)	0.045(7)	
	8	0.050(11)	0.050(10)	0.050(10)	
	9	0.08(3)	0.07(3)	0.07(3)	

NGC1333-IRAS2A

		10 K	20 K	30 K	literature data
DNC /HNC	1	0032(3)	0.032(2)	0.032(2)	
	2	0.037(3)	0.037(3)	0.037(3)	
	3	0.037(5)	0.037(5)	0.037(5)	
	4	0.050(5)	0.047(4)	0.046(4)	
	5	0.053(5)	0.048(4)	0.047(4)	
	6	0.047(4)	0.045(4)	0.045(4)	
	7	0.049(5)	0.047(4)	0.047(4)	
	8	0.056(6)	0.050(4)	0.050(4)	
	9	0.057(5)	0.052(4)	0.051(4)	
DCN /HCN	1	0.014(2)	0.014(2)	0.014(2)	
	2	0.012(2)	0.013(2)	0.013(2)	
	3	0.013(4)	0.014(4)	0.014(4)	
	4	0.020(3)	0.020(3)	0.020(3)	
	5	0.0175(14)	0.0180(14)	0.0182(14)	
	6	0.022(3)	0.022(3)	0.023(3)	
	7	0.023(2)	0.024(3)	0.024(3)	
	8	0.0246(18)	0.0252(18)	0.0254(19)	
	9	0.024(2)	0.024(2)	0.025(2)	

L483

		10 K	20 K	30 K	literature data
DNC /HNC	4u	0.042(14)	0.042(14)	0.042(14)	
	4	0.050(9)	0.048(9)	0.048(8)	
	5	0.053(7)	0.050(6)	0.049(5)	0.09
	6	0.056(5)	0.051(5)	0.050(4)	
	6d	0.054(9)	0.052(8)	0.052(8)	

IRAS16293-2422

		10 K	20 K	30 K	literature data
DNC /HNC	1	0.07(15)	0.07(15)	0.07(15)	
	2	0.10(12)	0.10(12)	0.10(12)	
	3	0.06(5)	0.06(5)	0.06(5)	
	4	0.03(4)	0.03(4)	0.03(4)	
	5	0.028(14)	0.028(14)	0.028(14)	
	6	0.05(3)	0.05(2)	0.05(2)	
	7	0.1(5)	0.1(5)	0.1(5)	
	8	0.024(12)	0.024(12)	0.024(12)	
	9	0.023(9)	0.024(9)	0.024(9)	

L1251A

Table 4.10: Deuterium fractionation ratios observed with the Nobeyama 45 m telescope. The numbers in parentheses represent three times the standard deviation (3σ) in units of the best significant digits. The literature data are taken from Hirota et al. (2001), Wootten et al. (1982) and Lis et al. (2002).

4.3 Discussion

Here, we summarize the distributions of the deuterium fractionation ratios of DNC/HNC toward L1551-IRS5, IRAS16293-2422 and L1251A, and those of DNC/HNC and DCN/HCN toward L483 and NGC1333-IRAS2A.

4.3.1 L1551-IRS5

The top panel of figure 4.6 shows distribution of the deuterium fractionation ratio DNC/HNC around the protostar. The deuterium fractionation ratio seems to be relatively low at the disk direction (positions 4, 5 and 6), but there seems to be no clear dip at the protostar position (position 5). Although the ratio at the position 8 is relatively high, no significant gradient over the cloud can be seen in the deuterium fractionation ratio.

We consider the ratio along a few directions through the center position: positions 1, 5 and 9, positions 2, 5 and 8, positions 3, 5 and 7, and positions 4, 5 and 6. The DNC/HNC ratios seems to be low at the protostar position compared with the ambient positions. However, the error is quite large, so no clear dip can not be seen. Toward the disk direction (positions 4, 5 and 6), there exists no dip for the DNC/HNC ratio toward the protostar position. Above all, the deuterium fractionation of DNC does not decrease at the protostar position unlike in the case of the DCO^+/HCO^+ ratio.

In figure 4.7, we show the optical depths of DNC and $HN^{13}C$. Since the variation of the optical depth of DNC along various directions through the protostar is similar to that of $HN^{13}C$, no dip of the deuterium fractionation ratio is expected toward the protostar position: only a gradient of the deuterium fractionation ratio is seen.

4.3.2 L483

Figure 4.8 shows the distribution of the deuterium fractionation ratios DNC/HNC and DCN/HCN. The DNC/HNC ratio shows a slight gradient from northeast to southwest. The deuterium fractionation ratios at positions 4, 5, 6 and 7 are comparable to one another, while those at positions 8 and 9 are relatively high and those at positions 1, 2 and 3 are lower.

We consider the ratio along a few direction through the protostar position (figure 4.9). A decrease of the DNC/HNC ratios at the protostar position is not clearly seen for each direction. This result contrasts with the L1551-IRS5 case.

0.060(20)	0.031(4)	0.064(25)
0.069(39)	0.036(4)	0.082(29)
0.085(104)	0.043(5)	0.065(17)

DNC/HNC (10 K)

0.058(19)	0.031(4)	0.062(24)
0.068(37)	0.036(4)	0.077(26)
0.085(103)	0.042(4)	0.062(16)

DNC/HNC (20 K)

0.057(18)	0.031(3)	0.062(23)
0.067(37)	0.036(4)	0.076(26)
0.085(102)	0.042(4)	0.061(15)

DNC/HNC (30 K)

1	4	7
2	5	8
3	6	9

position

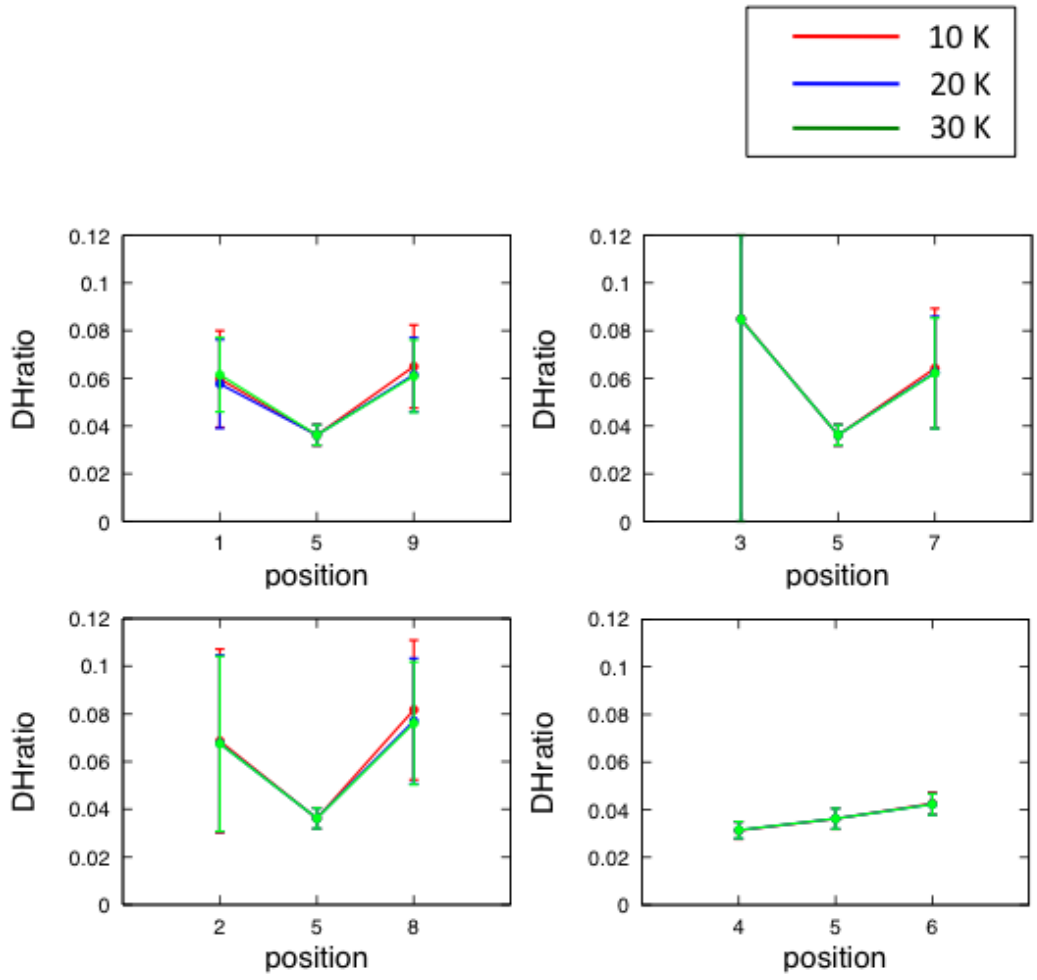

Figure 4.6: The deuterium fractionation ratio toward L1551-IRS5. The numbers in parentheses represent three times the standard deviation (3σ) in units of the best significant digits.

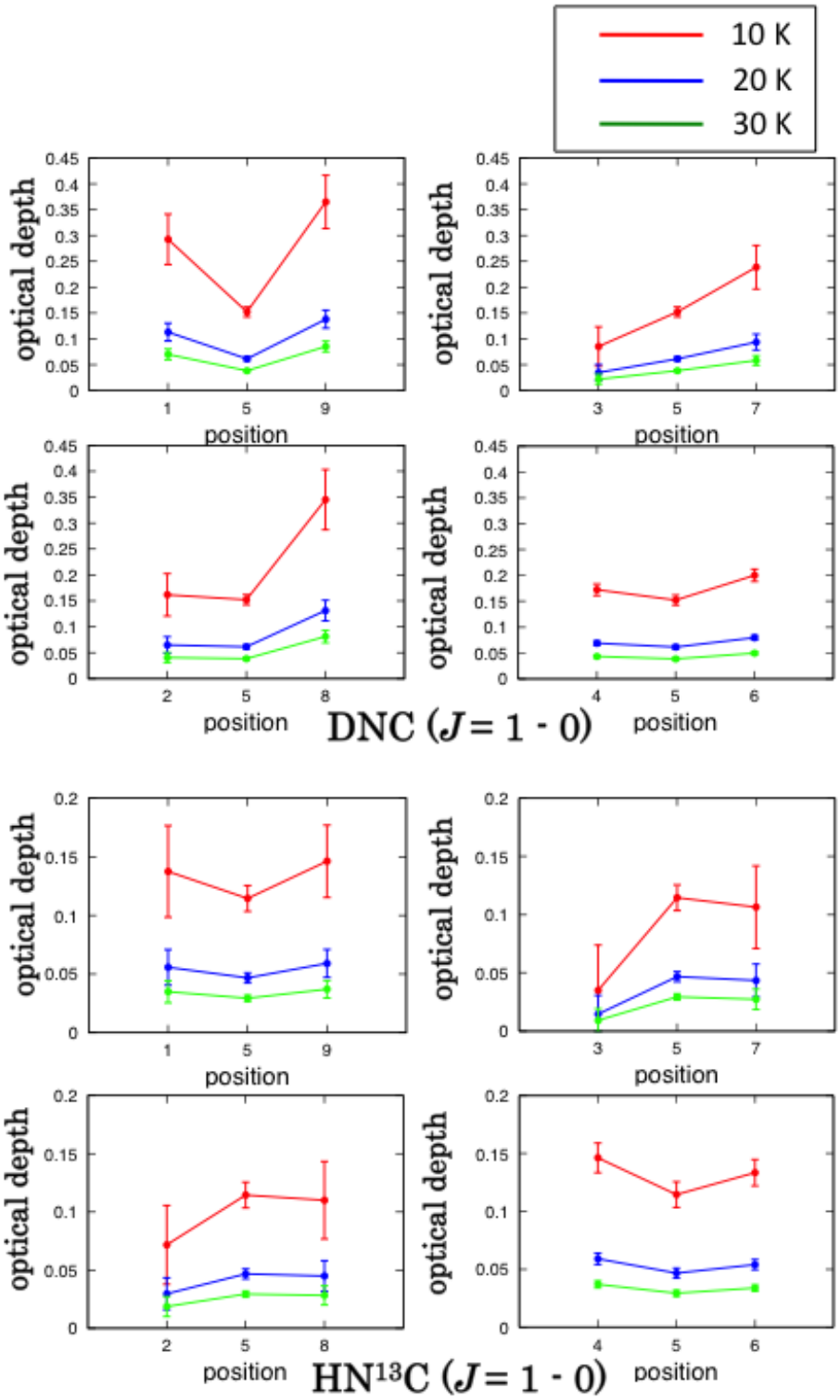

Figure 4.7: The optical depth toward L1551-IRS5. We show 3σ value for the error.

The deuterium fractionation ratio DCN/HCN also shows a similar trend as seen in the DNC/HNC ratio. A slight gradient over the cloud from northeast to southwest is visible in the DCN/HCN ratio. Figure 4.9 shows the deuterium fractionation ratio of DCN/HCN for each direction. We cannot confirm the dip toward the protostar position as in the case of the DNC/HNC ratio. The DCN/HCN ratio does not decline at the protostar position.

Figure 4.10 shows the optical depths of DNC and $HN^{13}C$. The optical depths of DNC and $HN^{13}C$ show a similar behavior, although that at the protostar position (position 5) seems to be higher than that at the other positions. Hence, no dip of the deuterium fractionation ratio is expected at the protostar position.

4.3.3 NGC1333-IRAS2A

The distribution of the deuterium fractionation ratio DNC/HNC is shown in the upper panel of figure 4.11. The deuterium fractionation ratio of DNC/HNC is almost constant for the observed position except for position 9.

We examine the deuterium fractionation ratios of each direction (figure 4.11). Although a slight decrease of the ratio at the protostar position is seen along the direction (2, 5, 8), the ratio toward the protostar position is not significantly decreased. This result contrasts with the DCO^+/HCO^+ ratio in this source.

We plot the optical depths of DNC and $HN^{13}C$ in figure 4.12. The optical depths of DNC and $HN^{13}C$ show a similar behavior, and hence, it is natural that the dip of the deuterium fractionation ratio cannot be found toward the protostar position.

4.3.4 IRAS16293-2422

Figure 4.13 shows the deuterium fractionation ratio DNC/HNC. We conducted a five-strip observation vertical to the outflow direction (along the disk direction). The deuterium fractionation ratio around the protostar seems to be almost constant.

4.3.5 L1251A

Figure 4.14 shows the distribution of the deuterium fractionation ratio DNC/HNC. We can not see a clear variation of the deuterium fractionation ratio over the cloud within the estimated errors, inspite of the significant gradient of the column densities of DNC and $HN^{13}C$ from north to south.

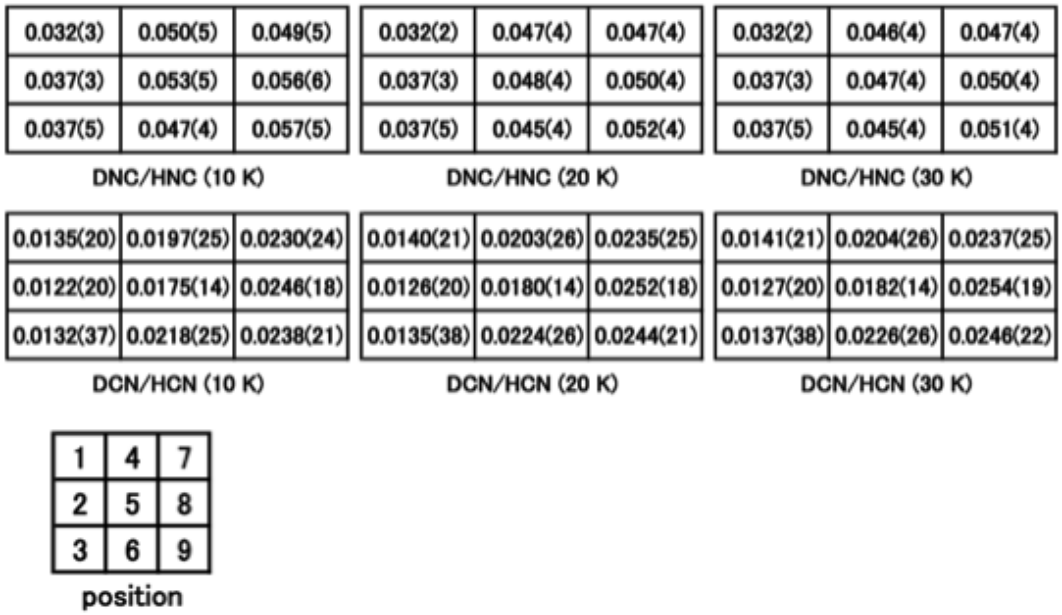

Figure 4.8: The deuterium fractionation ratios toward L483. The numbers in parentheses represent three times the standard deviation (3σ) in units of the best significant digits.

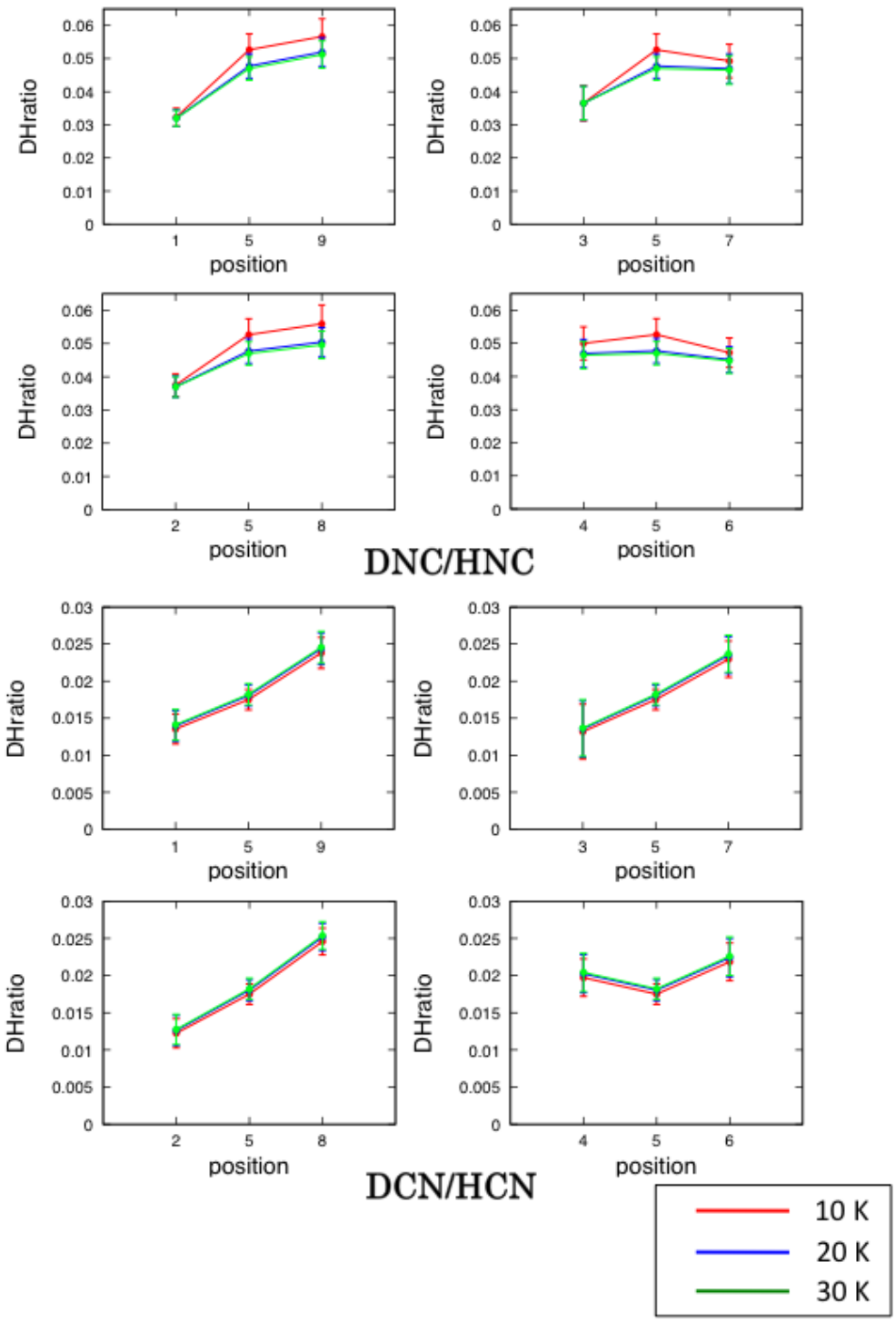

Figure 4.9: The deuterium fractionation ratios plotted for each direction toward L483. We show 3σ value for the error.

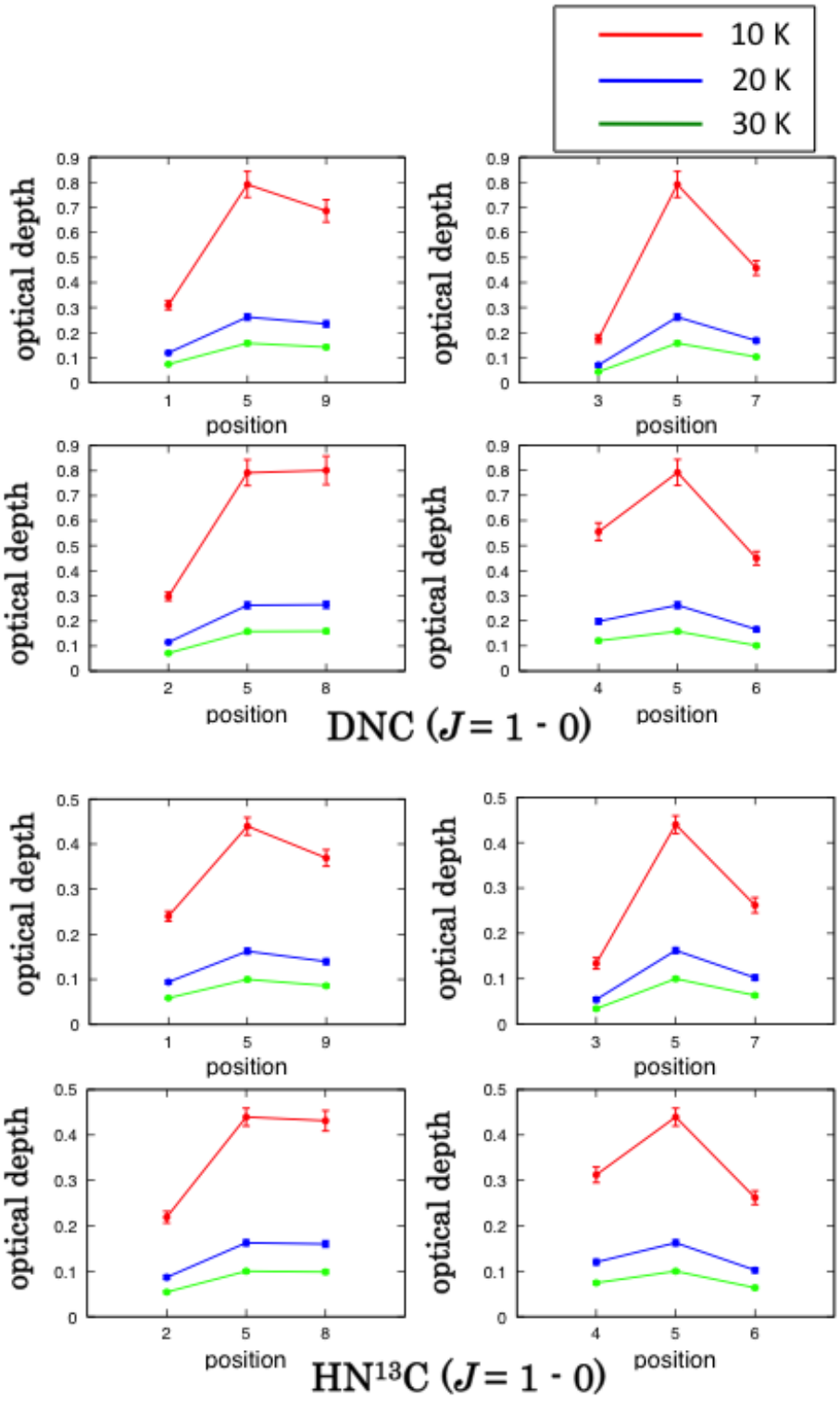

Figure 4.10: The optical depth toward L483. We show 3σ value for the error.

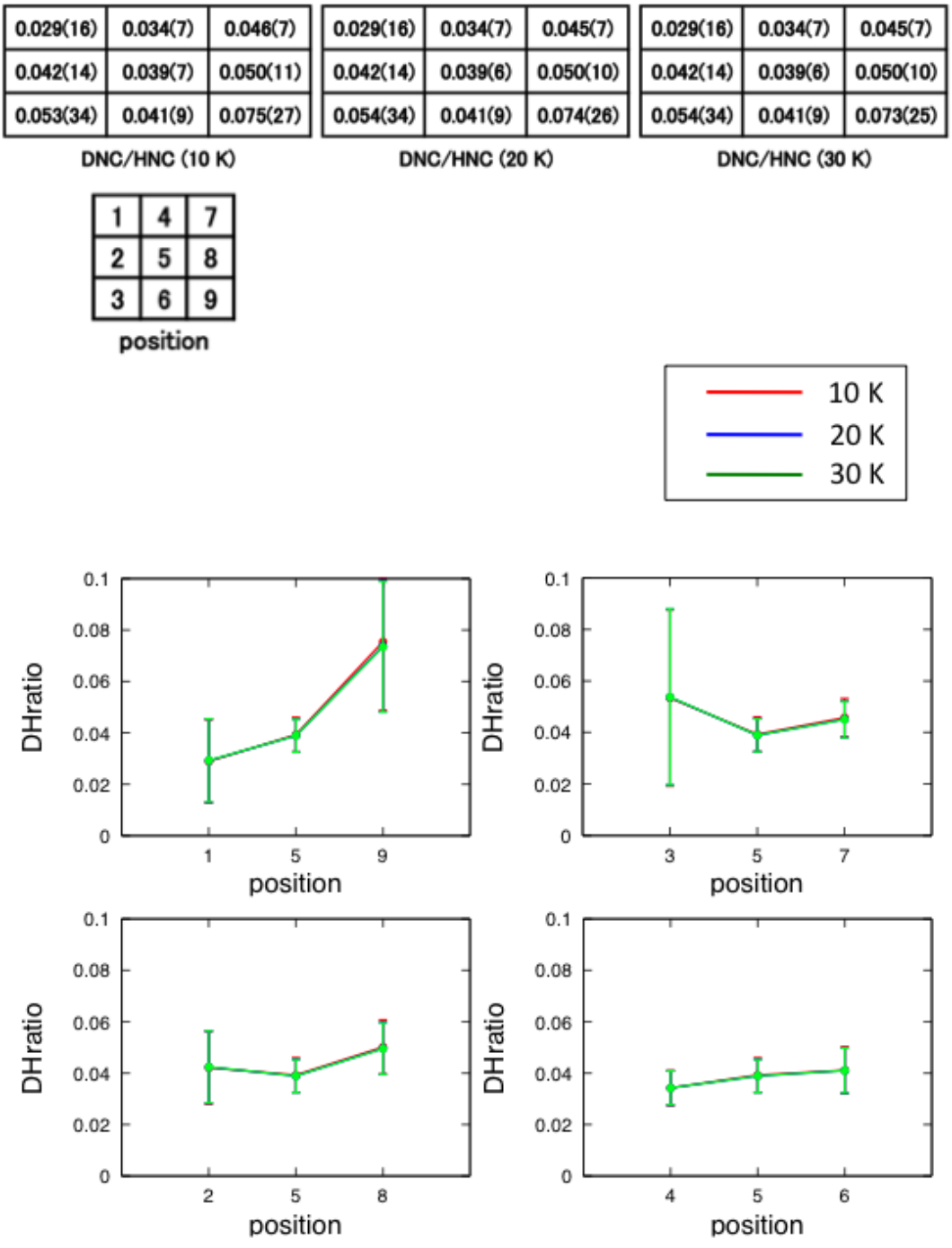

Figure 4.11: The deuterium fractionation ratio toward NGC1333-IRAS2A. The numbers in parentheses represent three times the standard deviation (3σ) in units of the best significant digits.

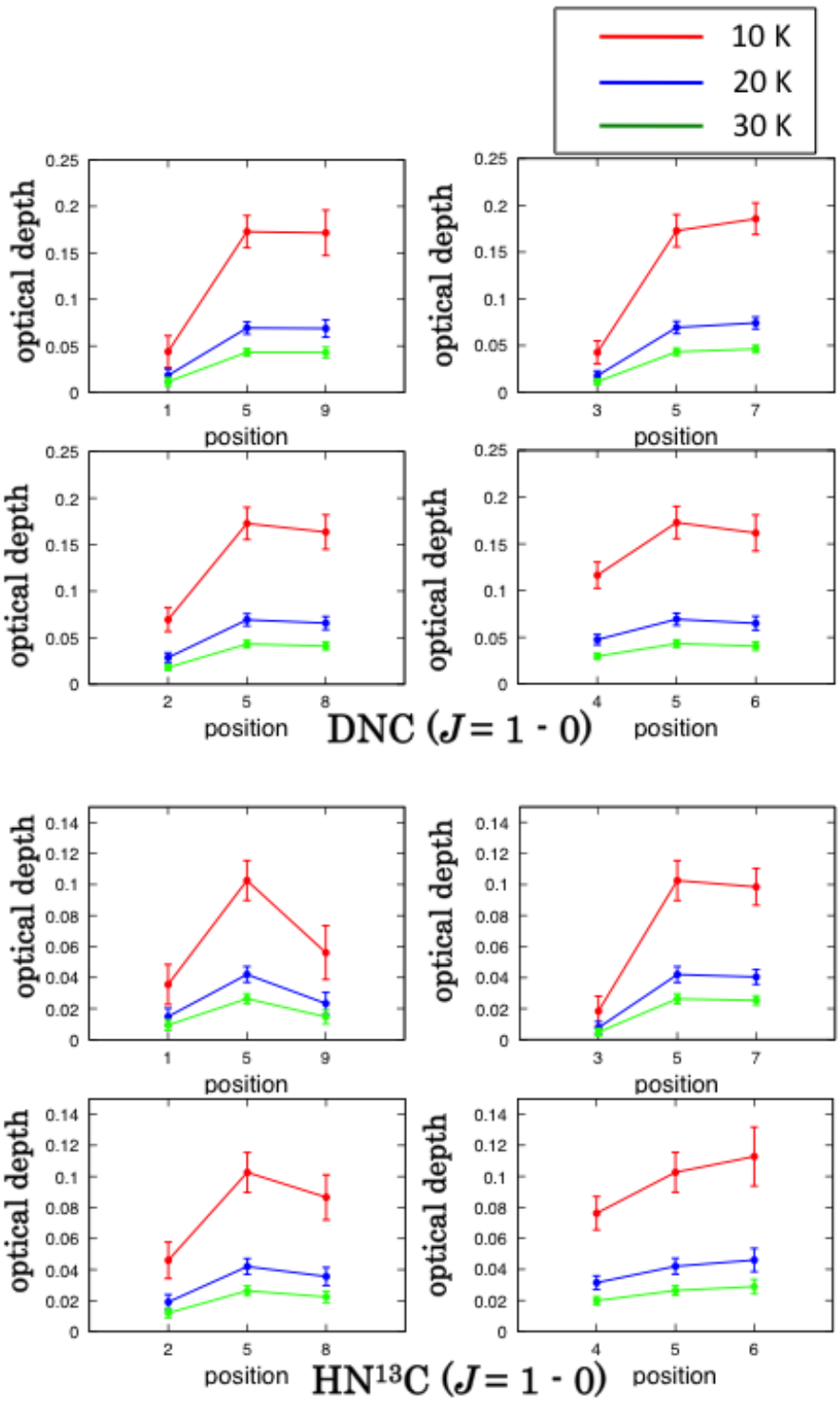

Figure 4.12: The optical depth toward NGC1333-IRAS2A. We show 3σ value for the error.

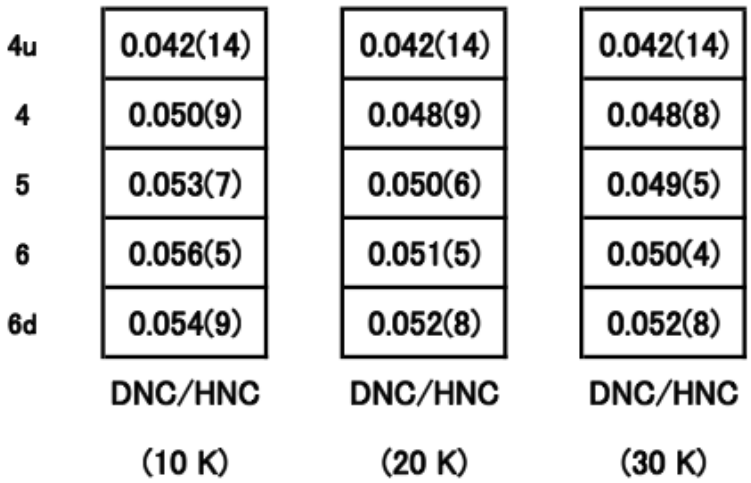

Figure 4.13: The deuterium fractionation ratio toward IRAS16293-2422. The numbers in parentheses represent three times the standard deviation (3σ) in units of the best significant digits.

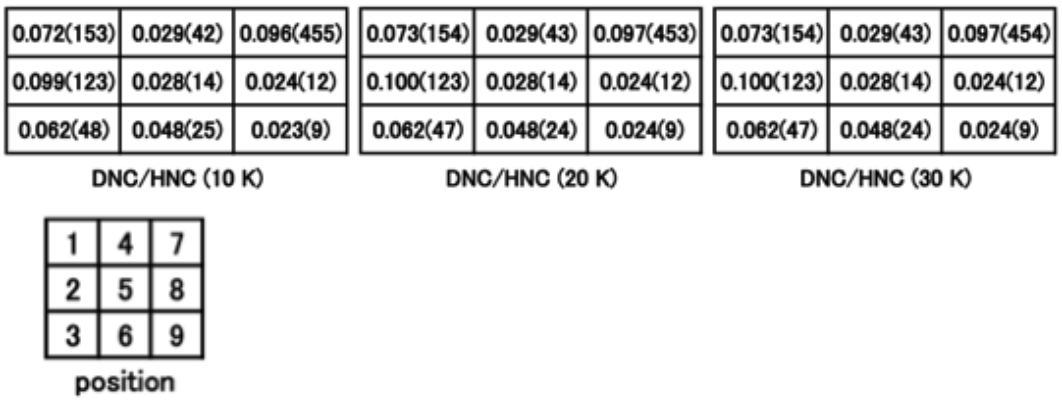

Figure 4.14: The deuterium fractionation ratio toward L1251A. The numbers in parentheses represent three times the standard deviation (3σ) in units of the best significant digits.

Chapter 5

Comparison between the ionic species and the neutral species

5.1 Dip trend

In previous chapters, we have examined how the deuterium fractionation ratio is affected around the protostar for each source. In table 5.1, we summarize the results. It is found that the behaviors of the ionic species and neutral species are different among the sources.

	Class	ionic species		neutral species	
		DCO^+/HCO^+ (20 K)	N_2D^+/N_2H^+ (20 K)	DNC/HNC (20 K)	DCN/HCN (20 K)
L1551-IRS5	Class I	○	○	×	
L483	Class I/0	○		×	**gradient**
NGC1333-IRAS2A	Class 0	**gradient**		×	
IRAS16293-2422	Class 0	×	×	×	
L1251A	Class I	×		×	

○ : low at the protostar position
gardient : There exist gradient
× : not low at the protostar position

Table 5.1: The results of the previous sections.

Here, we introduce a new parameter, dip depth D, to estimate the behavior of the each deuterium fractionation ratio in a quantitative way. The deuterium fractionation ratio at the protostar position is denoted as $R_{\rm in}$, while the average deuterium fractionation ratio of the

surrounding positions is represented as $R_{\rm out}$ (figure 5.1). Then, we define the dip depth D as following equation:

$$D \equiv \frac{R_{\rm out} - R_{\rm in}}{R_{\rm out}}. \tag{5.1}$$

The dip depth means how strongly the deuterium fractionation ratio at the protostar position is decreased in comparison with the surrounding positions, and we can be used to evaluate the degree of the dip without being influenced by the gradient over the cloud. Namely, $D > 0$ means existence of the dip, $D = 0$ means smooth distribution over the cloud, and $D < 0$ means enhancement toward the protostar position. If the deuterium fractionation ratio is decreased at the protostar position, the dip depth will be $D > 0$. If the deuterium fractionation ratio does not decrease, the dip depth will be $D < 0$.

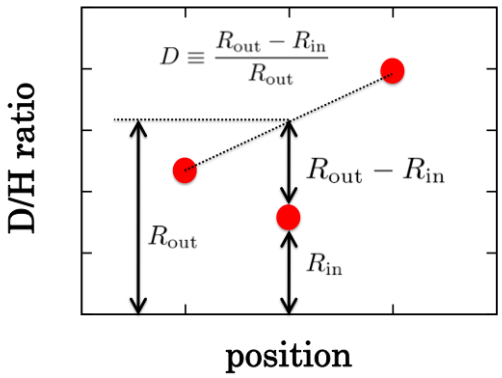

Figure 5.1: The dip depth.

We calculated the dip depth D of the deuterium fractionation ratios of DCO^+/HCO^+, N_2D^+/N_2H^+, DNC/HNC and DCN/HCN for each source. The results are shown in table 5.2. We show the dip depth in red if it is larger than 0 for ionic species, and also show it in blue if it is larger than 0 for the neutral species. Toward L1551-IRS5, all D of the ionic species are larger than 0. On the other hand, the dip depth of the neutral species is almost 0 in the direction of 4, 5 and 6. Both DNC and $HN^{13}C$ lines at position 3 are weak, so the error of the dip depth of the direction 3, 5 and 7 is large. The deuterium fractionation ratios of the ionic species, DCO^+ and N_2D^+, tend to decrease toward the protostar position, while the DNC/HNC ratio does not seem to be low at the protostar position. There seems to be the difference between the deuterium fractionation ratios of the ionic species and neutral

species toward L1551-IRS5, L483 and NGC1333-IRAS2A, although the dip depth of the DCO^+/HCO^+ ratio in the disk direction is not larger than 0 toward NGC1333-IRAS2A.

For IRAS16293-2422, the dip depth of DCO^+/HCO^+ is significantly higher than 0, if we consider only central three positions (positions 4, 5 and 6). The dip depth is larger than 0 considering all five position but the error becomes larger. On the other hand, the dip depth of the deuterium fractionation ratio DNC/HNC is almost 0.

The errors of the dip depth are larger than those of the other protostars toward L1251A. It is difficult to examine from the dip depth.

As shown in the previous sections, the optical depth effect is taken into account by using equations (3.4) and (3.5) at least for the first order. The dip of DCO^+/HCO^+ ratio observed in L1551-IRS5 and L483 is not due to the saturation effect of the DCO^+ line. Here, we consider the effect of the optical depth more carefully. In paticular, the optical depths of DCO^+ and $H^{13}CO^+$ are relatively high toward L1551-IRS5 and L483, and hence, it is worth examing the self absorption effect. Figure 5.2 compares the spectral line profiles of $H^{13}CO^+$ and $HC^{18}O^+$ toward L483. The spectral line profiles are almost identical. Therefore, it is most likely that $H^{13}CO^+$ does not affected by self absorption. Moreover, we calculated dip depth by assuming the same excitation temperature for all nine positions. The exciation temperature of the central protostar position is expected to be higher toward the protostar position than that toward the ambient eight positions. Hence, the optical depth of the protostar position will be lower than that of the ambient positions due to higher excitation temperature: the optical depth of the protostar position assuming the excitation temperature of 20 K is smaller than that assuming the exication temperature of 10 K. Even if DCO^+ affected by the self absorption, this effect will be higher at the ambient positions than the protostar position. For these reasons, our conclusion of the existence of the dip toward the protostar position is robust regardless of the assumption of the same excitation temperature for all the positions.

Here, we briefly discuss the effect of the beam width of the telescope on the distribution of the deuterium fractionation ratio. Although our observations were done with the grid spacing comparable to the beam size, the contamination of the other positions is unavoidable. Quantitative estimation of this effect is difficult, because it requires the accurate intensity distribution and the accurate beam pattern: the former is not available in our case. However, the contamination tends to smear the dip structure, but it does not artificially make it. Hence, the observed dip structure should be real, even if we consider the beam width effect.

sources	direction	ionic species		neutral species	
		DCO^+/HCO^+ (20 K)	N_2D^+/N_2H^+ (20 K)	DNC/HNC (20 K)	DCN/HCN (20 K)
L1551-IRS5	total	0.4(3)	0.6(3)	0.4(5)	
	1, 5, 9	0.6(3)		0.4(3)	
	2, 5, 8	0.4(3)	0.7(3)	0.5(5)	
	3, 5, 7	0.4(3)		0.5(10)	
	4, 5, 6	0.3(2)	0.4(2)	0.02(16)	
L483	total	0.23(14)		−0.10(13)	0.07(14)
	1, 5, 9	0.26(14)		−0.14(12)	0.06(13)
	2, 5, 8	0.17(13)		−0.09(12)	0.05(13)
	3, 5, 7	0.23(17)		−0.14(15)	0.03(19)
	4, 5, 6	0.25(13)		−0.04(12)	0.15(14)
NGC1333-IRAS2A	total	0.3(3)		0.2(4)	
	1, 5, 9	0.3(3)		0.2(4)	
	2, 5, 8	0.4(2)		0.2(3)	
	3, 5, 7	0.3(3)		0.2(5)	
	4, 5, 6	0.1(3)		0.0(3)	
IRAS16293-2422	total	0.2(3)	−0.04(14)	0.0(2)	
	4, 5, 6	0.2(2)	0.09(13)	0.00(17)	
L1251A	total	0.1(5)		1(2)	
	1, 5, 9	0.0(5)		0.4(19)	
	2, 5, 8	0.1(4)		0.6(13)	
	3, 5, 7	0.0(5)		1(4)	
	4, 5, 6	0.1(4)		0.3(10)	

Table 5.2: The dip depth of each source. The numbers in parentheses represent three times the standard deviation (3σ) in units of the best significant digits.

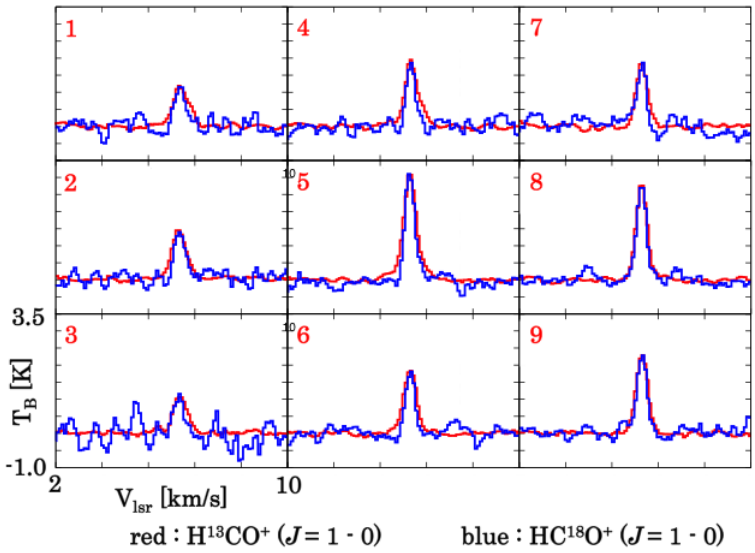

Figure 5.2: The spectra of $H^{13}CO^+$ and $HC^{18}O^+$ toward L483. The red spectra show $H^{13}CO^+$ and the blue spectra show $HC^{18}O^+$.

5.2 Destruction timescale and the dynamical age

The above results can be interpreted by considering destruction process of the deuterated species. Deuterium fractionation ratios will be the highest at the end of the starless core phase, and will decrease after the onset of star formation. They approach to new equilibrium ratios at higher temperatures. This decrease of the deuterium fractionation ratios mainly originated from destruction of the deuterated molecules produced in the cold starless core. Hence, the difference of the behavior between the deuterium fractionation ratios of the ionic species and neutral species may be ascribed to the different destruction mechanisms.

DCO^+ is mainly destructed by the dissociative recombination reaction with electron:

$$DCO^+ + e \longrightarrow D + CO. \tag{5.2}$$

The rate of this reaction is $k = 1.55 \times 10^{-6}$ $cm^3 s^{-1}$ at 20 K (the UMIST database http://udfa.ajmarkwick.net/) , and the time scale of this reaction is

$$t = \frac{1}{k_r[e]} \simeq 10^9 \text{ s} \simeq 100 \text{ yr}. \tag{5.3}$$

Thus, DCO^+ is rapidly destructed after the protostar is formed. For the above reason, the deuterium fractionation ratios of DCO^+/HCO^+ becomes low around the protostar. Moreover, once a protostar is formed and the ambient gas temperature reaches at 20 K, CO is evaporated from dust grains. Then, the following reaction:

$$N_2D^+ + CO \longrightarrow DCO^+ + N_2 \tag{5.4}$$

will be occur. The rate coefficient of this reaction is 8.8×10^{-10} s^{-1} (Millar et al. 1997), and the timescale of this destruction is shorter than 1 year. Hence, N_2D^+ around the protostar becomes deficient. On the other hands, the neutral species DNC and DCN is destructed by the following ionic destruction reactions:

$$DNC + He^+ \longrightarrow CN^+ + He + D \tag{5.5}$$
$$DNC + He^+ \longrightarrow N^+ + CD + He \tag{5.6}$$
$$DNC + He^+ \longrightarrow N + C^+ + He + D \tag{5.7}$$
$$DNC + He^+ \longrightarrow N + CD^+ + He. \tag{5.8}$$
$$DCN + He^+ \longrightarrow CN^+ + He + D \tag{5.9}$$
$$DCN + He^+ \longrightarrow N^+ + CD + He \tag{5.10}$$
$$DCN + He^+ \longrightarrow N + C^+ + He + D \tag{5.11}$$
$$DCN + He^+ \longrightarrow N + CD^+ + He. \tag{5.12}$$

The timescale of these reactions are about 10^4 - 10^5 year.

The model calculation of these destruction timescale is also conducted by Sakai et al. (2012). They considered the situation that the temperature raise at the age of 1×10^5 year and 3×10^5 year, and showed the variation of the DNC/HNC ratio and the N_2D^+/N_2H^+ ratio. Figure 5.3 shows the result. The N_2D^+/N_2H^+ ratio rapidly decreases after the temperature raise, whereas the DNC/HNC ratio gradually decreases with about 10^4 years after the temperature raises to 30 K.

The normal species are also destructed by the similar reactions. However, normal species does not decrease, because H_3^+, which is the resource of the normal species, abundantly exists in molecular clouds and does not decrease. On the other hand, H_2D^+, which is the resource of the deuterated species, decreases by the reason mentioned in Section 1.3.

For these reasons, the difference between the deuterium fractionation ratios of the

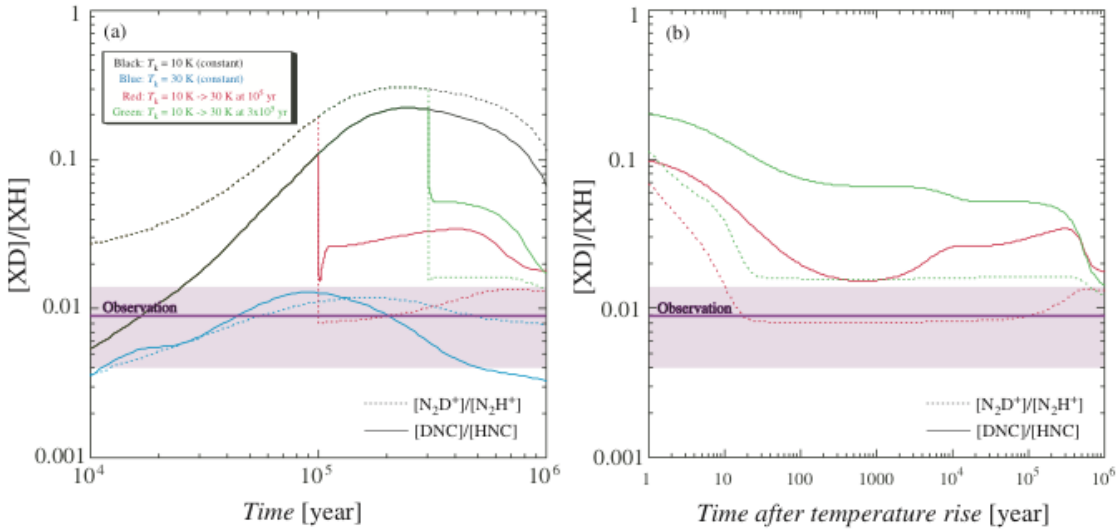

Figure 5.3: The model calculation conducted by Sakai et al. (2012). The solid line shows the DNC/HNC ratio and the dotted line shows the N_2D^+/N_2H^+ ratio. The red line shows the temperature rises at 10^5 year, and green shows that at 3×10^5 year. (Sakai et al., ApJ, 747, 140, 2012, ©AAS. Reproduced with permission.)

ionic species and neutral species would be expected. Indeed, the DCO^+/HCO^+ ratio and N_2D^+/N_2H^+ ratio toward L1551-IRS5 and the DCO^+/HCO^+ ratio toward L483 and NGC1333-IRAS2A decrease at the protostar position.

Table 5.3 shows the evolutionary stage and the dynamical age of CO outflow of each protostar. The dynamical age of outflow can roughly be regarded as the age of the protostar. The dynamical ages of each protostar are comparable to the destruction timescale of the neutral deuterated species. Hence, clear decrease of the DNC/HNC ratio is not seen at the protostar position, although the DCO^+/HCO^+ ratio is decreased.

sources	Class	dynamical age	reference
L1551-IRS5	Class I	$(3-10) \times 10^4$	Momose et al. 1998
L483	Class I/0	1.2×10^4	Dunham et al. 2014
NGC1333-IRAS2A	Class 0	$(5.7-12) \times 10^3$	Knee et al. 2000
IRAS16293-2422	Class 0	$(6-9) \times 10^3$	Mizuno et al. 1990
L1251A	Class I	$(9.2-18) \times 10^4$	Sato et al. 1994

Table 5.3: The dynamical timescale of each source.

5.3 The sizes of the warm region

The deuterium fractionation ratios are considered to change where the temperature is raised above 20 K due to the protostar formation. Then, we consider about the temperature structure of each source.

According to Terebey et al. (1993), the relationship between the dust temperature $T_{\rm dust}$ and the radius r is written as the following equation :

$$T_{\rm dust}(r) = T_0 \left(\frac{r}{r_0}\right)^{-q} \left(\frac{L}{L_0}\right)^{q/2}, \tag{5.13}$$

where T_0 is the dust temperature at the fiducial radius r_0 when the central luminosity is L_0. Here, q depends on the dust property and is expressed by the following equation:

$$q = \frac{2}{4+\beta}. \tag{5.14}$$

β is the emissivity and generally takes the value ranging from 1 to 2. Hence, q ranges from 0.33 to 0.4.

Generally, the dust is optically thick for the UV rays, the visible rays and the near-infrared wave near the central core. Then, the equation (5.13) is usable for the optically thin outer region. The value of T_0 exactly depends on the effect of the radiative transfer at the inner optical thick region. The detail calculations of the radiative transfer were conducted toward various sources so far. Butner et al. (1990) calculated the radiative transfer toward the bright source, NGC2071. According to their calculation, it was determined that the dust temperature $T_{\rm dust}$ is proportional to $r^{-0.4}$.

Now, we use the value of β as 2. As the fiducial value, we conducted r_0 = 100 AU, T_0 = 38 K for the luminosity 1 $L_\odot$ (Fridlund et al. 2002). Then, the equation (5.15) is rewritten as:

$$T_{\rm dust}(r) = 38\ {\rm K} \left(\frac{r}{100\ {\rm AU}}\right)^{-0.4} \left(\frac{L}{1L_\odot}\right)^{0.2}. \tag{5.15}$$

Here, we assume the dust temperature and the gas temperature are the same.

We calculated the size of the 20 K region where the deuterium fractionation is considered to change by using the luminosity of each protostar (Motte et al. 2001; Emprechtinger et al. 2009; Shirley et al. 2000; Schöier et al. 2004; Jϕrgensen et al. 2004; Itziar et al. 2006) by

use of equation (5.15). Table 5.4 shows the result. In table 5.4 also shows simultaneously the apparent size. The spatial resolution of the Nobeyama 45 m telescope is about 20″ at 70 to 80 GHz band, and that of the ASTE 10 m telescope is 22″. Table 5.4 shows that even L1251A whose 20 K region is the smallest covers about 75 % of the beam of Nobeyama 45 m telescope. For this reason, the results shown before reflect warm region above 20 K around the protostar position.

	Luminosity	distance	$T > 20$ K region (arcsecond)
L1551-IRS5	28 $L_\odot$	140 pc	5266 AU (37.6 ″)
L483	13 $L_\odot$	200 pc	3588 AU (17.9 ″)
IRAS16293-2422	27 $L_\odot$	160 pc	5171 AU (32.3 ″)
NGC1333-IRAS2A	16 $L_\odot$	220 pc	3981 AU (18.1 ″)
L1251A	27 $L_\odot$	300 pc	5171 AU (17.2 ″)

Table 5.4: The regions whose temperature is over 20 K.

5.4 The effect of the envelope

We cannot see the clear decrease of the DCO^+/HCO^+ ratio and the N_2D^+/N_2H^+ ratio at the protostar position toward IRAS16293-2422. IRAS16293-2422 is classified in Class 0 protostar. In this stage, there exists much cold envelope gas around the protostar. For this reason, the results seems to strongly affected by a cold ambient envelope in observations of the low excitation lines.

Here, we consider the effect of the outer envelope on the observational results. The observational results may be affected by the outer envelope, because we observed the low excitation lines with the Nobeyama 45 m telescope. In fact, we could not clearly see decrease of the DCO^+/HCO^+ ratios, which are considered to decrease rapidly by the temperature rise, at the protostar positions toward IRAS16293-2422, NGC1333-IRAS2A and L1251A.

The envelope radius are shown in table 5.5. Jϕrgensen et al. (2002) and Schöier et al. (2002) calculated the physical structure of the envelope from spectral energy distribution. They calculated the region where the temperature rised at 10 K as the characteristic size of the envelope. Table 5.5 shows that the radius of the 10 K region of the Class I protostar, L1551-IRS5, is larger. However, this is due to the high luminosity of the protostar, and does not mean rich envelope gas. The column density of H_2 at the 10 K region of L1551-

IRS5 is rather smaller than those of the other protostars. Hence, contribution of the cold envelope to the observation would relatively be small toward L1551-IRS5. On the other hand, the column density of H_2 at the 10 K region of IRAS16293-2422 is one order larger than the other protostars. Moreover, the envelope mass $M_{10\ \mathrm{K}}$ of IRAS16293-2422 shows that IRAS16293-2422 has the massive envelope (table 5.5). For this reason, the decrease of the DCO^+/HCO^+ ratio at the protostar position can not observed due to overwhelming contribution of the envelope, though IRAS16293-2422 is bright and the size of the 20 K region of this protostar is large.

The actual size of the outer envelope is still uncertain, and the effect of the envelope can only be considered by some parameters. Hence, it is difficult to estimate quantitatively the effect of the envelope. However, the observational results toward different protostars can be explained on the basis of the difference of the column density of H_2 and the envelope mass.

sources	Class	$r_{10\ \mathrm{K}}$ [AU]	r_{out}	$N_{\mathrm{H_2},10\ \mathrm{K}}$	$M_{10\ \mathrm{K}}$
L1551-IRS5	Class I	1.6×10^4	2.5×10^4	3.8×10^{23}	1.7 $M_\odot$
L483	Class I/0	0.78×10^4	3.2×10^4	9.3×10^{23}	1.1 $M_\odot$
IRAS16293-2422	Class 0	0.80×10^4		16×10^{23}	5.4 $M_\odot$
NGC1333-IRAS2A	Class 0	1.2×10^4	2.1×10^4	5.5×10^{23}	1.7 $M_\odot$
L1251A	Class I				

Table 5.5: The evolutionary stages and the radius of the envelope of the observed protostars (Jørgensen et al. 2002, Schöier et al 2002).

The effect of the envelope may be seen when we look at the spectra toward the protostar position carefully. The spectral line of $H^{13}CO^+$ is slightly broader than that of DCO^+ toward the protostar position, as shown in table 5.6. The exceptions are L1551-IRS5 observed with the Nobeyama 45 m telescope and IRAS16293-2422 observed with the ASTE telescope. In figures 5.4 to 5.7, we show the difference spectra between $H^{13}CO^+$ and DCO^+ at the protostar position observed with the Nobeyama 45 m telescope and with the ASTE 10 m telescope. Here, we scale the peak intensity of the normal species to that of the deuterated species for comparison with the velocity feature. The DCO^+ line has the hyperfine structure of deuterium, and the line width of DCO^+ line may be wider than that of the $H^{13}CO^+$ line. Nevertheless, the difference spectrum toward L483 (figure 5.4) with the Nobeyama 45 m telescope shows negative feature in $v = 3.5 - 5$ km/s and $v = 6$ km/s. This means that the line width of DCO^+ is narrower than that of $H^{13}CO^+$. The similar features are also seen in the spectra toward NGC1333-IRAS2A, IRAS16293-2422 and L1251A observed with the

	Nobeyama 45 m telescope		ASTE 10 m telescope	
sources	DCO^+ (J = 1 − 0)	$H13CO^+$ (J = 1 − 0)	DCO^+ (J = 5 − 4)	$H13CO^+$ (J = 4 − 3)
L483	0.685(14)	0.685(11)	0.44(4)	0.87(6)
NGC1333-IRAS2A	0.86(3)	1.17(3)	0.84(3)	0.905(16)
IRAS16293-2422	0.99(4)	1.55(3)	2.25(11)	2.67(7)
NGC1333-IRAS2A	0.63(4)	1.12(5)		
L1551-IRS5	0.93(5)	0.813(16)		

Table 5.6: The line width of each source toward protostar position.

Nobeyama 45 m telescope, and toward L483, IRAS16293-2422 observed with the ASTE 10 m telescope.

In particular, this effect is particularly significant in IRAS16293-2422. This indicates that the DCO^+/HCO^+ ratio differs between the systemic velocity (narrow) component and the broad component. Apparently the DCO^+/HCO^+ ratio is much lower in the broad component. As schematically shown in figure 5.4, the velocity of the gas envelope would become faster for close to the protostar due to increasing infalling and rotating motion. Hence, the low DCO^+/HCO^+ ratio of the broad component implies that the DCO^+/HCO^+ ratio indeed decreases in the vicinity of the protostar.

To see this effect more in detail, interferometer observations are useful. We hence analysed the archival data of SMA. We show the spectra and channel maps of DCO^+, N_2D^+ and $H^{13}CO^+$ obtained by the analysis of the archival data of SMA in figure 5.8, 5.9, 5.10 and 5.11. Each spectra shown in figure 5.8 are the spectra averaged over $20'' \times 20''$ region around the protostar. The spectrum of $H^{13}CO^+$ is significantly wider than those of DCO^+ and N_2D^+. Since the envelope component extended, it is resolved out significantly in the interferometer observations. On the other hand, the compact component around the protostar is not resolved out. Hence, the difference between DCO^+ and $H^{13}CO^+$ line width is seen more clearly. As shown in table 5.7, the deuterium fractionation ratio DCO^+/HCO^+ is higher at the systemic velocity. This result support our interpretation.

Furthermore, a difference between ionic deuterated species and neutral deuterated species can be seen by the distribution obtained by the interferometer. Figure 5.12 shows the distributions of the deuterated species obtained from the analysis of the archival data of SMA. The neutral deuterated species are concentrated around the protostar. On the other hand, the ionic deuterated species does not exist near the protostar position and exist at the position away

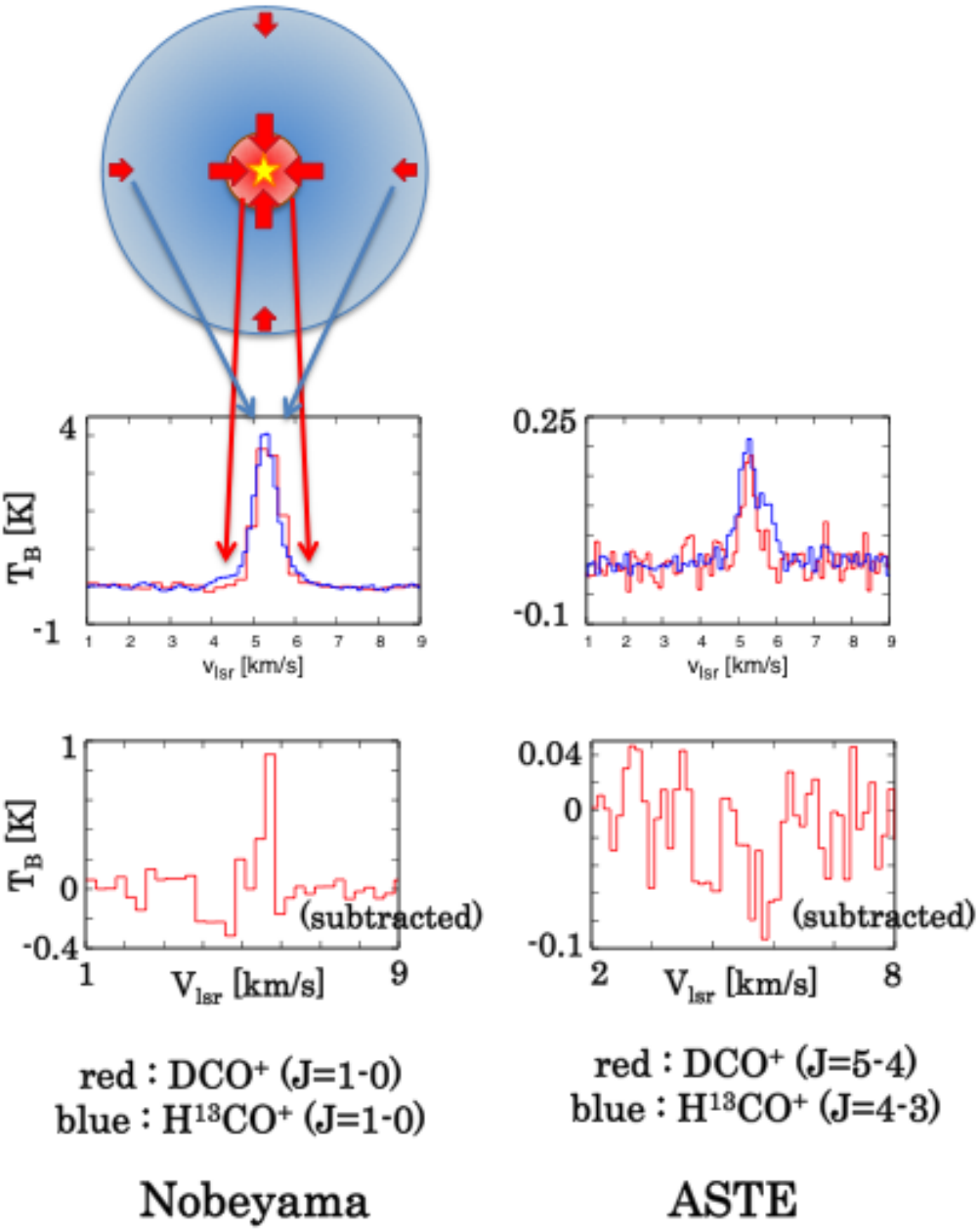

Figure 5.4: The spectra toward the protostar position of L483.

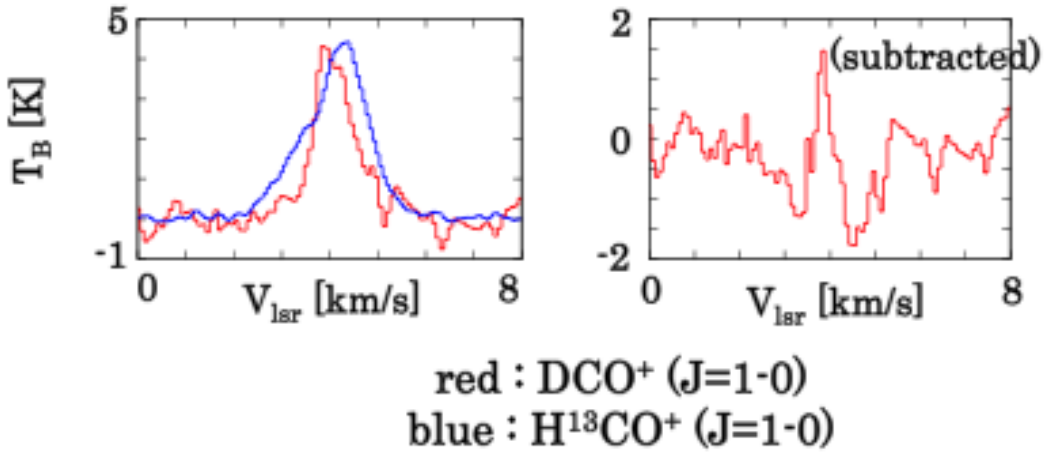

Figure 5.5: The spectra toward the protostar position of IRAS16293-2422.

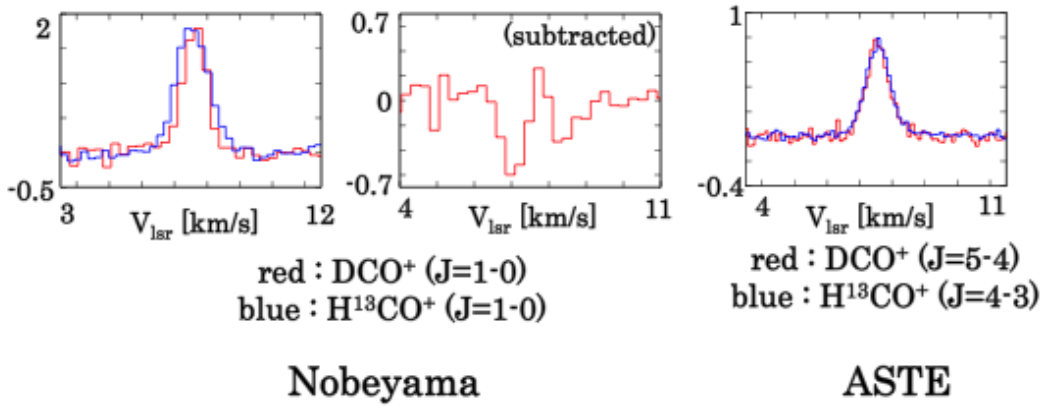

Figure 5.6: The spectra toward the protostar position of NGC1333-IRAS2A.

	DCO^+/HCO^+ (10 K)	DCO^+/HCO^+ (20 K)	DCO^+/HCO^+ (30 K)
v = 4.3 km/s	0.014(4)	0.032(10)	0.043(13)
v = 3 km/s	$<$ 0.005	$<$ 0.013	$<$ 0.015

Table 5.7: The DCO^+/HCO^+ ratios of v = 4.3 km/s and v = 3 km/s. The numbers in parentheses represent three times the standard deviation (3σ) in units of the best significant digits.

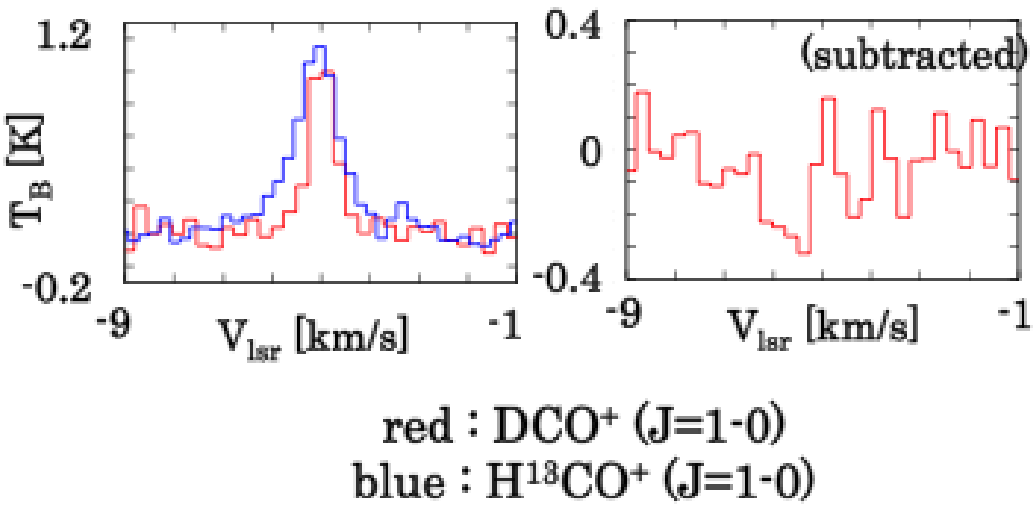

Figure 5.7: The spectra toward the protostar position of L1251A.

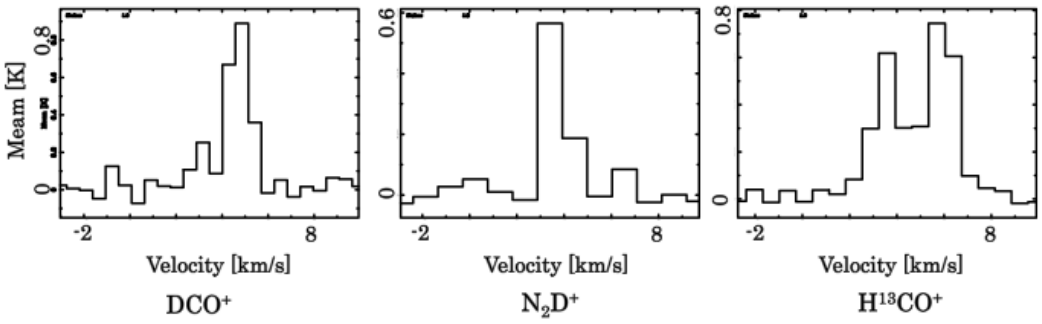

Figure 5.8: The spectra toward IRAS16293-2422 obtained by the analysis of the archival data of The Submillimeter Array.

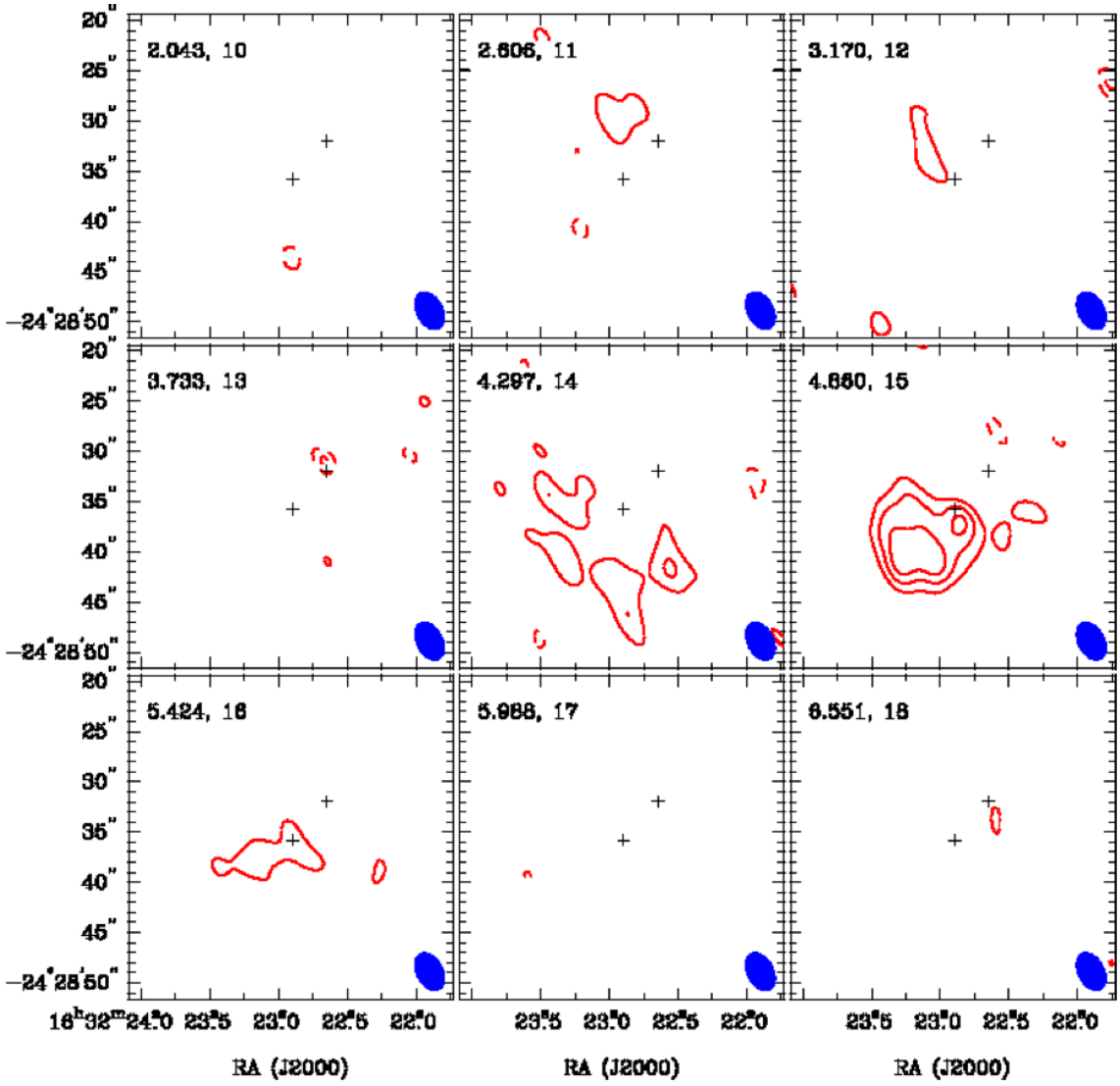

Figure 5.9: Channel map of DCO^+ toward IRAS16293-2422 obtained from the SMA archival data.

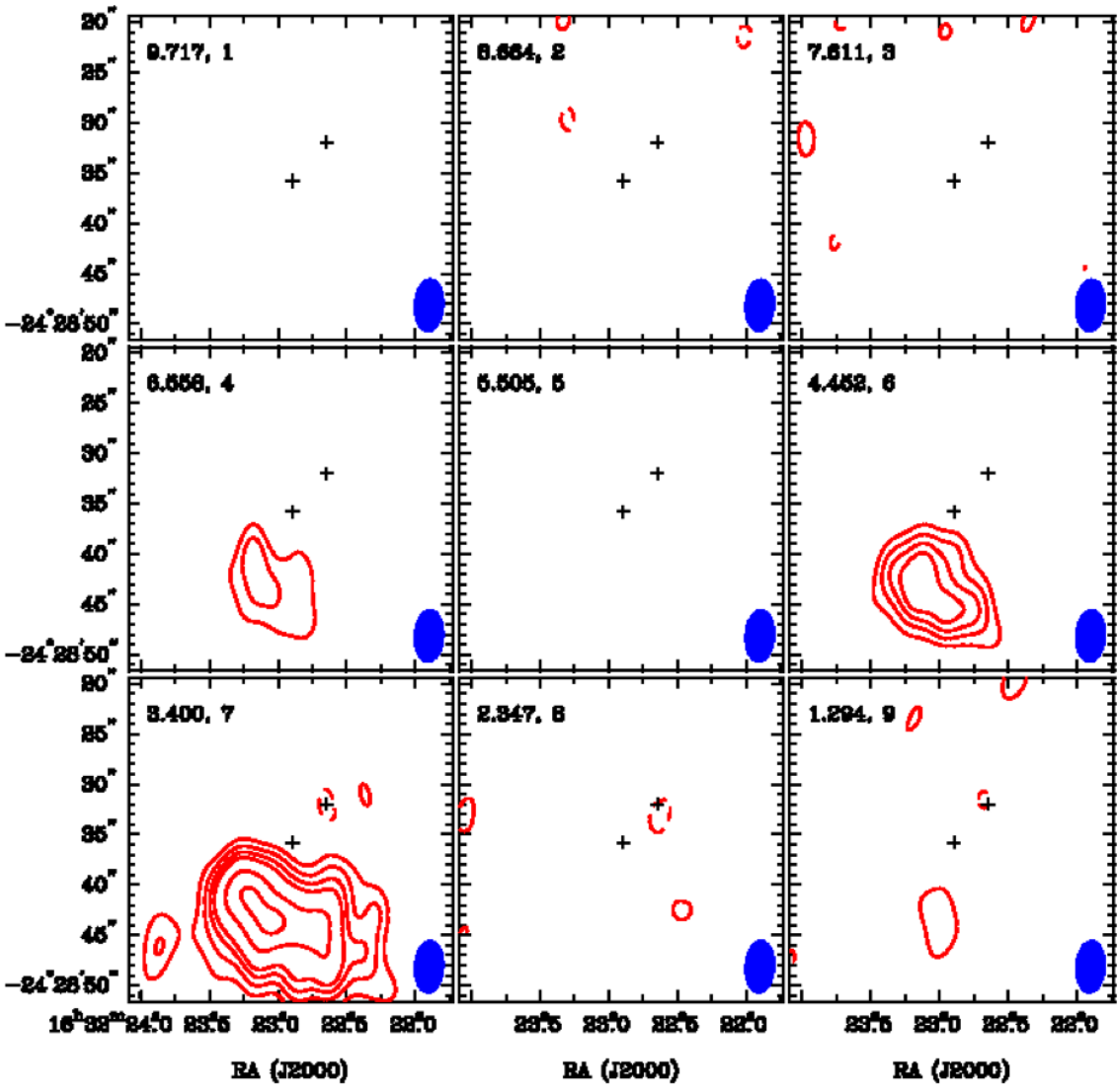

Figure 5.10: Channel map of N_2D^+ toward IRAS16293-2422 obtained from the SMA archival data.

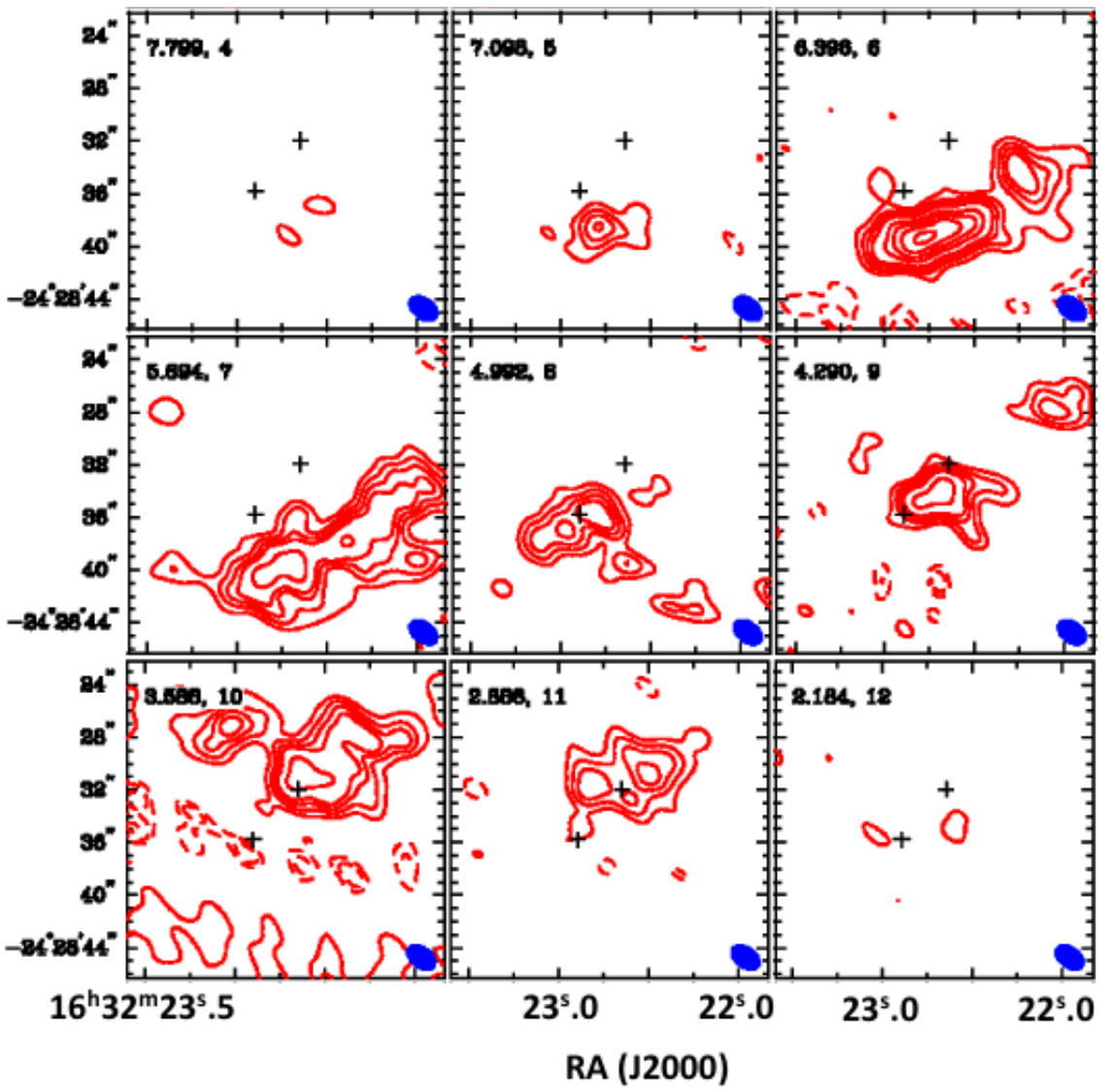

Figure 5.11: Channel map of $H^{13}CO^+$ toward IRAS16293-2422 obtained by SMA archival data.

from the protostar. This means that the neutral deuterated species does not still destructed around the protostar, whereas the ionic deuterated species already destructed.

5.5 The effect of the HNC destruction

Toward L483, we observed not only $HN^{13}C$ but also $H^{13}CN$. Then, we calculated HNC/HCN ratio and compared the distribution. Figure 5.13 shows the HNC/HCN ratios at the each position toward L483. We normalized each ratio by the ratio at the protostar position (position 5), and the red value means that the HNC/HCN ratio is larger than that at the protostar position. The HNC/HCN ratio shows gradient from east to west, namely the HNC/HCN ratios are low at the east positions and high at the west positions. The HNC/HCN ratio shows a dip at the protostar position. This means that HNC/HCN ratio shows the similar behavior as the deuterium fractionation ratio of the ionic species, DCO^+/HCO^+. It can be considered as follows.

HNC is the unstable molecule and preferentially exist only in the cold condition. When the temperature rises, HNC may be converted to HCN. The main reaction would be the following reaction:

$$\mathrm{HNC + H \longrightarrow HCN + H.} \tag{5.16}$$

The actibation energy barrier of this reaction is known to be 2000 K (Talbi et al. 1996). A recent value is 1200 K (Graninger et al. 2014).

Hirota et al. (1998) considered the following destruction and formation processes between HNC, HCN and $HCNH^+$:

$$\mathrm{HNC + H \longrightarrow HCN + H} \tag{5.17}$$
$$\mathrm{HNC + HX^+ \longrightarrow HCNH^+ + X} \tag{5.18}$$
$$\mathrm{HCN + HX^+ \longrightarrow HCNH^+ + X} \tag{5.19}$$
$$\mathrm{HCNH^+ + e \longrightarrow HNC + H} \tag{5.20}$$
$$\mathrm{HCNH^+ + e \longrightarrow HCN + H,} \tag{5.21}$$

and estimated that equation (5.16) becomes effective when the temperature reaches at 24 K. The size of the 24 K region toward L483 is 2275 AU (11.4″) calculated by the equation (5.15). This corresponds to about 32 % of the beam of the Nobeyama 45 m telescope. The

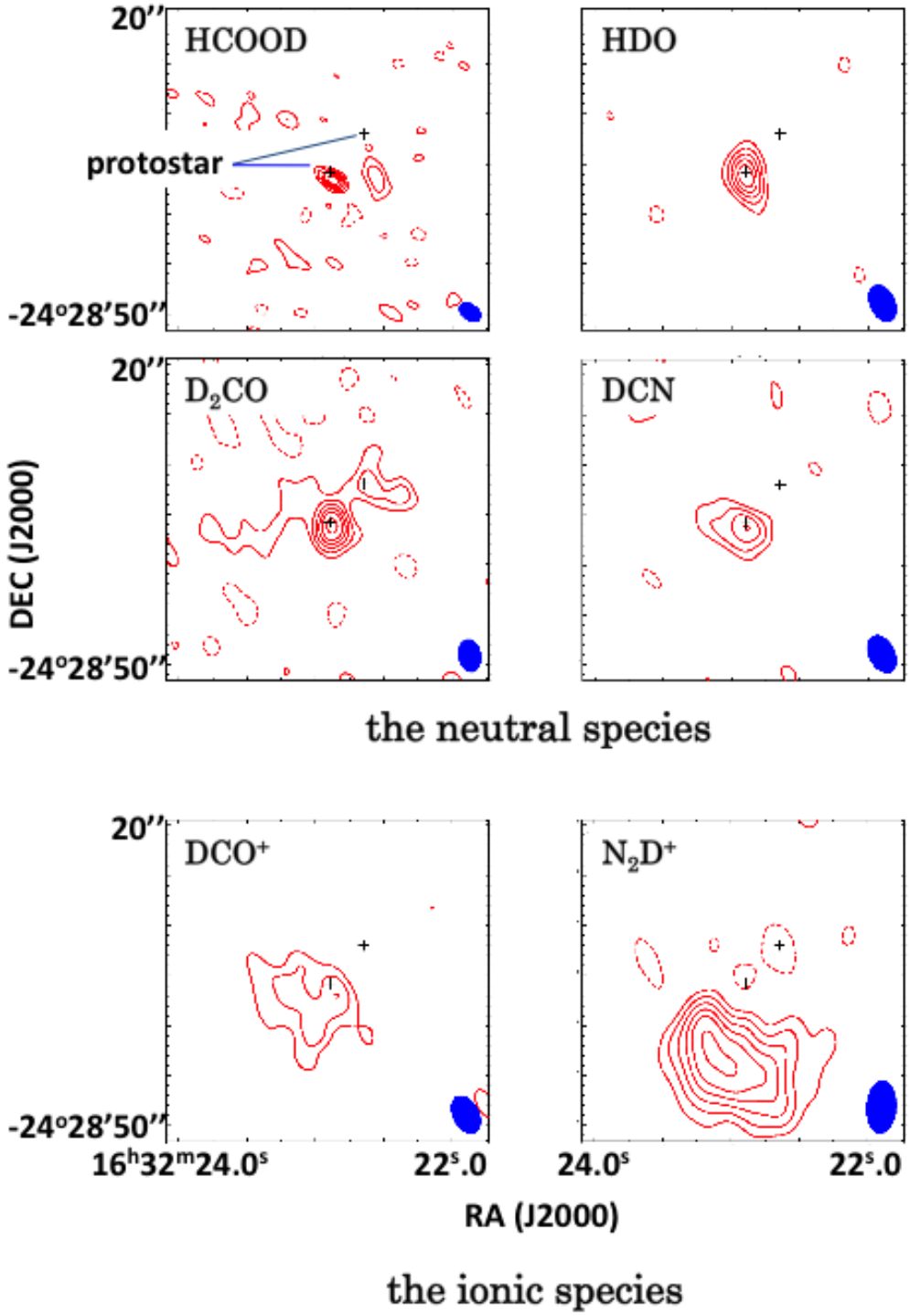

Figure 5.12: The distributions of the deuterated species toward IRAS16293-2422 obtained by the analysis of the archival data of The Submillimeter Array.

observational result toward the protostar position may traces the effect of the destruction of HNC to HCN. This means that we can trace the same phenomenon as the deuterium fractionation of the ionic species which changes by the temperature raise after birth of the protostar. If so, the HNC/HCN ratio will be a new tracer to explore the temperature structure in the vicinity of protostars.

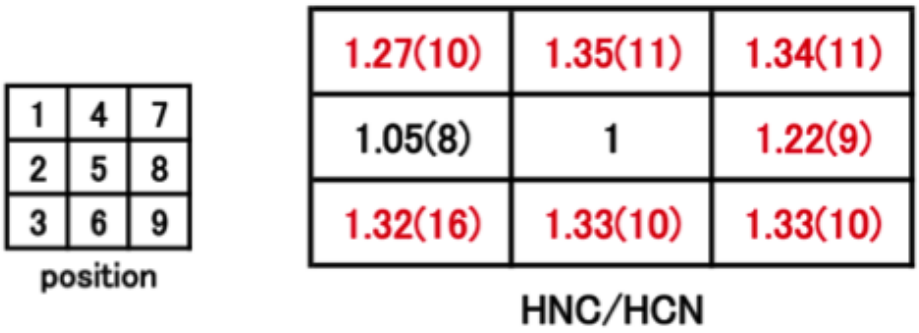

Figure 5.13: The HNC/HCN ratio normalized by the protostar position toward L483. The numbers in parentheses represent three times the standard deviation (3σ) in units of the best significant digits.

		total	1, 5, 9	2, 5, 8	3, 5, 7	4, 5, 6
L483	HNC/HCN (10 K)	0.22(8)	0.23(7)	0.12(7)	0.25(10)	0.25(7)
	HNC/HCN (20 K)	0.20(8)	0.22(7)	0.11(7)	0.23(10)	0.24(7)
	HNC/HCN (30 K)	0.20(8)	0.21(7)	0.11(7)	0.23(10)	0.24(7)

Table 5.8: The dip depth of the HNC/HCN ratios. The numbers in parentheses represent three times the standard deviation (3σ) in units of the best significant digits.

Chapter 6

Conclusion

6.1 Summary of this thesis

In this thesis, to examine the behavior of the deuterated species with the temperature raise by the protostar birth, we observed the deuterated species toward the low-mass star forming region L1551-IRS5, L483, IRAS16293-2422, NGC1333-IRAS2A and L1251A with the Nobeyama 45 m telescope and the ASTE 10 m telescope.

As a result, we found that the deuterium fractionation of DCO^+ and that of DNC show the different behavior toward L1551-IRS5, L483 and NGC1333-IRAS2A. The DCO^+/HCO^+ ratio decreases toward the protostar position. On the other hand, the DNC/HNC ratio does not show such a decrease toward the protostar position. The deuterated species are destructed by the temperature raise. The destruction timescale of DNC is 10^4 - 10^5 years, whereas DCO^+ is rapidly destructed after the protostar birth. Hence, the neutral deuterated species remains for a while after the protostar birth, and the ionic deuterated species is already destructed toward these protostars.

In contrast, for the other protostars, IRAS16293-2422 and L1251A, we could not see clear destruction of the ionic deuterated species and neutral deuterated species at the protostar position from the distribution of the deuterium fractionation ratio. IRAS16293-2422 is the young protostars classified in Class 0. Hence, the effect of the ambient envelope cannot be ignored. However, by comparing the spectra of DCO^+ and $H^{13}CO^+$ toward the protostar position, we could confirm the destruction of the ionic deuterated species for these protostars from the velocity structure. Moreover, by analysing the archival data of SMA, we can see the difference between the distributions of the neutral species and the ionic species toward

IRAS16293-2422.

For L483, we find the central decrease of the HNC/HCN ratio. The core itself has the gradient and the effect seems to appear to the HNC/HCN ratio. HNC seems to change to HCN by the temperature raise and HNC/HCN ratio at the protostar position becomes smaller than those at the ambient positions because of the destruction of HCN. This is the similar phenomenon as the deuterium fractionation of the ionic species.

Summarizing the above results, the deuterium fractionation ratio of the neutral species does not decrease at the protostar position toward L1551-IRS5, L483, NGC1333-IRAS2A, IRAS16293-2422. This means that the deuterium fractionation ratio of the neutral species preserves for a while after the protostar birth. Sakai et al. (2012) reported that the DNC/HNC ratio in the star forming region depends not only on the temperature and this ratio reflect the physical conditions just before the protostar birth from the observation of the DNC/HNC ratio toward the high-mass protostars. On the basis of chemical model calculation, the DNC/HNC ratio gradually decreases over 10^4 years. Our result gives an important support the expectation that the deuterium fractionation of the neutral species reflect the physical conditions just after the protostar birth. This could be a novel tracer to investigate past star formation processes.

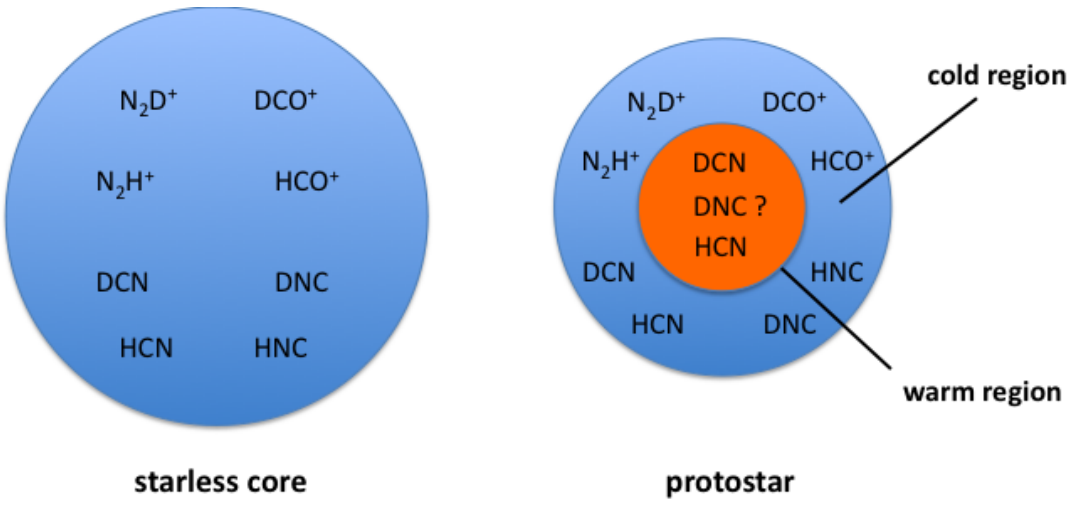

Figure 6.1: Schematical image of the deuterated species around the protostar.

6.2 Future prospects

We observed the behavior of the deuterated species with the single-dish telescope. For the next step, it is important to observe with more high resolution telescope and investigate directly the distributions of the deuterated species around the protostar. For this purpose, the observation with the interferometer is needed. In fact, the difference of the distribution can be seen in IRAS16293-2422. However, the deuterated species are the isotope and very weak. We also analyzed the archival data of SMA for the other protostars, but we could not get the decent distribution. Hence, the observation with the telescope whose sensitivity is better than SMA is strongly needed.

Appendix A

Detection equation

A.1 Radiative transfer equation

Spontaneous emission

The molecules in the interstellar molecular clouds spontaneously radiates. By the effect, the intensity of photon through the interstellar molecular clouds becomes strong. To explain quantitatively this amplification of the intensity, we define the emission coefficient j_ν as follows:

$$dE \equiv j_\nu dV d\Omega dt d\nu. \tag{A.1}$$

Here, dE denotes the variation of energy, dV the microvolume, $d\Omega$ the minute solid-angle, dt the minute time, and $d\nu$ the minute frequency. Then, the dimension of the emission coefficient is [cm^{-3} s^{-1} ster^{-1} Hz^{-1}]. Considering the photon proceeds the distance ds in the area of the cross section dA, then the energy variation becomes

$$dE = j_\nu dA ds d\Omega dt d\nu. \tag{A.2}$$

We define the specific intensity I_ν as:

$$dE \equiv dI_\nu dA dt d\Omega d\nu, \tag{A.3}$$

and then it can be explained as

$$dI_\nu = j_\nu ds. \tag{A.4}$$

Absorption

The photon passing through the interstellar molecular clouds will be absorbed by the various interstellar matters, and its intensity will be weak. To explain the effect of the decrease of the intensity, we define the absorption coefficient α_ν as follows:

$$dI_\nu \equiv -\alpha_\nu I_\nu ds. \tag{A.5}$$

Here, the dimension of the absorption coefficient is [cm^{-1}].

If the radiative process is only absorption, from the equation (A.5)

$$\frac{dI_\nu}{ds} = -\alpha_\nu I_\nu. \tag{A.6}$$

Then, I_ν is obtained as

$$I_\nu = I_\nu(0)\mathrm{e}^{-\alpha_\nu s}. \tag{A.7}$$

Radiative transfer equation

As one equation containing the above effects of both absorption and emission, we can define the following equation:

$$\frac{dI_\nu}{ds} = -\alpha_\nu I_\nu + j_\nu. \tag{A.8}$$

This equation is called the radiative transfer equation. Here, we define the optical depth τ as follows:

$$\tau_\nu \equiv \int_{s_0}^{s} \alpha_\nu(s')ds'. \tag{A.9}$$

The radiative transfer equation is written as follows:

$$\frac{dI_\nu}{d\tau_\nu} = I_\nu + S_\nu \tag{A.10}$$

by using the optical depth. Here, S_ν is called the source function.

We consider the situation that a photon which incomes at the distance $s = 0$ into molecular cloud comes out at the distance $s = \Delta s$. Then, the solution of the radiative transfer equation is obtained by:

$$I_\nu(\Delta s) = I_\nu(0)\exp\left[-\int_0^{\Delta s}\alpha_\nu(s')ds'\right] + \int_0^{\Delta s} ds' j_\nu(s')\exp\left[-\int_{s'}^{\Delta s}\alpha_\nu(s'')ds''\right]. \quad \text{(A.11)}$$

Here $I_\nu(0)$ denotes background emission. Moreover, assuming that molecular cloud is homogeneous and the absorption coefficient and the emission coefficient do not depend on the position, the solution of the radiative transfer equation is written as follows:

$$I_\nu(\Delta s) = I_\nu(0)\exp\left[-\alpha_\nu\Delta s\right] + \frac{j_\nu}{\alpha_\nu}\left(1 - \exp\left[-\alpha_\nu\Delta s\right]\right). \quad \text{(A.12)}$$

A.2 Einstein coefficient

We consider the two-level system, and write the upper level as k and the lower level as j. Here, we consider the emission and absorption deviding into spontaneous emission, absorption and stimulated emission. Here, Einstein coefficients are defined as follows:

$$A_{\rm kj} \equiv \text{the probability to transfer } k \to j \text{ by the spontaneous emission}[\mathrm{s}^{-1}] \quad \text{(A.13)}$$

$$B_{\rm jk}J \equiv \text{the probability to transfer } k \to j \text{ by the absorption} \quad \text{(A.14)}$$

$$B_{\rm kj}J \equiv \text{the probability to transfer } k \to j \text{ by the stimulated emission} \quad \text{(A.15)}$$

$$J \equiv \int_0^\infty J_\nu\phi(\nu)d\nu \quad \text{(A.16)}$$

J_ν denotes average intensity and $\phi(\nu)$ is the line profile function.

We rewrite the lower level as l and the upper level as u. The energy, abundance and statistical weight of each level is written as $E_{\rm l} = E$, $n_{\rm l}$, $g_{\rm l}$, $E_{\rm u} = E + h\nu_0$, $n_{\rm u}$ and $g_{\rm u}$. We assume the thermodynamic equilibrium. Here, the following relation is satisfied:

$$n_{\rm l}B_{\rm lu}J \equiv n_{\rm u}A_{\rm ul} + n_{\rm u}B_{\rm ul}J, \quad \text{(A.17)}$$

and

$$J = \frac{A_{\mathrm{ul}}/B_{\mathrm{ul}}}{\frac{n_{\mathrm{l}}}{n_{\mathrm{u}}}\frac{B_{\mathrm{lu}}}{B_{\mathrm{ul}}} - 1}. \tag{A.18}$$

On the other hand, considereing the canonical distribution, the ratio of the number density of each level is written as

$$\frac{n_{\mathrm{l}}}{n_{\mathrm{u}}} = \frac{g_{\mathrm{l}}\mathrm{e}^{-\frac{E}{kT}}}{g_{\mathrm{u}}\mathrm{e}^{-\frac{E+h\nu_0}{kT}}} = \frac{g_{\mathrm{l}}}{g_{\mathrm{u}}}\mathrm{e}^{\frac{h\nu_0}{kT}}, \tag{A.19}$$

and

$$J = \frac{A_{\mathrm{ul}}/B_{\mathrm{ul}}}{\frac{g_{\mathrm{l}}B_{\mathrm{lu}}}{g_{\mathrm{u}}B_{\mathrm{ul}}}\mathrm{e}^{\frac{h\nu_0}{kT}} - 1}. \tag{A.20}$$

Moreover, in the thermodynamic equilibrium, J_ν can be written with the Plank function B_ν as

$$B_\nu = \frac{2h\nu_0^3/c^2}{\mathrm{e}^{\frac{h\nu_0}{kT}} - 1}. \tag{A.21}$$

We can consider J_ν is constant because it is known emprically known that the Plank function is marginally change in the scale of the line width of the line profile function. Then, J is given by

$$J = J_\nu = B_\nu = \frac{2h\nu_0^3/c^2}{\mathrm{e}^{\frac{h\nu_0}{kT}} - 1}. \tag{A.22}$$

By the above equations (A.20) and (A.22), the following relation can be derived:

$$\frac{A_{\mathrm{ul}}/B_{\mathrm{ul}}}{\frac{g_{\mathrm{l}}B_{\mathrm{lu}}}{g_{\mathrm{u}}B_{\mathrm{ul}}}\mathrm{e}^{\frac{h\nu_0}{kT}} - 1} = \frac{2h\nu_0^3/c^2}{\mathrm{e}^{\frac{h\nu_0}{kT}} - 1}. \tag{A.23}$$

Then, the following relation between the Einstein coefficient is given:

$$\begin{aligned} g_{\mathrm{l}}B_{\mathrm{lu}} &= g_{\mathrm{u}}B_{\mathrm{ul}} \\ A_{\mathrm{ul}} &= \frac{2h\nu_0^3}{c^2}B_{\mathrm{ul}}. \end{aligned} \tag{A.24}$$

A.3 Detection equation

When we describe the transfer coefficient and the absorption coefficient with the Einstein coefficient, j_ν and α is written as

$$j_\nu = \frac{h\nu_c}{4\pi} n_u A_{ul} \phi(\nu) \tag{A.25}$$

$$\alpha_\nu = \frac{h\nu_c}{4\pi} (n_l B_{lu} - n_u B_{ul}) \phi(\nu). \tag{A.26}$$

Here, ν_c denotes the center frequency of spectra. On the other hand, the following relation is satisfied

$$\frac{A_{ul}}{B_{ul}} = \frac{2h\nu_c^3}{c^2} \tag{A.27}$$

$$g_l B_{lu} = g_u B_{ul} \tag{A.28}$$

$$\frac{n_u}{n_l} = \frac{g_u}{g_l} \exp\left[-\frac{\Delta E}{kT_{ex}}\right] \tag{A.29}$$

$$\Delta E = h\nu_c, \tag{A.30}$$

and the following relation is satisfied

$$\frac{j_\nu}{\alpha_\nu} = \frac{2h\nu_c^3/c^2}{e^{\frac{h\nu_c}{kT_{ex}}} - 1}. \tag{A.31}$$

When we sabstitute this relation into the solution of the radiative transfer equation:

$$I_{\nu_c}(s) = I_{\nu_c} e^{-\alpha_\nu s} + \frac{j_\nu}{\alpha_\nu} (1 - e^{-\alpha_\nu s}), \tag{A.32}$$

the specific intensity is given by

$$I_{\nu_c}(\tau) = I_{\nu_c} e^{-\tau} + \frac{2h\nu_c^3/c^2}{e^{\frac{h\nu_c}{kT_{ex}}} - 1} (1 - e^{-\tau}). \tag{A.33}$$

Substituting this equation into the brightness temperature T_B

$$T_B \equiv \frac{c^2}{2\nu_c^2 k} \left[I_{\nu_c}(\tau) - I_{\nu_c}(0)\right], \tag{A.34}$$

the brightness temperature is written as follows:

$$T_{\mathrm{B}} = \frac{c^2}{2\nu_{\mathrm{c}}^2 k}\left[\frac{2h\nu_{\mathrm{c}}^3/c^2}{\mathrm{e}^{\frac{h\nu_{\mathrm{c}}}{kT_{\mathrm{ex}}}}-1}\left(1-\mathrm{e}^{-\tau}\right) - I_{\nu_{\mathrm{c}}}(0)\left(1-\mathrm{e}^{-\tau}\right)\right]. \tag{A.35}$$

Here, assuming that $I_{\nu_{\mathrm{c}}}(0)$ is the cosmic background radiation, $I_{\nu_{\mathrm{c}}}(0)$ is given by

$$I_{\nu_{\mathrm{c}}}(0) = B_{\nu_{\mathrm{c}}}(T_{\mathrm{bg}}) = \frac{2h\nu_c^3/c^2}{\mathrm{e}^{\frac{h\nu_{\mathrm{c}}}{kT_{\mathrm{ex}}}}-1}. \tag{A.36}$$

Then, the brightness temperature is written as

$$T_{\mathrm{B}} = \frac{h\nu_{\mathrm{c}}}{k}\left[\frac{1}{\mathrm{e}^{\frac{h\nu_{\mathrm{c}}}{kT_{\mathrm{ex}}}}-1} - \frac{1}{\mathrm{e}^{\frac{h\nu_{\mathrm{c}}}{kT_{\mathrm{bg}}}}-1}\right]. \tag{A.37}$$

Here, we define T_0 and $f(T)$ as follows.

$$T_0 \equiv \frac{h\nu_{\mathrm{c}}}{k} \tag{A.38}$$

$$f(T) \equiv \frac{1}{\mathrm{e}^{\frac{T_0}{T}}-1} \tag{A.39}$$

The brightness temperature can be written by T_0 and $f(T)$ as follows

$$T_{\mathrm{B}} = T_0\left[f(T_{\mathrm{ex}}) - f(T_{\mathrm{bg}})\right](1-\mathrm{e}^{-\tau}). \tag{A.40}$$

This equation is called the detection equation.

Appendix B

Column density

Assuming the Boltzmann distribution, the number density of the upper state energy is given by

$$n_{\mathrm{u}} = \frac{n g_{\mathrm{u}}}{Z} \exp\left[-\frac{E}{kT}\right]. \tag{B.1}$$

Here, Z denotes the distribution function, and E_u the upper state energy. The absorption coefficient can be written with the Einstein coefficient as

$$\alpha = \frac{h\nu}{4\pi} \left(B_{\mathrm{lu}} g_{\mathrm{l}} n_{\mathrm{l}} - B_{\mathrm{ul}} g_{\mathrm{u}} n_{\mathrm{u}}\right) \phi(\nu). \tag{B.2}$$

When we use the LTE approximation, the ratio of the number density is written as follows:

$$\frac{n_{\mathrm{l}}}{n_{\mathrm{u}}} = \exp\left[\frac{h\nu}{kT}\right]. \tag{B.3}$$

Assuming that line profile function is almost the same as $\frac{1}{\Delta\nu}$, the abosorption coefficient is written by

$$\alpha = \frac{c^2 n}{8\pi\nu^2 \Delta\nu Z} \left[\exp\left(\frac{h\nu}{kT}\right) - 1\right] . \exp\left[-\frac{E_{\mathrm{u}}}{kT}\right] g_{\mathrm{u}} A_{\mathrm{ul}} \tag{B.4}$$

Moreover, $A_{\rm ul}$ and Δv are given by

$$g_{\rm u}A_{\rm ul} = \frac{64\pi^4\nu^3\mu_0^2 S_{\rm ul}}{3hc^3} \tag{B.5}$$

$$\Delta\nu = \frac{\Delta v}{c}\nu, \tag{B.6}$$

and the absorption coefficient is written as follows:

$$\alpha = \frac{8\pi^3\mu_0^2 S_{\rm ul} n}{3h\Delta\nu Z}\left[\exp\left(\frac{h\nu}{kT}\right)-1\right].\exp\left[-\frac{E_{\rm u}}{kT}\right] \tag{B.7}$$

The optical depth τ and the column density N are written with the distance s as

$$\tau = \alpha s \tag{B.8}$$

$$N = ns. \tag{B.9}$$

Then, the optical depth is given as follows:

$$\tau = \frac{8\pi^3\mu_0^2 S_{\rm ul} N}{3h\Delta\nu Z}\exp\left[\left(\frac{h\nu}{kT}\right)-1\right]\exp\left[-\frac{E_{\rm u}}{kT}\right]. \tag{B.10}$$

Here, Δv is the line width.

We assume the integrated intensity W as $W = T_{\rm obs}\Delta v$. Then, by the detection equation, the observed temperature can be written by

$$T_{\rm obs} \simeq (T_{\rm ex} - T_{\rm b})\left(1 - e^{-\tau}\right). \tag{B.11}$$

The column density is written as follows:

$$N = -\frac{3h\Delta\nu Z}{8\pi^3\mu_0^2 S_{\rm ul}}\left[\exp\left(\frac{h\nu}{kT}\right)-1\right]^{-1}\exp\left(\frac{E_{\rm u}}{kT}\right)\ln\left[1-\frac{W}{\Delta v\,(T-T_{\rm b})}\right]. \tag{B.12}$$

On the other hand, the optical dipth is given, the column density is written as

$$N = \tau\frac{3h\Delta\nu Z}{8\pi^3(S_{\rm ul}\mu^2)}\left[\exp\left(\frac{h\nu}{kT}\right)-1\right]^{-1}\exp\left(\frac{E_{\rm u}}{kT}\right). \tag{B.13}$$

Here, the distribution function is given as follows:

$$\begin{aligned} Z &= \sum_{i=1}^{n} g_i \exp\left[-\frac{E_i}{kT}\right] \\ &= \sum_{i=1}^{n} (2J+1) \exp\left[-\frac{BJ(J+1)}{kT_{\rm ex}}\right] \\ &\simeq \frac{kT}{hB} \qquad \text{(B.14)} \\ B &= \frac{h}{8\pi I}. \qquad \text{(B.15)} \end{aligned}$$

Then, column density is written as follows:

$$N = \tau \frac{3hc\Delta\nu}{8\pi^3 \nu_{\rm c} (S_{\rm ul}\mu^2)} \frac{kT_{\rm ex}}{hB} \left[\exp\left(\frac{h\nu_{\rm c}}{kT_{\rm ex}}\right) - 1\right]^{-1} \exp\left(\frac{E_{\rm u}}{kT_{\rm ex}}\right). \qquad \text{(B.16)}$$

References

[1] G. Anglada, I. Sepulveda, and J. F. Gomez. Ammonia observations towards molecular and optical outflows. *A&AS*, Vol. 121, pp. 255–274, February 1997.

[2] A. Bacmann, B. Lefloch, C. Ceccarelli, A. Castets, J. Steinacker, and L. Loinard. The degree of CO depletion in pre-stellar cores. *A&A*, Vol. 389, pp. L6–L10, July 2002.

[3] A. Bacmann, B. Lefloch, C. Ceccarelli, J. Steinacker, A. Castets, and L. Loinard. CO Depletion and Deuterium Fractionation in Prestellar Cores. *ApJ*, Vol. 585, pp. L55–L58, March 2003.

[4] L. G. Balazs, J. Eisloeffel, A. Holl, J. Kelemen, and M. Kun. The optical counterpart of the IRAS point source 22343+7501 in L1251. *A&A*, Vol. 255, pp. 281–284, February 1992.

[5] M. T. Beltrán, R. Estalella, G. Anglada, L. F. Rodríguez, and J. M. Torrelles. Radio Spectral Indices of the Powering Sources of Outflows. *AJ*, Vol. 121, pp. 1556–1568, March 2001.

[6] P. J. Benson and P. C. Myers. A survey for dense cores in dark clouds. *ApJS*, Vol. 71, pp. 89–108, September 1989.

[7] S. Bottinelli, C. Ceccarelli, J. P. Williams, and B. Lefloch. Hot corinos in NGC 1333-IRAS4B and IRAS2A. *A&A*, Vol. 463, pp. 601–610, February 2007.

[8] H. M. Butner, N. J. Evans, II, P. M. Harvey, L. G. Mundy, A. Natta, and M. S. Randich. High-resolution, far-infrared observations of NGC 2071. *ApJ*, Vol. 364, pp. 164–172, November 1990.

[9] P. Caselli, F. F. S. van der Tak, C. Ceccarelli, and A. Bacmann. Abundant H_2D^+ in the pre-stellar core L1544. *A&A*, Vol. 403, pp. L37–L41, May 2003.

[10] P. Caselli, C. M. Walmsley, M. Tafalla, L. Dore, and P. C. Myers. CO Depletion in the Starless Cloud Core L1544. *ApJ*, Vol. 523, pp. L165–L169, October 1999.

[11] P. Caselli, C. M. Walmsley, A. Zucconi, M. Tafalla, L. Dore, and P. C. Myers. Molecular Ions in L1544. II. The Ionization Degree. *ApJ*, Vol. 565, pp. 344–358, January 2002.

[12] S. Cazaux, A. G. G. M. Tielens, C. Ceccarelli, A. Castets, V. Wakelam, E. Caux, B. Parise, and D. Teyssier. The Hot Core around the Low-mass Protostar IRAS 16293-2422: Scoundrels Rule! *ApJ*, Vol. 593, pp. L51–L55, August 2003.

[13] C. Ceccarelli, A. Castets, L. Loinard, E. Caux, and A. G. G. M. Tielens. Detection of doubly deuterated formaldehyde towards the low-luminosity protostar IRAS 16293-2422. *A&A*, Vol. 338, pp. L43–L46, October 1998.

[14] K. Cernis. Interstellar extinction in the vicinity of the reflection nebula NGC 1333 in Perseus. *Ap&SS*, Vol. 166, pp. 315–330, April 1990.

[15] A. C. Cheung, D. M. Rank, C. H. Townes, D. D. Thornton, and W. J. Welch. Detection of NH_3 Molecules in the Interstellar Medium by Their Microwave Emission. *Physical Review Letters*, Vol. 21, pp. 1701–1705, December 1968.

[16] M. J. Claussen, B. A. Wilking, P. J. Benson, A. Wootten, P. C. Myers, and S. Terebey. A Monthly Survey of Water Masers Associated with Low-Mass Stars. *ApJS*, Vol. 106, p. 111, September 1996.

[17] T. M. Dame and P. Thaddeus. A wide-latitude CO survey of molecular clouds in the northern Milky Way. *ApJ*, Vol. 297, pp. 751–765, October 1985.

[18] T. M. Dame, H. Ungerechts, R. S. Cohen, E. J. de Geus, I. A. Grenier, J. May, D. C. Murphy, L.-A. Nyman, and P. Thaddeus. A composite CO survey of the entire Milky Way. *ApJ*, Vol. 322, pp. 706–720, November 1987.

[19] I. de Gregorio-Monsalvo, J. F. Gómez, O. Suárez, T. B. H. Kuiper, L. F. Rodríguez, and E. Jiménez-Bailón. CCS and NH_3 Emission Associated with Low-Mass Young Stellar Objects. *ApJ*, Vol. 642, pp. 319–329, May 2006.

[20] M. M. Dunham, H. G. Arce, D. Mardones, J.-E. Lee, B. C. Matthews, A. M. Stutz, and J. P. Williams. Molecular Outflows Driven by Low-mass Protostars. I. Correcting

for Underestimates When Measuring Outflow Masses and Dynamical Properties. *ApJ*, Vol. 783, p. 29, March 2014.

[21] C. Eiroa, J. M. Torrelles, L. F. Miranda, G. Anglada, and R. Estalella. Optical nebulosities associated with IRAS sources in dense cloud cores. *A&AS*, Vol. 108, pp. 73–78, November 1994.

[22] M. Emprechtinger, P. Caselli, N. H. Volgenau, J. Stutzki, and M. C. Wiedner. The N{2}Dˆ+/N{2}H^+ ratio as an evolutionary tracer of Class 0 protostars. *A&A*, Vol. 493, pp. 89–105, January 2009.

[23] M. Emprechtinger, M. C. Wiedner, R. Simon, G. Wieching, N. H. Volgenau, F. Bielau, U. U. Graf, R. Güsten, C. E. Honingh, K. Jacobs, D. Rabanus, J. Stutzki, and F. Wyrowski. The molecular environment of the massive star forming region NGC 2024: Multi CO transition analysis. *A&A*, Vol. 496, pp. 731–739, March 2009.

[24] F. Fontani, T. Sakai, K. Furuya, N. Sakai, Y. Aikawa, and S. Yamamoto. DNC/HNC and N_2D^+/N_2H^+ ratios in high-mass star-forming cores. *MNRAS*, Vol. 440, pp. 448–456, May 2014.

[25] C. V. M. Fridlund, P. Bergman, G. J. White, G. L. Pilbratt, and J. A. Tauber. The molecular disk surrounding the protostellar binary L1551 IRS5. *A&A*, Vol. 382, pp. 573–582, February 2002.

[26] G. A. Fuller and P. C. Myers. Thermal Material in Dense Cores: A New Narrow-Line Probe and Technique of Temperature Determination. *ApJ*, Vol. 418, p. 273, November 1993.

[27] G. A. Fuller and A. Wootten. Small-Scale Structure of the Circumstellar Gas around the Very Young Outflow-Driving Source L483-FIR. *ApJ*, Vol. 534, pp. 854–869, May 2000.

[28] M. Gerin, J. C. Pearson, E. Roueff, E. Falgarone, and T. G. Phillips. Determination of the Hyperfine Structure of N_2D^+. *ApJ*, Vol. 551, pp. L193–L197, April 2001.

[29] A. A. Goodman, P. J. Benson, G. A. Fuller, and P. C. Myers. Dense cores in dark clouds. VIII - Velocity gradients. *ApJ*, Vol. 406, pp. 528–547, April 1993.

[30] D. M. Graninger, E. Herbst, K. I. Öberg, and A. I. Vasyunin. The HNC/HCN Ratio in Star-forming Regions. *ApJ*, Vol. 787, p. 74, May 2014.

[31] E. M. Gregersen, N. J. Evans, II, S. Zhou, and M. Choi. New Protostellar Collapse Candidates: An HCO^+ Survey of the Class 0 Sources. *ApJ*, Vol. 484, pp. 256–276, July 1997.

[32] R. A. Gutermuth, P. C. Myers, S. T. Megeath, L. E. Allen, J. L. Pipher, J. Muzerolle, A. Porras, E. Winston, and G. Fazio. Spitzer Observations of NGC 1333: A Study of Structure and Evolution in a Nearby Embedded Cluster. *ApJ*, Vol. 674, pp. 336–356, February 2008.

[33] C. Hayashi. Stellar evolution in early phases of gravitational contraction. *PASJ*, Vol. 13, pp. 450–452, 1961.

[34] N. Hirano, H. Mikami, T. Umemoto, S. Yamamoto, and Y. Taniguchi. SIO Emission in the Multilobe Outflow Associated with IRAS 16293-2422. *ApJ*, Vol. 547, pp. 899–906, February 2001.

[35] T. Hirota, T. Bushimata, Y. K. Choi, M. Honma, H. Imai, K. Iwadate, T. Jike, O. Kameya, R. Kamohara, Y. Kan-Ya, N. Kawaguchi, M. Kijima, H. Kobayashi, S. Kuji, T. Kurayama, S. Manabe, T. Miyaji, T. Nagayama, A. Nakagawa, C. S. Oh, T. Omodaka, T. Oyama, S. Sakai, T. Sasao, K. Sato, K. M. Shibata, Y. Tamura, and K. Yamashita. Astrometry of H_2O Masers in Nearby Star-Forming Regions with VERA. II. SVS13 in NGC1333. *PASJ*, Vol. 60, pp. 37–, February 2008.

[36] T. Hirota, M. Ikeda, and S. Yamamoto. Observations of DNC and $HN^{13}C$ in Dark Cloud Cores. *ApJ*, Vol. 547, pp. 814–828, February 2001.

[37] T. Hirota, S. Yamamoto, H. Mikami, and M. Ohishi. Abundances of HCN and HNC in Dark Cloud Cores. *ApJ*, Vol. 503, pp. 717–728, August 1998.

[38] P. T. P. Ho, J. M. Moran, and K. Y. Lo. The Submillimeter Array. *ApJ*, Vol. 616, pp. L1–L6, November 2004.

[39] R. E. Jennings, D. H. M. Cameron, W. Cudlip, and C. J. Hirst. IRAS observations of NGC1333. *MNRAS*, Vol. 226, pp. 461–471, May 1987.

[40] J. K. Jørgensen. Imaging chemical differentiation around the low-mass protostar L483-mm. *A&A*, Vol. 424, pp. 589–601, September 2004.

[41] J. K. Jørgensen, T. L. Bourke, P. C. Myers, J. Di Francesco, E. F. van Dishoeck, C.-F. Lee, N. Ohashi, F. L. Schöier, S. Takakuwa, D. J. Wilner, and Q. Zhang. PROSAC: A Submillimeter Array Survey of Low-Mass Protostars. I. Overview of Program: Envelopes, Disks, Outflows, and Hot Cores. *ApJ*, Vol. 659, pp. 479–498, April 2007.

[42] J. K. Jørgensen, T. L. Bourke, P. C. Myers, F. L. Schöier, E. F. van Dishoeck, and D. J. Wilner. Probing the Inner 200 AU of Low-Mass Protostars with the Submillimeter Array: Dust and Organic Molecules in NGC 1333 IRAS 2A. *ApJ*, Vol. 632, pp. 973–981, October 2005.

[43] J. K. Jørgensen, M. R. Hogerheijde, E. F. van Dishoeck, G. A. Blake, and F. L. Schöier. The structure of the NGC 1333-IRAS2 protostellar system on 500 AU scales. An infalling envelope, a circumstellar disk, multiple outflows, and chemistry. *A&A*, Vol. 413, pp. 993–1007, January 2004.

[44] J. K. Jørgensen, D. Johnstone, H. Kirk, and P. C. Myers. Current Star Formation in the Perseus Molecular Cloud: Constraints from Unbiased Submillimeter and Mid-Infrared Surveys. *ApJ*, Vol. 656, pp. 293–305, February 2007.

[45] J. K. Jørgensen, F. L. Schöier, and E. F. van Dishoeck. Physical structure and CO abundance of low-mass protostellar envelopes. *A&A*, Vol. 389, pp. 908–930, July 2002.

[46] J. K. Jørgensen, F. L. Schöier, and E. F. van Dishoeck. Molecular inventories and chemical evolution of low-mass protostellar envelopes. *A&A*, Vol. 416, pp. 603–622, March 2004.

[47] N. Kaifu, T. Hasegawa, M. Morimoto, J. Inatani, K. Nagane, K. Miyazawa, Y. Chikada, T. Kanzawa, K. Akabane, and S. Suzuki. Rotating gas disk around L1551 IRS-5. *A&A*, Vol. 134, pp. 7–12, May 1984.

[48] L. B. G. Knee and G. Sandell. The molecular outflows in NGC 1333. *A&A*, Vol. 361, pp. 671–684, September 2000.

[49] M. Kun. Star Formation in the Cepheus Flare Molecular Clouds. I. Distance Determination and the Young Stellar Object Candidates. *ApJS*, Vol. 115, pp. 59–89, March 1998.

[50] M. Kun and T. Prusti. Star Formation in L:1251 - Distance and Members. *A&A*, Vol. 272, p. 235, May 1993.

[51] C. J. Lada. Star formation - From OB associations to protostars. In M. Peimbert and J. Jugaku, editors, *Star Forming Regions*, Vol. 115 of *IAU Symposium*, pp. 1–17, 1987.

[52] D. C. Lis, M. Gerin, T. G. Phillips, and F. Motte. The Role of Outflows and C Shocks in the Strong Deuteration of L1689N. *ApJ*, Vol. 569, pp. 322–333, April 2002.

[53] D. C. Lis, E. Roueff, M. Gerin, T. G. Phillips, L. H. Coudert, F. F. S. van der Tak, and P. Schilke. Detection of Triply Deuterated Ammonia in the Barnard 1 Cloud. *ApJ*, Vol. 571, pp. L55–L58, May 2002.

[54] R. Liseau, G. Sandell, and L. B. G. Knee. The structure of the molecular outflow near SSV 13 and HH 7-11 in the NGC 1333 region. *A&A*, Vol. 192, pp. 153–164, March 1988.

[55] F.-C. Liu, B. Parise, L. Kristensen, R. Visser, E. F. van Dishoeck, and R. Güsten. Water deuterium fractionation in the low-mass protostar NGC1333-IRAS2A. *A&A*, Vol. 527, p. A19, March 2011.

[56] L. Loinard, A. Castets, C. Ceccarelli, E. Caux, and A. G. G. M. Tielens. Doubly Deuterated Molecular Species in Protostellar Environments. *ApJ*, Vol. 552, pp. L163–L166, May 2001.

[57] L. W. Looney, L. G. Mundy, and W. J. Welch. Unveiling the Circumstellar Envelope and Disk: A Subarcsecond Survey of Circumstellar Structures. *ApJ*, Vol. 529, pp. 477–498, January 2000.

[58] R. Lucas and H. Liszt. Interstellar isotope ratios from mm-wave molecular absorption spectra. *A&A*, Vol. 337, pp. 246–252, September 1998.

[59] D. Mardones, P. C. Myers, M. Tafalla, D. J. Wilner, R. Bachiller, and G. Garay. A Search for Infall Motions toward Nearby Young Stellar Objects. *ApJ*, Vol. 489, pp. 719–733, November 1997.

[60] A. McKellar. Evidence for the Molecular Origin of Some Hitherto Unidentified Interstellar Lines. *PASP*, Vol. 52, p. 187, June 1940.

[61] T. J. Millar, P. R. A. Farquhar, and K. Willacy. The UMIST Database for Astrochemistry 1995. *A&AS*, Vol. 121, pp. 139–185, January 1997.

[62] A. Mizuno, Y. Fukui, T. Iwata, S. Nozawa, and T. Takano. A remarkable multilobe molecular outflow - Rho Ophiuchi East, associated with IRAS 16293-2422. *ApJ*, Vol. 356, pp. 184–194, June 1990.

[63] M. Momose, N. Ohashi, R. Kawabe, T. Nakano, and M. Hayashi. Aperture Synthesis $C^{18}O$ J = 1-0 Observations of L1551 IRS 5: Detailed Structure of the Infalling Envelope. *ApJ*, Vol. 504, pp. 314–333, September 1998.

[64] F. Motte and P. André. The circumstellar environment of low-mass protostars: A millimeter continuum mapping survey. *A&A*, Vol. 365, pp. 440–464, January 2001.

[65] L. G. Mundy, A. Wootten, B. A. Wilking, G. A. Blake, and A. I. Sargent. IRAS 16293 - 2422 - A very young binary system? *ApJ*, Vol. 385, pp. 306–313, January 1992.

[66] P. C. Myers, R. Bachiller, P. Caselli, G. A. Fuller, D. Mardones, M. Tafalla, and D. J. Wilner. Gravitational Infall in the Dense Cores L1527 and L483. *ApJ*, Vol. 449, p. L65, August 1995.

[67] P. C. Myers, R. A. Linke, and P. J. Benson. Dense cores in dark clouds. I - CO observations and column densities of high-extinction regions. *ApJ*, Vol. 264, pp. 517–537, January 1983.

[68] S. Nikolić, L. E. B. Johansson, and J. Harju. Star forming cores in L 1251: Maps and molecular abundances. *A&A*, Vol. 409, pp. 941–951, October 2003.

[69] L. Pagani, A. Bacmann, S. Cabrit, and C. Vastel. Depletion and low gas temperature in the L183 (=L134N) prestellar core: the N2Hˆ+-$N2D^+$ tool. *A&A*, Vol. 467, pp. 179–186, May 2007.

[70] B. Parise, A. Castets, E. Herbst, E. Caux, C. Ceccarelli, I. Mukhopadhyay, and A. G. G. M. Tielens. First detection of triply-deuterated methanol. *A&A*, Vol. 416, pp. 159–163, March 2004.

[71] B. Parise, E. Caux, A. Castets, C. Ceccarelli, L. Loinard, A. G. G. M. Tielens, A. Bacmann, S. Cazaux, C. Comito, F. Helmich, C. Kahane, P. Schilke, E. van Dishoeck, V. Wakelam, and A. Walters. HDO abundance in the envelope of the solar-type protostar IRAS 16293-2422. *A&A*, Vol. 431, pp. 547–554, February 2005.

[72] B. Parise, C. Ceccarelli, A. G. G. M. Tielens, A. Castets, E. Caux, B. Lefloch, and S. Maret. Testing grain surface chemistry: a survey of deuterated formaldehyde and methanol in low-mass class 0 protostars. *A&A*, Vol. 453, pp. 949–958, July 2006.

[73] B. Parise, C. Ceccarelli, A. G. G. M. Tielens, E. Herbst, B. Lefloch, E. Caux, A. Castets, I. Mukhopadhyay, L. Pagani, and L. Loinard. Detection of doubly-deuterated methanol in the solar-type protostar IRAS 16293-2422. *A&A*, Vol. 393, pp. L49–L53, October 2002.

[74] Y.-S. Park, J.-F. Panis, N. Ohashi, M. Choi, and Y. C. Minh. Interferometric Observation of the L483 Molecular Core. *ApJ*, Vol. 542, pp. 344–351, October 2000.

[75] N. D. Parker. IRAS associations with dark clouds of opacity class 6. *MNRAS*, Vol. 235, pp. 139–150, November 1988.

[76] A. J. Remijan and J. M. Hollis. IRAS 16293-2422: Evidence for Infall onto a Counterrotating Protostellar Accretion Disk. *ApJ*, Vol. 640, pp. 842–848, April 2006.

[77] H. Roberts. Modelling of Deuterium Chemistry in Star-Forming Regions. In D. C. Lis, G. A. Blake, and E. Herbst, editors, *Astrochemistry: Recent Successes and Current Challenges*, Vol. 231 of *IAU Symposium*, pp. 27–36, August 2005.

[78] H. Roberts, E. Herbst, and T. J. Millar. The importance of new rate coefficients for deuterium fractionation reactions in interstellar chemistry. *MNRAS*, Vol. 336, pp. 283–290, October 2002.

[79] H. Roberts and T. J. Millar. A survey of [D2CO] /[H2CO] and [N2Dˆ+] /[N2Hˆ+] ratios towards protostellar cores. *A&A*, Vol. 471, pp. 849–863, September 2007.

[80] E. Roueff, S. Tiné, L. H. Coudert, G. Pineau des Forêts, E. Falgarone, and M. Gerin. Detection of doubly deuterated ammonia in L134N. *A&A*, Vol. 354, pp. L63–L66, February 2000.

[81] T. Sakai, N. Sakai, K. Furuya, Y. Aikawa, T. Hirota, and S. Yamamoto. DNC/HNC Ratio of Massive Clumps in Early Evolutionary Stages of High-mass Star Formation. *ApJ*, Vol. 747, p. 140, March 2012.

[82] G. Sandell and L. B. G. Knee. NGC 1333-Protostars, Dust Shells, and Triggered Star Formation. *ApJ*, Vol. 546, pp. L49–L52, January 2001.

[83] G. Sandell, L. B. G. Knee, C. Aspin, I. E. Robson, and A. P. G. Russell. A molecular jet and bow shock in the low mass protostellar binary NGC 1333-IRAS2. *A&A*, Vol. 285, pp. L1–L4, May 1994.

[84] F. Sato and Y. Fukui. Two molecular outflows in L1251. *ApJ*, Vol. 343, pp. 773–778, August 1989.

[85] F. Sato, A. Mizuno, T. Nagahama, T. Onishi, Y. Yonekura, and Y. Fukui. A new look at the dark cloud L1251: Sensitive observations of the molecular emission. *ApJ*, Vol. 435, pp. 279–289, November 1994.

[86] F. L. Schöier, J. K. Jørgensen, E. F. van Dishoeck, and G. A. Blake. Does IRAS 16293-2422 have a hot core? Chemical inventory and abundance changes in its protostellar environment. *A&A*, Vol. 390, pp. 1001–1021, August 2002.

[87] Y. L. Shirley, N. J. Evans, II, J. M. C. Rawlings, and E. M. Gregersen. Tracing the Mass during Low-Mass Star Formation. I. Submillimeter Continuum Observations. *ApJS*, Vol. 131, pp. 249–271, November 2000.

[88] R. L. Snell, R. B. Loren, and R. L. Plambeck. Observations of CO in L1551 - Evidence for stellar wind driven shocks. *ApJ*, Vol. 239, pp. L17–L22, July 1980.

[89] T. Stantcheva and E. Herbst. Deuterium fractionation on interstellar grains studied with the direct master equation approach. *MNRAS*, Vol. 340, pp. 983–988, April 2003.

[90] K. M. Strom, S. E. Strom, and F. J. Vrba. Infrared surveys of dark-cloud complexes. IV. The Lynds 1517 and Lynds 1551 clouds. *AJ*, Vol. 81, pp. 320–322, May 1976.

[91] M. Sugimoto, Y. Sekimoto, K. Tatematsu, T. Kamba, H. Toba, S. Yokogawa, T. Okuda, K. Kohno, T. Noguchi, N. Yamaguchi, R. Kandori, and K. Muraoka.

Cartridge-Type 800 GHz Receiver for the Atacama Submillimeter Telescope Experiment (ASTE). *PASJ*, Vol. 56, pp. 1115–1126, December 2004.

[92] E. C. Sutton, R. Peng, W. C. Danchi, P. A. Jaminet, G. Sandell, and A. P. G. Russell. The distribution of molecules in the core of OMC-1. *ApJS*, Vol. 97, pp. 455–496, April 1995.

[93] M. Tafalla, P. C. Myers, D. Mardones, and R. Bachiller. L483: a protostar in transition from Class 0 to Class I. *A&A*, Vol. 359, pp. 967–976, July 2000.

[94] S. Takakuwa, T. Kamazaki, M. Saito, N. Yamaguchi, and K. Kohno. ASTE Observations of Warm Gas in Low-Mass Protostellar Envelopes: Different Kinematics between Submillimeter and Millimeter Lines. *PASJ*, Vol. 59, pp. 1–13, February 2007.

[95] D. Talbi, Y. Ellinger, and E. Herbst. On the HCN/HNC abundance ratio: a theoretical study of the H+CNH - HCN+H exchange reactions. *A&A*, Vol. 314, pp. 688–692, October 1996.

[96] V. Taquet, A. López-Sepulcre, C. Ceccarelli, R. Neri, C. Kahane, A. Coutens, and C. Vastel. Water Deuterium Fractionation in the Inner Regions of Two Solar-type Protostars. *ApJ*, Vol. 768, p. L29, May 2013.

[97] K. Tatematsu, T. Umemoto, R. Kandori, and Y. Sekimoto. N_2H^+ Observations of Molecular Cloud Cores in Taurus. *ApJ*, Vol. 606, pp. 333–340, May 2004.

[98] S. Terebey, C. J. Chandler, and P. Andre. The contribution of disks and envelopes to the millimeter continuum emission from very young low-mass stars. *ApJ*, Vol. 414, pp. 759–772, September 1993.

[99] S. Tiné, E. Roueff, E. Falgarone, M. Gerin, and G. Pineau des Forêts. Deuterium fractionation in dense ammonia cores. *A&A*, Vol. 356, pp. 1039–1049, April 2000.

[100] B. E. Turner. Detection of doubly deuterated interstellar formaldehyde (D2CO) - an indicator of active grain surface chemistry. *ApJ*, Vol. 362, pp. L29–L33, October 1990.

[101] F. F. S. van der Tak, P. Schilke, H. S. P. Müller, D. C. Lis, T. G. Phillips, M. Gerin, and E. Roueff. Triply deuterated ammonia in NGC 1333. *A&A*, Vol. 388, pp. L53–L56, June 2002.

[102] E. F. van Dishoeck, G. A. Blake, D. J. Jansen, and T. D. Groesbeck. Molecular Abundances and Low-Mass Star Formation. II. Organic and Deuterated Species toward IRAS 16293-2422. *ApJ*, Vol. 447, p. 760, July 1995.

[103] B. A. Wilking, M. J. Claussen, P. J. Benson, P. C. Myers, S. Terebey, and A. Wootten. Water masers associated with low-mass stars: A 13 month monitoring survey. *ApJ*, Vol. 431, pp. L119–L122, August 1994.

[104] R. W. Wilson, K. B. Jefferts, and A. A. Penzias. Carbon Monoxide in the Orion Nebula. *ApJ*, Vol. 161, p. L43, July 1970.

[105] A. Wootten and R. B. Loren. L1689N - Misalignment between a bipolar outflow and a magnetic field. *ApJ*, Vol. 317, pp. 220–230, June 1987.

[106] A. Wootten, R. B. Loren, and R. L. Snell. A study of DCO+ emission regions in interstellar clouds. *ApJ*, Vol. 255, p. 160, April 1982.

[107] P.-F. Wu, S. Takakuwa, and J. Lim. Multiple Bipolar Molecular Outflows from the L1551 IRS5 Protostellar System. *ApJ*, Vol. 698, pp. 184–197, June 2009.

[108] D. Xiang and B. E. Turner. Newly Discovered Galactic H 2O Masers Associated with Outflows. *ApJS*, Vol. 99, p. 121, July 1995.

[109] S. C. C. Yeh, N. Hirano, T. L. Bourke, P. T. P. Ho, C.-F. Lee, N. Ohashi, and S. Takakuwa. The CO Molecular Outflows of IRAS 16293-2422 Probed by the Submillimeter Array. *ApJ*, Vol. 675, pp. 454–463, March 2008.

Acknowledgement

To complete this PhD thesis, I got a lot of supports by many people. Thanks to kind supervision of Prof. Satoshi Yamamoto, I was able to conduct my research. Kind assistant of Dr. Nami Sakai was also great help on my research. Moreover, I would like to appreciate to research associate of our laboratory, Dr. Yoshimasa Watanabe. I was not only received many advice for my research, but also advised for my private affair.

I am also grateful to all members of Yamamoto group, Mr. Tatsuya Soma, Ms. Yuri Nishimura, Ms. Yoko Oya, Mr. Yuuji Ebisawa, Mr. Kento Yoshida, Mr. Osamu Ohguchi and Mrs. Miki Ueda, for their kindness support on conducting my research.

I would like to express my gratitude to Dr. Shigehisa Takakuwa, associate research fellow of ACADEMIA SINICA Institute of Astronomy and Astrophysics. He taught me how to analyse the archival data of SMA. I was able to conduct detail interpretation toward IRAS16293-2422 thanks to his teach.

Prof. Ryugo Hayano, my supervisor of the ALPS course, opened three-monthly meeting where every ALPS course students got together. This meeting was the prime opportunity to hear the research of different field and I was able to get many important advices.

Many people besides Yamamoto group supported me and I was able to conduct my research. First of all, my teacher of calligraphy, president of Oyu Shodo-kai, Mr. Hokuto Kondo has been always taking care of me and gives me many advices on my life and career. The members of Oyu Shodo-kai also gave me many supports. Moreover, many friends including Mr. Hiroyasu Tajima supported me and I was able to conduct my research at graduate school.

I was supported by my family in every aspect including daily life. Without their support, I could not have conducted my research at graduate school.

Thanks to the support of all of them, I successfully complete my PhD thesis. I would like to extend my heartfelt thanks to all of them on this occasion.